UNIVERSITY OF OKLAHOMA

GRADUATE COLLEGE

PALEOMAGNETIC AND PETROLOGICAL INVESTIGATION OF LONG MOUNTAIN GRANITE, WICHITA MOUNTAINS, OKLAHOMA

A THESIS

SUBMITTED TO THE GRADUATE FACULTY

In partial fulfillment of the requirements for the

Degree of

MASTER OF SCIENCE

By

EVAN MATTHEW HAMILTON

Norman, Oklahoma

2011

THE EFFECTS OF CONFINING PRESSURE ON THE MECHANICAL BEHAVIOR AND DEFORMATION MECHANISMS FOR THE OIL CREEK SANDSTONE IN LABORATORY TESTS

A THESIS

APPROVED FOR THE SCHOOL OF GEOLOGY AND GEOPHYSICS

BY [redacted]

Table of Contents

List of Tables

List of Figures

Abstract

The Long Mountain Granite, a member of the Cambrian-aged Wichita Granite Group, is exposed in the western Wichita Mountains. The rock is red at the surface which grades into a dark gray to green core that has been exposed by quarrying operations. The Long Mountain Granite is a highly granophyric, fluorite-bearing alkali feldspar granite with hedenbergite as the dominant mafic phase. The formation of red granite is not associated with significant geochemical change. Hematite occurs as fracture fill, grain boundary coatings and as slivers inserted along cleavage and exsolution planes in alkali feldspars. The Fe in the hematite appears to be sourced from the oxidation of magnetite and ilmenite and the breakdown of mafic minerals.

Anisotropy of magnetic susceptibility analysis shows that the green granite contains what appears to be a primary magnetic fabric that is consistent with the sill-like emplacement of Wichita-group granites. Demagnetization yields a characteristic remanent magnetization (ChRM) with a pole at 8.8°S, 134.7°E. This is interpreted as a primary Cambrian thermal remanent magnetization residing in magnetite, and is consistent with several other paleomagnetic poles of similar age, providing a new constraint to the Cambrian apparent polar wander path (APWP) for Laurentia.

Red granite has approximately two orders of magnitude lower magnetic susceptibility and natural remanent intensity. The degree of magnetic anisotropy is reduced relative to green granite and the fabrics are incompatible. The ChRM of red granite yields a paleopole at 44.9°N, 124.9°E and is interpreted as a chemical remanent magnetization residing in hematite. This pole is consistent with the late Paleozoic segment of the North American APWP and is consistent with inferred timing of uplift

or exposure. Alteration was likely caused by fluid interactions during this time, either by high-temperature fluids mobilized by uplift or by low-temperature weathering fluids while exposed at the surface.

1. Introduction

Granitoid rocks throughout the world have a wide range of colors; some are nearly white, others green, still others gray to nearly black. Many, however, are also known to exhibit a red coloration that appears to reside in feldspar crystals (Boone, 1969). It has historically been accepted that this red clouding of feldspars is due to the presence of hematite "dust" (e.g., Taylor, 1915; Heinrich and Moore, 1970) as inclusions. The origin of these hematite inclusions, however, has remained a subject of research for decades. Some have proposed a primary magmatic origin for hematite, though this has usually been dismissed on the grounds that other minerals do not contain hematite (e.g., Ernst, 1960); others have suggested solid-state exsolution from iron-bearing feldspar minerals (e.g., Rosenqvist, 1951; Lindqvist, 1966), precipitation during deuteric feldspar recrystallization reactions (e.g., Nakano et al., 2005; Putnis et al., 2007), and general hydrothermal activity (e.g., Wenner and Taylor, 1976) as possible causes for the oxide inclusions. With the exception of Wenner and Taylor's (1976) mention of anomalously young radiometric dates in the St. Francois Mountains, MO, no literature was found that actively investigates the timing of hydrothermal alteration that results in red coloration.

Red color has been found to be due to the presence of sub-micron hematite inclusions in feldspar crystals (Putnis et al., 2007). Hematite can hold magnetic remanence, and has been used in numerous studies of both primary and secondary magnetizations (e.g., Watts et al., 1980; Lynnes and Van der Voo, 1984) and to constrain the timing of diagenetic events (e.g., Elmore et al., 2010). Paleomagnetic analysis of the hematite in red granites should, therefore, be capable of determining the

timing of the reddening alteration of the rock without resorting to spurious radiometric dates as Wenner and Taylor (1976) were forced to do.

Long Mountain, a granite body located in the Wichita Mountains west of Snyder, Oklahoma (Figure 1.1), provides an ideal place to test this hypothesis. Surface exposures of the granite are pink to red, and quarrying operations on the west side of the mountain have exposed a sharp transition to gray-green granite at depth. The Wichita Granite Group, of which the Long Mountain Granite is a part, is considered to be Cambrian in age (Ham et al., 1964). The contrasting exposures provide opportunity to investigate the petrological and magnetic properties of the rock and how they have changed with alteration. Petrological analysis will give clues as to the nature of the alteration, and paleomagnetism will determine the timing.

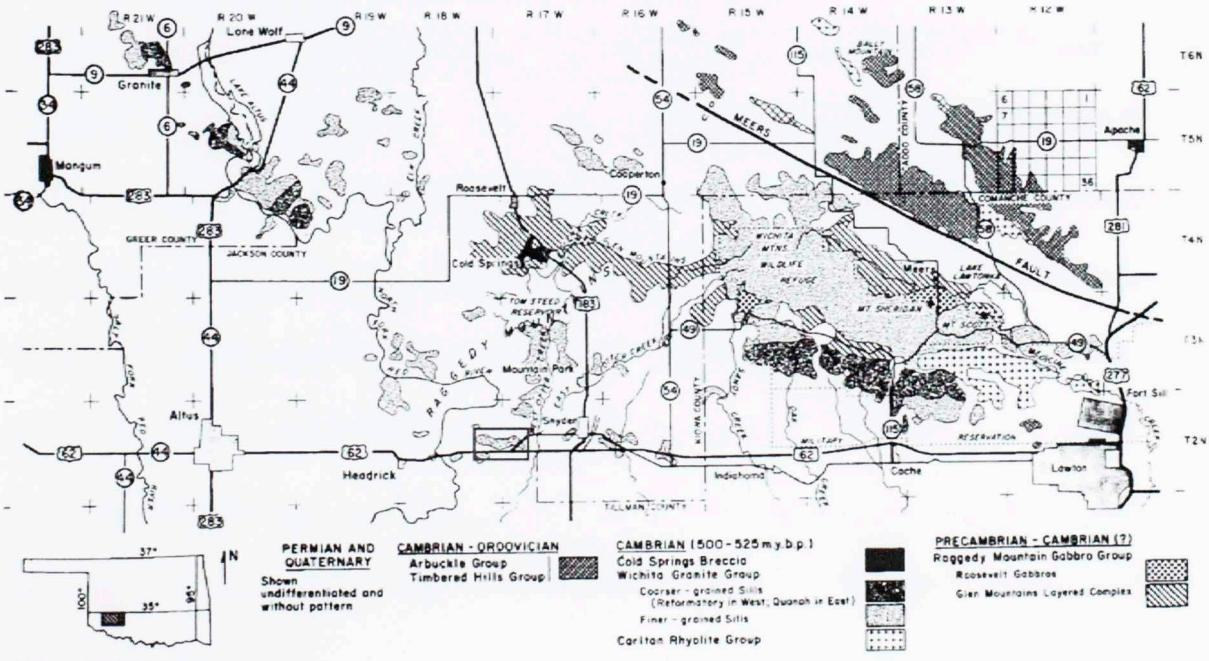

Figure 1.1. Simplified geologic map of the Wichita Mountains area. Long Mountain is outlined by rectangle west of Snyder. Modified from Powell et al. (1980).

Due to its age, the Long Mountain Granite also provides a possible opportunity to obtain a primary Cambrian paleomagnetic pole from the relatively unaltered green Long Mountain granite. Edicaran to Cambrian paleomagnetism in North America is problematic, with paleopoles of roughly the same age having a wide range of locations (e.g., Van der Voo, 1993; Elmore et al., 1998; McCausland et al., 2007; Abrajevitch and Van der Voo, 2010). This led to the now-discredited idea of a Cambrian loop in the apparent polar wander path (e.g., Watts et al., 1980; Lynnes and Van der Voo, 1984) and has led to more modern, yet still controversial, hypotheses such as rapid continental motion due to inertial-interchange true polar wander (Kirschvink et al., 1997) and the presence of an equatorial geomagnetic dipole (Abrajevitch and Van der Voo, 2010) in Ediacaran and Cambrian times.

2. Geologic Background

The concept of an aulacogen as a recompressed rift zone was first put forward by Shatski (1946) and later put into the context of plate tectonics as a failed arm of a rift zone by Hoffman et al. (1974). The Cambrian-aged Southern Oklahoma Aulacogen (SOA), one of several rifts that developed in North America during the breakup of the supercontinent Pannotia, is a classic example of such a feature (Keller et al., 1983; Hogan and Gilbert, 1998). A wealth of information on the structure is available through decades of studies and thousands of petroleum wells drilled into the basins of the region (Keller and Baldridge, 1995). The oldest rocks known to be associated with the aulacogen are those of the Glen Mountains Layered Complex (GMLC), a large layered intrusion with a lateral area of at least 2000 km^2, which forms the backbone of the Wichita Mountains area of the SOA (Powell and Phelps, 1977; Hogan and Gilbert, 1998; Hogan et al., 2000). This body itself was uplifted, tilted by approximately 15°, and eroded prior to further igneous activity, with as much as the top 2-4 km of the GMLC having been eroded away (Powell and Phelps, 1977; Powell et al., 1980). Subsequently, a very large volume of A-type rhyolites were extruded onto the landscape, and a series of sheet-like A-type granite sills emplaced at the base of the volcanic pile. Following granite intrusion, a series of rhyolitic and diabasic dikes penetrated the entire section, constituting the last igneous activity in the region. The total volume of igneous rocks is estimated at approximately 100,000 km^3 intrusive and over 40,000 km^3 volcanic (Keller and Stephenson, 2007).

Once igneous activity ceased, the rift zone quickly began subsiding, and was covered by the Cambro-Ordovician sediments of the Timbered Hills Group, first by the

Reagan Sandstone, which in the area consists largely of sediment derived from the Carlton Rhyolite Group, and subsequently by Honey Creek Formation sandstone and limestone (Gilbert 1982; Donovan, 1982). The region continued to subside and accumulate sediments until the late Mississippian to early Pennsylvanian, when it began to be re-uplifted by the Ouachita Orogeny. This led to the erosion of much of the previous sedimentary cover, and during the Permian the igneous rocks were re-exposed, only to be covered again by Permian conglomerates and other sediments. These are now being eroded away, and at present what is believed to be a fossil Permian surface is being re-exposed (Gilbert, 1982).

Structural and geophysical signs of the SOA extend southeast to the rifted margin in Texas, and northwest as far as Utah. Cambrian-age igneous rocks possibly related to the SOA are also found all along this lineament (Keller and Stephenson, 2007; Larson et al., 1985). The SOA appears from regional gravity data to intersect the southernmost extent of the 1.1 Ga Mid-Continent Rift (MCR) (Figure 2.1).

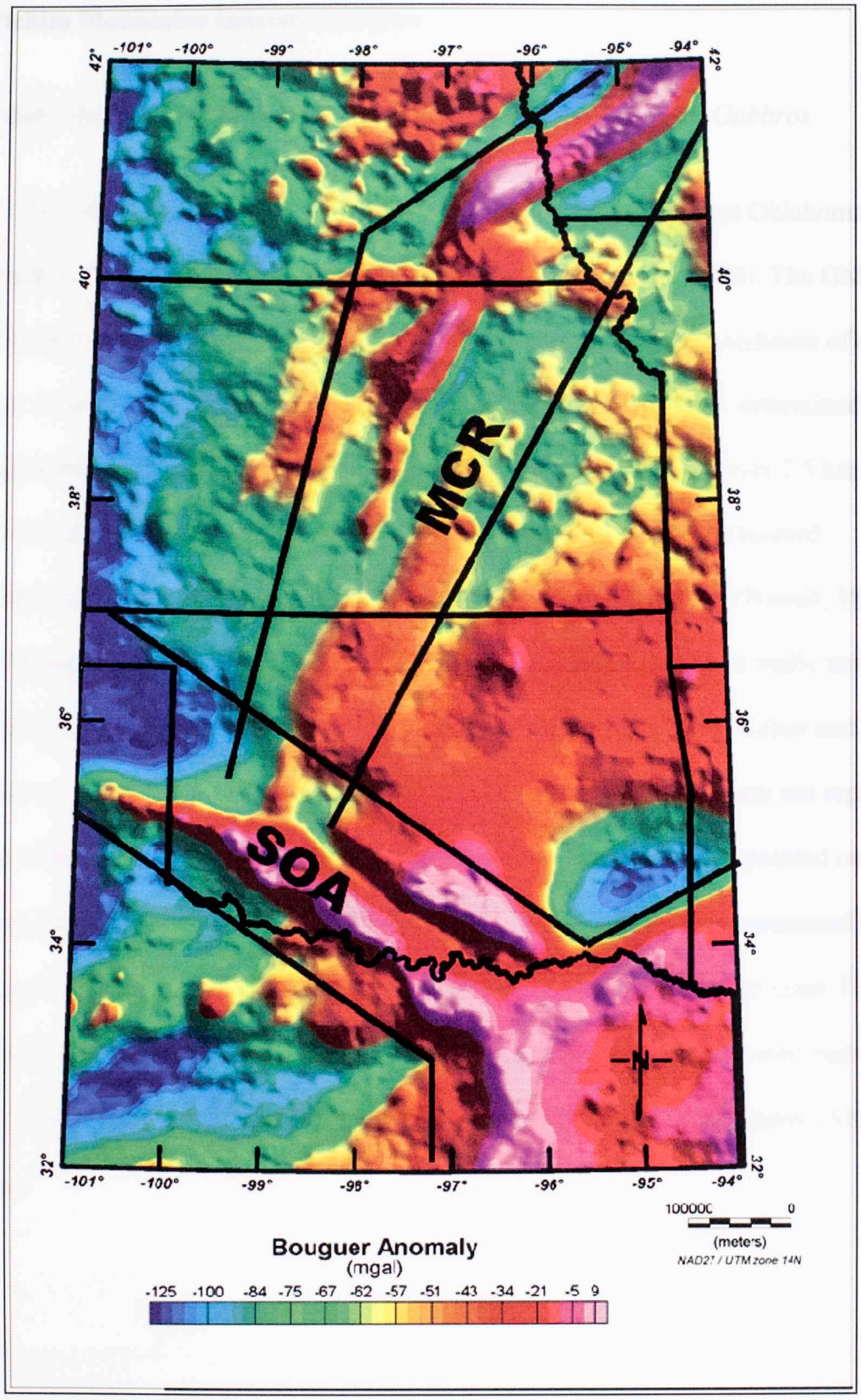

Figure 2.1. Regional gravity map showing intersection of southern Mid-Continent Rift (MCR) with the Southern Oklahoma Aulacogen (SOA). Data from GeoNet Gravity and Magnetic Dataset Repository.

2.1 Wichita Mountains Igneous Province

2.1.1 Mafic Rocks: Glen Mountains Layered Complex and Roosevelt Gabbros

The oldest igneous unit recognized as being part of the Southern Oklahoma Aulacogen is the Glen Mountains Layered Complex (Powell et al., 1980). The GMLC is a very large (~2000 km^2 exposed area) mafic pluton with an exposed thickness of as much as 1 km (Lambert et al., 1988). Its total thickness has never been determined, although Ham et al. (1964) report that it has been drilled to a depth of over 2.5 km. It consists of several rhythmically layered zones, much like other famous layered intrusions such as the Bushveld, Stillwater, and Skaergaard complexes (Powell, 1986). The SOA produces a 125 mgal gravity anomaly that appears to require a mafic mass up to 13 km thick (Robbins and Keller, 1992; Keller and Baldridge, 1995; Keller and Stephenson, 2007) in geophysical modeling (Figure 2.2). This may or may not represent only the GMLC, however, as Gilbert (1982, and references therein) has pointed out that the production of the Wichita granites and rhyolites must have been accompanied by an even larger volume of mafic magmas emplaced into the middle and lower crust. Hogan and Gilbert (1998; Hogan et al., 1998) have proposed that much of this mafic material may be in the form of a subsurface anorthosite-mangerite-charnockite-granite (AMCG) province.

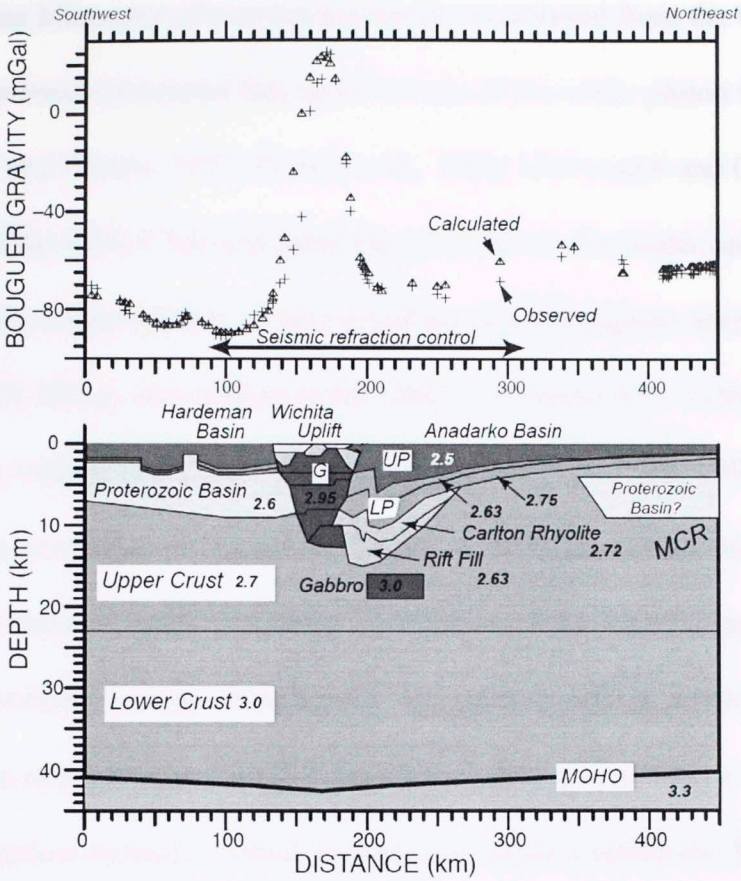

Figure 2.2. Integrated geophysical model of the Southern Oklahoma Aulacogen indicating a large amount of upper and middle crustal mafic material. Modified from Keller and Stephenson (2007).

The age of the GMLC has been problematic to determine, as it does not contain zircon (Lambert et al., 1988). However, attempts have been made by various methods. Ham et al. (1964) determined a likely age of 535 ± 30 Ma based on Rb/Sr analyses and K/Ar dating of amphiboles and biotite. Roggenthen et al. (1981) argued that paleomagnetic measurements indicated a date of either 800 or 1300 Ma, favoring the older age. Lambert et al. (1988) obtained a date of 528 ± 29 Ma based on Sm-Nd isotopes, and a Rb-Sr isochron yielding an age of 577 ± 165 Ma. The uncertainty in all accepted radiometric dates makes the age of the GMLC statistically indistinguishable from the ages of the Wichita granites and rhyolites.

At least one kilometer of overburden has been removed from the GMLC by erosion, and it has been speculated that up to 2-4 km of the mafic pluton itself has been removed (Powell and Phelps, 1977; Powell et al., 1980; McConnell and Gilbert, 1986). As the layering in the GMLC has a general dip of 15-20° to the North, and Wichita granites and rhyolites immediately overlie it and produce an angular unconformity, it is believed that uplift, tilting, and erosion of the GMLC occurred prior to the onset of felsic magmatism within the rift zone (McConnell and Gilbert, 1986, 1990; Powell and Phelps, 1977). The erosional surface of the GMLC is the main surface upon which the Carlton Rhyolites were extruded and along which most of the Wichita granites were intruded. Some modern outcrops of the GMLC are quite saprolitic, and it has been postulated that the combination of a thick rhyolitic sequence overlying a weakened mafic erosional surface formed a crustal magma trap which enabled the Wichita Granites to be intruded along the contact (Hogan and Gilbert, 1995, 1997; Hogan et al., 2000).

Historically, all mafic rocks of the Wichita Mountains area have been grouped together as the Raggedy Mountain Gabbro Group (Ham et al., 1964). This is a geographic grouping rather than a genetic grouping, and essentially consists of the GMLC and the Roosevelt Gabbros, which is the group name for local mafic rock units that are not a part of the GMLC. Earlier models of the SOA assumed that all of the Raggedy Mountain Group predated felsic magmatism (e.g., Myers et al., 1981; Gilbert, 1982). More recent data, however, indicates that the Mount Sheridan Gabbro may be younger than the Mount Scott Granite (Hames et al., 1998; Gilbert and Hogan, 2010). The fine details on the age relationships between mafic and felsic magmatism in the

SOA have yet to be fully investigated. A list of known radiometric ages from the Wichita Igneous Province is listed in Table 2.1.

Table 2.1 Radiometric Dates from the Wichita Mountains Igneous Province

Rock Unit	**Age (Ma)**	**Reference**
Mount Sheridan Gabbro	498 ± 10	Burke et al., 1969
Cold Springs Breccia	514 ± 10	Burke et al., 1969
Roosevelt Gabbros	533 ± 3	Hames et al., 1998
	552 ± 7	Bowring and Hoppe, 1982
Wichita Granites (coarse)	525 ± 25	Tilton et al., 1962
	530 ± 3	Wright et al., 1996
Wichita Granites (fine)	525 ± 25	Tilton et al., 1962
	533 ± 3	Wright et al., 1996
Carlton Rhyolite	525 ± 25	Tilton et al., 1962
	533 ± 3	Wright et al., 1996
Glen Mountains Layered Complex	528 ± 29	Lambert et al., 1998
	577 ± 165	Lambert et al., 1998

2.1.2 Felsic Rocks: Carlton Rhyolites and the Wichita Granite Group

The first major investigation of the felsic igneous rocks of southwest Oklahoma was that of Taylor (1915). Taylor grouped the felsic rocks into five units: the Lugert, Headquarters, Reformatory, and Quanah granites, and the Cold Springs Granite (now Cold Springs Breccia). Of these, the Lugert was by far the largest, and virtually all subsequent separations of units have been recognitions of new units in what was initially called Lugert Granite. Up until the 1960s, the prevailing interpretation of the Wichita Granites was that they represented discontinuous exposure of a single lopolith (e.g., Hamilton, 1959). By the late 1960s, the Carlton Rhyolite Group and the Mount

Scott Granite had been separated from the Lugert (Merritt, 1967) and the lopolith hypothesis abandoned. The currently accepted nomenclature of the Wichita Granite Group was put forward by Myers et al. (1981) and added to the list of formally recognized units the Cooperton, Long Mountain, Cache, Medicine Park, and Saddle Mountain Granites. Gilbert and Myers (1986) point out that the Lugert still contains too much textural variety and geochemical variety (see Weaver and Gilbert, 1986) to represent a single unit, indicating more detailed study is needed. To date, this has not been done.

The most likely reason for the historical tendency to lump different bodies of Wichita granite together is the prevalence of granophyric texture. Taylor (1915) described the prevailing feature of his Lugert Granite to be "a fine-grained intergrowth of quartz and microperthite." Hamilton (1959) describes the rocks of the then-hypothesized Wichita Lopolith as "dominantly granophyres." According to Merritt (1967), in his review of the history of Wichita granite research, some workers went so far as to rename several rock units "granophyres" instead of granite, in their zeal sometimes mistakenly labeling obviously extrusive textures as granophyre. Samples of Mount Scott Granite have been determined to contain from 0-70% granophyre (Myers et al., 1981), and similar or even higher amounts of granophyre are not unusual in other Wichita granites.

All extrusive felsic rocks (and a few rare basalt sills or flows) in the Wichita Mountains Igneous Province are grouped together in the Carlton Rhyolite Group. Carlton Group rhyolites are red and variably spherulitic to porphyritic (Ham et al., 1964; Merritt, 1967). Ham et al. (1964) proposed that the Carlton Group consists of the

extrusive equivalents of the Wichita Granite Group, an idea which has yet to be disproven. The description of the Carlton Rhyolite Group has remained virtually unchanged from that given by Ham et al. (1964), who noted that it consists of welded tuffs, water-laid tuffs, pyroclastic flow deposits, agglomerates, and flow-banded rhyolites, with uncommon basalt flows and devitrified obsidians recognized in the sequence. They estimate an original area of at least 44,000 km^2 was covered by the extrusives, and postulate that Carlton Group rocks may extend westward in the subsurface into the Texas Panhandle. They give a minimum thickness of approximately 1,400 meters based on a drill core. Hogan et al. (2000) argue from a mechanical standpoint that the intrusive style of the granites precludes the volcanic overburden from attaining a thickness greater than approximately 4 km during the timespan of granite intrusion. Given that the rhyolitic volcanics and the granites are believed to be equivalent, the cessation of granite emplacement would likely have coincided closely with the cessation of rhyolitic volcanism, thus 4 km is likely the maximum thickness that the volcanic pile could have ever acquired.

All aerially extensive intrusive granitoids in the Wichita Mountains area are classified as constituting the Wichita Granite Group. Ham et al. (1964) noted that the granites extend across an area of approximately 40,000 km^2 in the subsurface and tend to occur as laterally-extensive sheets approximately 500 meters thick. The granites are universally red, of variable grain size, and variably granophyric (Myers et al., 1981; Gilbert and Myers, 1986). Most of the granites are fine-grained (i.e., <1 cm), while the Quanah and Reformatory tend to be more coarse-grained (≥1 cm) (Myers et al., 1981; Hogan et al., 2000). The Mount Scott Granite is considered to be one of the oldest

Wichita granites and is also currently the most aerially extensive recognized unit of the Wichita Granite Group (Merritt, 1967; Myers et al., 1981; Gilbert and Myers, 1986). All of the Wichita granites were determined by Myers et al. (1981) to fit the classification of A-type granites (see Whalen et al., 1987; Eby, 1990, 1992). Hogan et al. (2000) point out that the Wichita granites fall into the A1 subtype of Eby (1992), which suggests that they may have a source region similar to that of ocean island basalts or hot-spot magmas. This is consistent with the trace element analysis of Weaver and Gilbert (1986), which showed that all of the Wichita granites have a "within-plate" signature. The trace element analysis, however, could not rule out an alkalic lower-crustal source or crustal contamination of the magmas.

Myers et al. (1981) also noted that, based on variation diagrams, the Wichita granites clustered into three distinct groups. These groups were named the Mount Scott, Reformatory, and Mountain Park classes. Gilbert and Myers (1986) pointed out that the Mount Scott class is dominant in the eastern Wichitas while the Reformatory is dominant in the west, with Mountain Park class granites being spread throughout the Wichitas. They also noted that there is no apparent relation of chemical class to age, as some of the oldest granites and some of the youngest share chemical classes.

As previously stated, the Wichita granites were emplaced as thin, laterally extensive sheets. All of the Wichita granites have elevated halogen concentrations and are water-undersaturated. All of the felsic liquids are believed to have been intruded or erupted at very high temperatures, in the range of 900-1000° C (Gilbert, 1982). It is believed that this combination allowed the granites to intrude nonexplosively into the subvolcanic pile at depths of as little as 1 km. The elevated halogen content (especially

fluorine) would have also greatly lowered the viscosity of the magmas, allowing them to spread out over large distances (Hogan and Gilbert, 1997; Hogan et al., 1998, 2000). Non-explosive magma intrusion is a critical part of any attempt to model the emplacement conditions of the Wichita granites, as no caldera structures have been found in the region (Ham et al., 1964). Hogan et al. (2000) suggested that the finer-grained granites are the earlier ones, intruded shallowly, and that grain size of the granites increased with the thickness of the volcanic pile.

2.1.3 End of magmatism: Late Diabase and Rhyolite Dikes

The youngest known igneous rocks in the Wichita Mountains area are a widespread series of igneous dikes known collectively as "Late Diabase", with rarer rhyolitic dikes as well. These dikes are known to cross-cut all of the local igneous units, but are not observed to intrude the Reagan Sandstone which lays atop the youngest Carlton rhyolite flows (Ham et al., 1964; Gilbert, 1982; Gilbert and Hughes, 1986; McConnell and Gilbert, 1990). No radiometric ages have been obtained for these dikes to date. Gilbert and Hughes (1986) performed trace element analyses indicating that there are at least two suites of "Late Diabase", one of which appears to be fueled by the growth of a large mafic layered complex in the middle crust. Field observations by the author show that in at least one location where both rhyolite and diabase dikes occur, the diabase is the younger.

2.2 Long Mountain Granite

The Long Mountain Granite, the focus of this study, was, like all fine-grained Wichita granites first mapped as Lugert Granite by Taylor (1915). Hessa (1964) was the first to do a detailed study of the Long Mountain Granite and suggest that it be considered a separate unit; however, his thesis advisor went on to map it as Mount Scott Granite (Merritt, 1967). Myers et al. (1981) revisited Hessa's work and obtained chemical analyses of four samples of Long Mountain Granite. On the basis of chemistry and petrographic differences, they validated Hessa's claim that it represented a separate unit and admitted it into the formal nomenclature. Reconnaissance chemistry was conducted by Weaver and Gilbert (1986) on a further four samples. Myers et al. (1981) and Gilbert and Myers (1986) placed the Long Mountain into the Mountain Park chemical class. To date, these geochemical analyses have stood as the only additions since Hessa's M.S. thesis work on this granite.

Taylor (1915) made several noteworthy observations in outcrops that were later determined by Hessa (1964) to be either in or near Long Mountain Granite. He described a "fine-grained, grayish-red, hornblende granite…with a predominating micropegmatitic texture" (page 63). Furthermore, on page 64 he notes that, "The fine-grained type is of light pinkish-gray color where exposed, but it is probable that if fresher samples could be obtained they would be a much darker gray." In several places in his report, Taylor attributes the red coloration of the Wichita granites to very fine-grained disseminated hematite, which he hypothesized is produced by the alteration of primary minerals via groundwater.

Hessa (1964) agreed with this hypothesis, and notes on page 11 of his thesis that granite quarries on Long Mountain itself exposed faces showing that the color became gray with depth, as predicted by Taylor, which led to the eventual abandonment of the quarries. A similar situation exists today with the current Martin-Marietta Materials aggregate quarry on Long Mountain. Joey Schulte and Bill Brenton, who supervise operations there, have in multiple conversations told the author that they cannot sell aggregate consisting of only gray or green granite to their main client, a ceramics manufacturer, because the red coloration is what is commercially desirable. The result is that their active quarrying operations today focus mainly on the margins of Long Mountain, where the granites are red, and have not been actively pursuing the green-gray granites.

Hessa (1964) additionally noted that in the field, Long Mountain Granite is moderately to heavily jointed, with joint sets being so numerous and complex as to defy determination of deformation history. In his field sites, he saw that the granite weathers into large boulders. He found small miarolitic cavities in an outcrop roughly west and a little south of Long Mountain that contained feldspar and smoky quartz crystals. At Navajoe Mountain, he identified mafic and hornfelsic inclusions in the granite.

Hessa's (1964) thesis describes the petrography of the Long Mountain Granite, identifying it as a "medium-textured, hypidiomorphic granular, granophyric granite." He noted that the granite is predominantly composed of exsolved feldspars and quartz, with accessory quantities of magnetite, titanite (sphene), hornblende, zircon, epidote, and calcite. He identified hematite, chlorite, and clay minerals as secondary alteration products. The only age relationship he was able to determine is that the Long Mountain

is younger than the Lugert Granite, based on cross-cutting relationships at Navajoe Mountain.

2.3 Paleomagnetism of the Wichita Province

2.3.1 Mafic Rocks

The first study of the paleomagnetism of the Wichita Mountains igneous rocks appears to be that of Ku et al. (1967), which included both mafic and felsic igneous rocks. They sampled five sites of gabbro in the region, only one of which gave a stable site mean. They did determine that the magnetism of the rock was held primarily in nearly pure magnetite; however, the paleopole was late Paleozoic in age, suggesting some sort of alteration. Vincenz et al. (1975) were unable to identify stable remanence components in gabbros and suggested that they contained both secondary magnetizations due to maghemitization and viscous remanence components in unaltered titanomagnetite. Roggenthen et al. (1981) obtained a paleopole that plotted near the 800 Ma and 1300 Ma regions of the then-accepted apparent polar wander path, and favored the older age in their interpretation. They did not, however, include the actual numbers of their pole in their paper, merely giving site means, and no subsequent data has confirmed this interpretation. Hogan et al. (1994) found what they believed to be a primary Cambrian pole in the Mount Sheridan Gabbro, along with a late Paleozoic remagnetization component.

2.3.2 Felsic Rocks

As mentioned in the previous section, the first paleomagnetic study of the Wichita Mountains igneous rocks to yield results was that of Ku et al. (1967), who studied both felsic and mafic igneous rocks. Their granite samples consistently showed that the characteristic remanent magnetization resided primarily in hematite, and yielded a paleopole consistent with that determined for the late Paleozoic. Spall (1968) recorded a paleopole obtained via alternating-field demagnetization that was consistent with late Paleozoic alteration. Using thermal demagnetization, he obtained another pole that he believed to be Cambrian in age. Vincenz et al. (1975) noted that, structurally, the Wichita igneous rocks should only have ever been subjected to up-and-down motion and should thus be suitable for paleomagnetic analysis. They were able to find a few sites which yielded what appeared to be Cambrian poles, but for the most part they were faced with sites that showed evidence of extensive hydrothermal alteration at temperatures of up to 300°C (based on the presence of epidote veins) and yielded late Paleozoic pole positions. Elmore et al. (1998) obtained a presumed primary paleopole from the Cambrian Colbert Rhyolite (likely a part of or at least contemporaneous with the Carlton Rhyolite Group). Price et al. (1998) sampled a drill core of the Mount Scott Granite and found that the magnetic susceptibility increased by approximately a factor of 50 over the course of the first 30 meters, with a corresponding change in color and fracture density. They attributed this to water-caused alteration of primary titanomagnetite to hematite and iron hydroxide minerals. The alteration was judged to be likely either recent or Permian in age, but this was not actually determined.

3. Methods

All samples utilized in the present study were obtained in the Martin-Marietta Materials Snyder Quarry, located west of the town of Snyder, Oklahoma on the west side of Long Mountain.

3.1 Paleomagnetism

For paleomagnetic analysis, 2.5-cm diameter cores were collected from in-situ rocks using a portable gasoline-powered water-cooled drill. Specimiens were oriented in the field using an inclinometer and Brunton compass. Cores were then cut to standard 2.5 centimeter lengths using a dual-blade water-cooled rock saw. The magnetic susceptibility and anisotropy of magnetic susceptibility were measured using an AGICO MFK-FA1 Multifunction Kappabridge. Anisotropy of magnetic susceptibility (AMS) data were analyzed using the Anisoft 4.2 software released by AGICO and written by M. Chadima and V. Jelinek. All calculations are done following Jelinek (1978).

The natural remanent magnetization (NRM) was measured using a 2G-Enterprises cryogenic magnetometer housed in a magnetically shielded room. Specimens were then subjected to one to two treatments of low-temperature demagnetization in liquid nitrogen to remove the effects of multi-domain magnetic minerals (Dulnop et al., 1997; Borradaile et al., 2004). Most were then stepwise thermally demagnetized in an ASC Scientific Thermal Specimen Demagnetizer up to a temperature of 700° C; some were subjected to alternating field (AF) demagnetization up to applied fields of 120mT. Demagnetization data was plotted on Zijderveld (1967) diagrams and analyzed using principle component analysis (Kirschvink, 1980), with site

statistics after Fisher (1953). Directions with mean angular deviations (MAD) greater than 15° were not used in the analysis.

The presence of a 70 cm-thick diabase dike in part of the field area permitted a baked contact test (see pp. 55-58 of Van der Voo, 1993). A site of 8 cores was sampled from the diabase itself, and 9 specimens were collected in a line extending from 10cm to 140 cm (2 dike widths) normal to the trend of the dike.

3.2 Petrography

The process of cutting the paleomagnetic cores to standard length produces in most cases leftover chips. These chips were selected on the basis of paleomagnetic data for petrographic analysis. Fifteen chips were prepared into polished petrographic thin sections of 30 μm thickness by TPS Enterprises of Bellaire, Texas. Additional thin sections were provided by Dr. David London. Thin sections were examined via petrographic microscope in order to determine overall mineralogy and texture of the rock itself as well as to identify magnetic minerals, secondary phases, and alteration textures.

Other selected chips were polished and carbon-coated and, along with selected thin sections, examined via electron microprobe. All image and analysis acquisition was done using the Cameca SX50 at the University of Oklahoma Electron Microprobe Laboratory. The instrument incorporates a PGT Prism 2000 Energy-Dispersive X-Ray Analyzer with a Moxtek polymer window and five wavelength-dispersive spectrometers. Phases were distinguished qualitatively on the basis of backscattered electron imaging and EDXA analysis. EDXA work was done at a 20 keV accelerating voltage with a 10

nA beam current. Backscattered electron images were acquired under the same beam conditions as 1024x1024 pixel arrays. Quantitative analysis by WDS was also done under these beam conditions, and feldspar analysis was assisted by the PC-based SAMx™ automation system. X-ray element mapping by WDS was done using a 50 nA beam current.

3.2.1 Quantitative Analysis

Electron microprobe analyses were performed using WDS and first-order emission lines. Intensity acquisition for all elements used a 2-point linear background model. Background offsets were determined by overlaying WDS spectra for all analyzed elements using Virtual WDS software. Additionally, the spectra were inspected for possible overlaps with other elements that may be present by overlaying spectra of possible contaminants. No significant overlaps were detected.

Feldspars were analyzed for the elements Na, K, Al, Si , Ca, and Fe. Under the beam current used, the alkalis should not be significantly mobile (Morgan and London, 1996). A defocused 20 μm spot was used to integrate bulk compositions of the feldspars, which show fine-scale exsolution. In order to average the compositions across larger areas, transects were chosen using BSE imaging to sample representative areas of exsolved anorthoclase and granophyres.

Spot size was reduced to 2 μm and current increased to 20 nA for analysis of oxide minerals, as they contained exsolution features and were not expected to contain volatiles.. Oxides were analyzed for Si, Ti, Al, Mn, Mg, Cr, Zn, and Fe^{2+}. All pulse

height analyses utilized integral mode, and data reduction employed the PAP method (Pouchou and Pichoir, 1985).

Automated analysis of the feldspars was done both on exsolved anorthoclase crystals and in granophyric regions of the samples. Consequently, many of the analyses done in the granophyric regions were either partially or completely contained within quartz crystals rather than feldspar. As the quartz is irrelevant to the objectives of this study, it was deemed best to remove quartz-contaminated analyses. This was done on the basis of Si atoms per 8 oxygen atoms. Analyses of the anorthoclase and granophyric alkali feldspar consistently had values very near but slightly lower than 3.00. Consequently, it was decided that any point with a calculated Si per 8 oxygen value of greater than 3.1 is contaminated and should be disregarded when calculating feldspar composition averages.

Quantitative analysis was also performed on other silicate phases (pyroxene, amphibole, micaceous minerals) in order to better constrain identity. Beam parameters used in these analyses were the same as for oxides.

WDS analysis was also used in x-ray mapping of Si, Al, Na, K, and Fe. The beam was rastered over a chosen area and Kα emissions counted. Element maps were collected as 256x256 arrays with a 0.2 second dwell time.

3.3 Whole-Rock Geochemistry

Six rock samples were collected in the field for the purpose of detailed whole-rock geochemical analysis. Three representative samples each were chosen from red and green granites. Sample preparation and analysis was performed by Activation

Labaratories (ActLabs) of Ancaster, Ontario. Fluorine was analyzed by Selective Ion Electrode methods. Ferric iron was measured by titration. Other elements and oxides were determined by mass spectrometry.

4. Results – Petrology

4.1 Field Observations

In the field, the Long Mountain Granite is present in two varieties. One is red, and the other has a gray fresh surface but develops a green coating after exposure, and will generally be referred to as green in this paper. The red granite tends to be more heavily fractured than the green, and in some quarry faces the characteristic tor topography can be seen developing beneath the soil (Figure 4.1). In others, a nearly complete progression from solid red granite through spheroidal weathering to soil can be found. Diabase dikes penetrating the red granite tend to be very fissile, sometimes crumbling to powder at a slight touch (Figure 4.2). Epidote-coated fracture surfaces have also been identified in the red granite (Figure 4.3). These have not been observed in green granite.

Figure 4.1. Developing tor topography in red granite. Note heavy fracture intensity.

Figure 4.2. Fissile, altered diabase dikes in red granite. Dikes are ~30 cm thick.

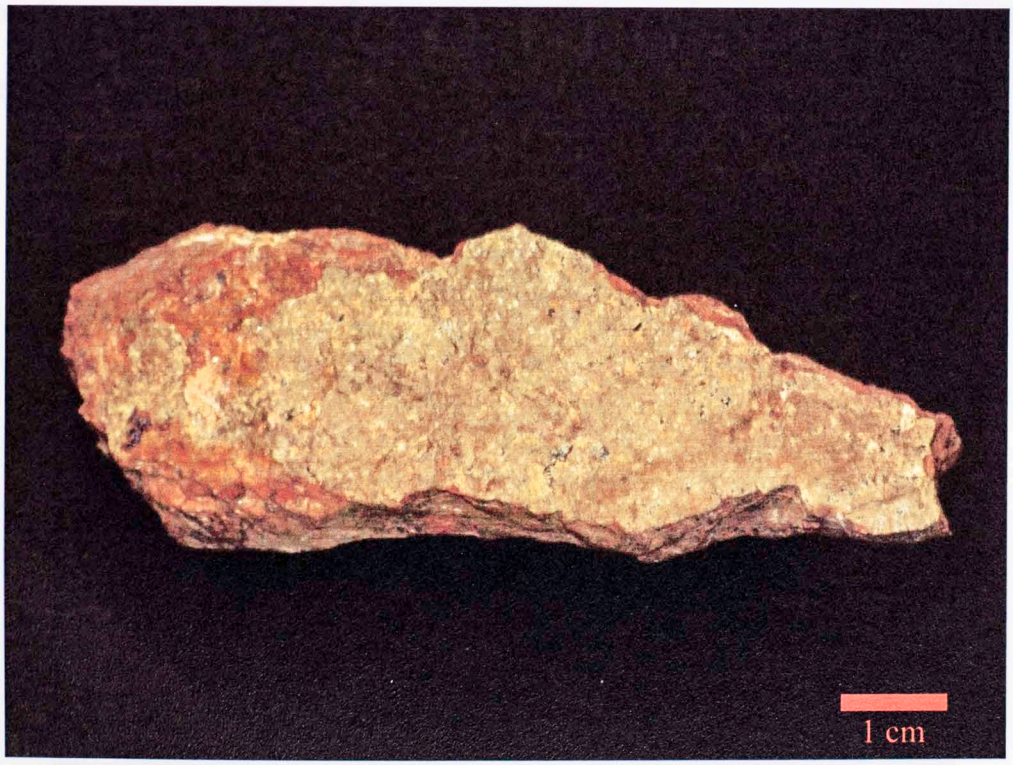

Figure 4.3. Epidote-covered fracture face in a specimen of red granite.

The granite is in several places cut by Late Diabase dikes. In the red granite, these tend to be very fissile, almost shale-like. Those penetrating the green granite tend to be more intact, though heavily fractured in some places. One of these dikes (Figure 4.4) and the adjacent granite were sampled for paleomagnetic analysis. A small near-vertical rhyolite dike is also cut by the diabase in Figure 4.4. At a fine scale, the diabase dike exhibits fingering textures into the rhyolite dike (Figure 4.5). Unusually, some samples of green granite also appear to contain petroleum residues along fracture surfaces (Figure 4.6).

Large fractures in the green granite commonly exhibit strong red coloration around them, and it is not difficult to find boulders of green granite with red rims. In general, the red granite is found in the upper and outer levels of the quarry, as well as in the most fractured zones. It has the general morphology of a carapace around the green granite, penetrating further inwards along fractures in places.

Figure 4.4. 70 cm-thick diabase dike cutting green granite and, in the center, a rhyolite dike.

Figure 4.5. Fingering of diabase dike into rhyolite dike.

Figure 4.6. Organic residue coating a fracture surface in the green granite.

4.2 Whole-Rock Geochemistry

As discussed in Geologic Setting, the petrology of the Long Mountain Granite was first described by Hessa (1964), from samples taken from Navajoe Mountain and other localities, though not from Long Mountain itself. To date, this has only been supplemented by geochemical analyses. Advances in technology since the time of the original description make it possible to perform a more thorough and accurate analysis. For purposes of investigating the alteration history of the rock, it is imperative to have a thorough grasp of both the primary and secondary mineralogy and textures of the granite, and therefore the current study includes updated petrological observations.

Three samples of the green-gray granite (LMGG2, LMGG3, LMGDH1) and three of red granite (LMGR1, LMGR7, LMGR5) from Long Mountain were analyzed for major and trace elements. Table 4.1 contains the data for major element compositions.

Table 4.1. Major Element Composition in Wt. %

	LMGG2	LMGG3	LMGDH1	LMGR1	LMGR7	LMGR5
SiO_2	75.04	75.25	75.06	74.52	74.01	74.31
TiO_2	0.218	0.212	0.217	0.212	0.243	0.222
Al_2O_3	12.14	11.79	12.1	12.11	11.97	11.92
FeO	1.52	1.51	1.59	0.75	1.01	0.7
Fe_2O_3	0.98	1.15	1.19	1.63	1.96	2.05
MnO	0.047	0.045	0.042	0.033	0.033	0.033
MgO	0.10	0.19	0.13	0.19	0.45	0.21
CaO	0.74	0.57	0.63	0.61	0.45	0.65
Na_2O	3.77	3.92	3.93	4.04	3.84	4.01
K_2O	4.77	4.76	4.86	4.47	4.64	4.57
P_2O_5	0.01	0.02	0.01	< 0.01	0.02	0.02
F	0.14	0.14	0.15	0.24	0.15	0.21
LOI*	0.38	0.26	0.24	0.52	0.44	0.56
Total	99.88	99.84	100.2	99.19	99.17	99.32

*** Loss on Ignition has been corrected for the titration of FeO.**

From Table 1, it appears that the red granite is depleted in SiO_2, MnO, and K_2O and enriched in volatiles relative to the green, though these are small deviations (SiO_2 and K_2O by less than 1 wt.%, MnO by 0.01 wt.%, volatiles by about 0.2 wt.%). The change in preferred oxidation state of iron (FeO vs. Fe_2O_3) is quite obvious with average Fe^{2+}/Fe^{3+} dropping from 1.74 to 0.54; however, the total amount of iron is essentially identical (Fe close to 2 wt.%) in red and green. On the whole, the major element composition of the rock indicates that it is a typical alkaline A-type granite (see Bonin, 2007). Relative to an analysis of Mount Scott Granite, the most well-characterized granite of the Wichitas, given in Price et al. (1999), the Long Mountain Granite is more silicic, more potassic, less calcic, and also has less titanium and phosphorus.

Trace element data were also obtained for the same samples (see Table 4.2). Both rare earth element (REE) and other trace element data have been plotted together alongside datasets from Mount Scott Granite (Weaver and Gilbert, 1986). These data show that there is virtually no difference in trace element composition between green and red granite (see figure 4.7). The data are nearly identical with those of the Mount Scott, though the Long Mountain exhibits a stronger negative Eu anomaly and lower phosphorus and titanium abundances, indicating that the magma was somewhat more fractionated than that of the Mount Scott. The data are given in Table 4.2. The abnormally high chromium content is likely contamination introduced during sample preparation.

Table 4.2 Trace Element Composition in ppm

	LMGG2	LMGG3	LMGDH1	LMGR1	LMGR7	LMGR5
Sc	2	2	2	2	2	2
Be	5	6	5	6	5	6
V	< 5	< 5	< 5	< 5	< 5	< 5
Cr	20	30	100	30	90	90
Co	< 1	< 1	< 1	< 1	< 1	< 1
Ni	< 20	< 20	< 20	< 20	< 20	< 20
Cu	10	< 10	< 10	< 10	< 10	< 10
Zn	150	130	140	110	190	90
Ga	26	27	27	26	26	27
Ge	2.1	2.2	2.2	1.8	2.1	2.1
As	< 5	< 5	< 5	< 5	< 5	< 5
Rb	181	173	172	160	157	166
Sr	57	49	55	53	61	53
Y	91.4	94.7	92	94.5	104	95.3
Zr	620	677	662	684	709	660
Nb	66.9	71.6	65.8	64.7	66.8	69.2
Mo	3	3	9	2	10	8
Ag	2.1	2.7	2.4	2.3	2.5	2.2
In	< 0.1	< 0.1	< 0.1	< 0.1	< 0.1	< 0.1
Sn	7	30	8	9	11	8
Sb	< 0.2	< 0.2	< 0.2	< 0.2	< 0.2	< 0.2
Cs	7.8	3.9	5.3	5.1	6	6.4
Ba	1103	1093	1188	1159	1271	1129
La	89.3	90.9	101	95.9	104	90
Ce	197	201	220	211	230	199
Pr	22.3	22.7	24.5	23.5	26.1	22.5
Nd	87.4	90.9	96.7	93.5	104	89
Sm	17.8	18.6	18.9	18.9	20.8	17.7
Eu	2.55	2.57	2.74	2.77	2.97	2.56
Gd	15.3	16	16.2	16.5	17.9	15.6
Tb	2.7	2.79	2.72	2.82	3.07	2.69
Dy	15.5	16	15.7	16.1	17.3	15.5
Ho	2.98	3.13	3	3.12	3.34	3.04
Er	8.98	9.32	8.91	9.09	9.69	8.94
Tm	1.33	1.41	1.35	1.36	1.41	1.37
Yb	9.12	9.54	9.48	9.51	9.65	9.48
Lu	1.37	1.44	1.44	1.43	1.44	1.39
Hf	13.3	14.4	13.8	14.8	14.4	14.2
Ta	4.5	4.73	4.55	4.43	4.02	4.66
W	1.8	1.3	4.3	1.3	2.4	1.5
Tl	0.68	0.65	0.6	0.58	0.56	0.59
Pb	21	29	22	15	17	16
Bi	0.2	0.2	0.2	16.2	0.2	7.1
Th	14.6	15.2	15.5	14.9	14.7	14.9
U	4.58	4.74	4.67	4.98	4.18	4.89

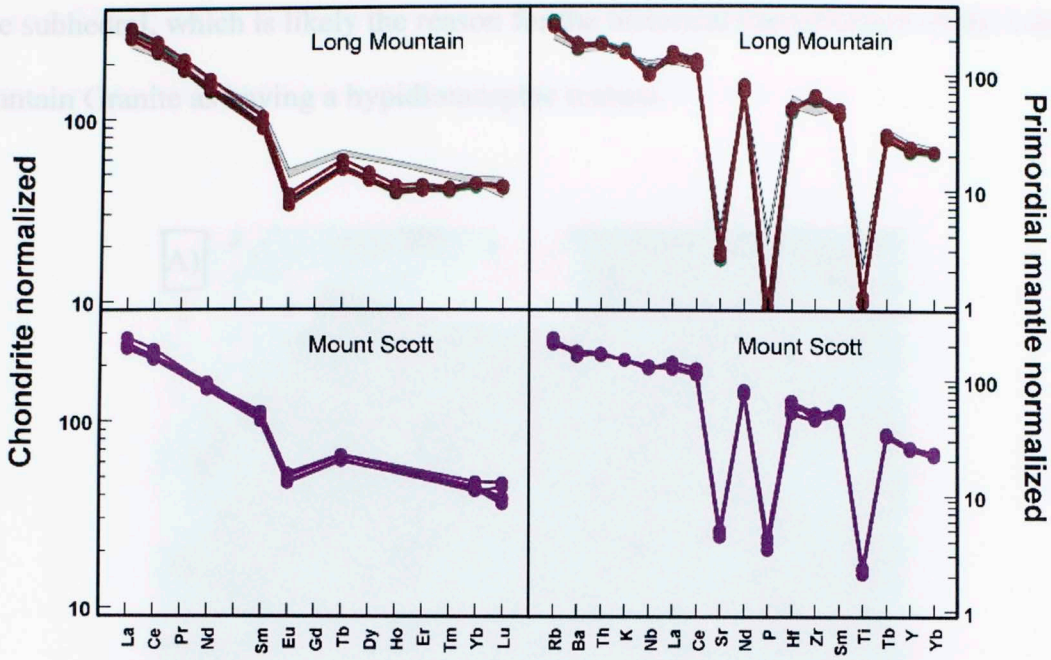

Figure 4.7. Normalized REE and trace element abundances of Long Mountain Granite, with Mount Scott Granite for comparison. Long Mountain Granite analyses represented by green and red points and lines for green and red granite samples respectively, gray shading on Long Mountain plot shows Mount Scott Granite data.

4.3 Petrography

4.3.1 Green Granite

The Long Mountain Granite is a fine-grained microporphyry, with average size of feldspar and quartz grains being on the order of a millimeter or two. The rock is dominantly (>90-95%) composed of quartz and alkali feldspar intergrowths in a myrmekitic to granophyric whole-rock texture (Figure 4.8a). Accessory minerals tend to occur as sub-millimeter crystals in small clusters that may or may not be monomineralic (Figure 4.8b), giving the rock a cumulophyric to glomerophyric texture in addition to the dominant granophyre. Non-granophyric feldspar and accessory mineral grains tend

to be subhedral, which is likely the reason for the historical classification of the Long Mountain Granite as having a hypidiomorphic texture.

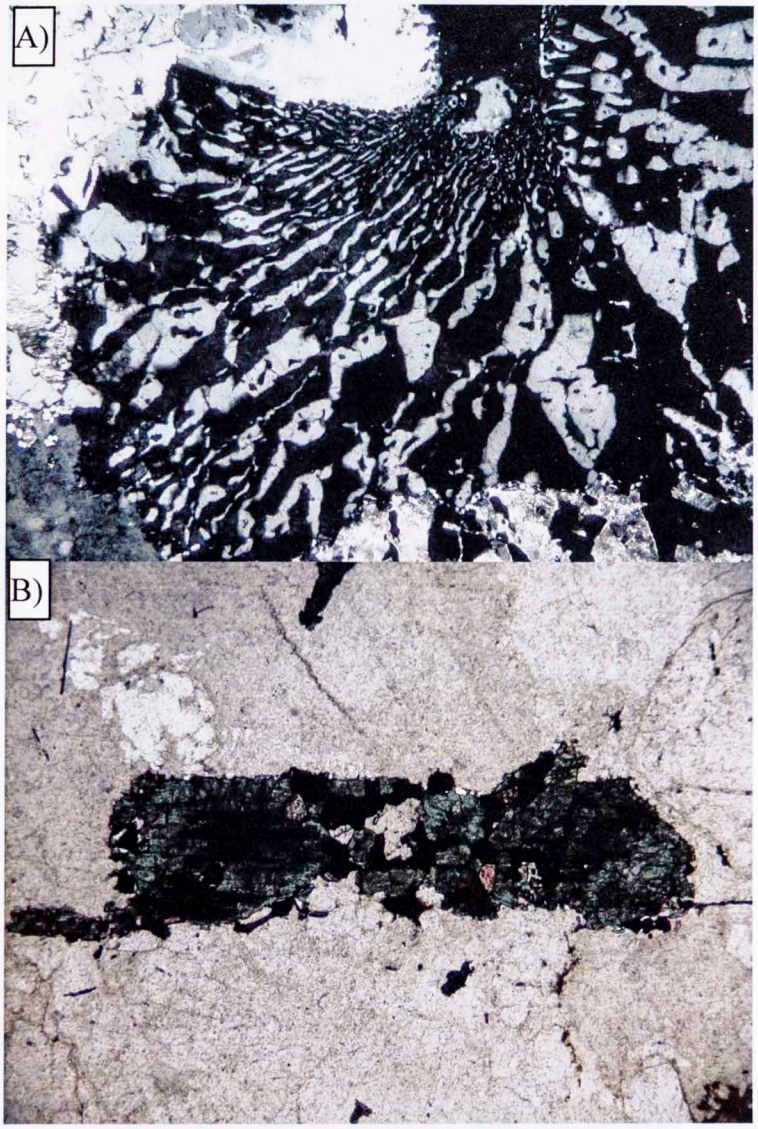

Figure 4.8. A) Myrmekitic quartz-feldspar intergrowth grading into granophyre. Crossed polarizers, 3.5mm field of view. B) Cumulophyric cluster of hedenbergite, fluorite, Fe-Ti oxides, and zircon. Plane-polarized light, 3.5mm field of view.

As previously stated, the vast majority of the rock is composed of intergrown quartz and feldspars. Feldspars are also present as exsolved anorthoclase phenocrysts. These sparingly contain partially resorbed plagioclase cores of compositions as calcic as

An_{21} (see Figure 4.9a). These anorthoclase grains uncommonly have inclusions of other mineral grains, and almost always have a potassium-rich rim (Figure 4.9b).

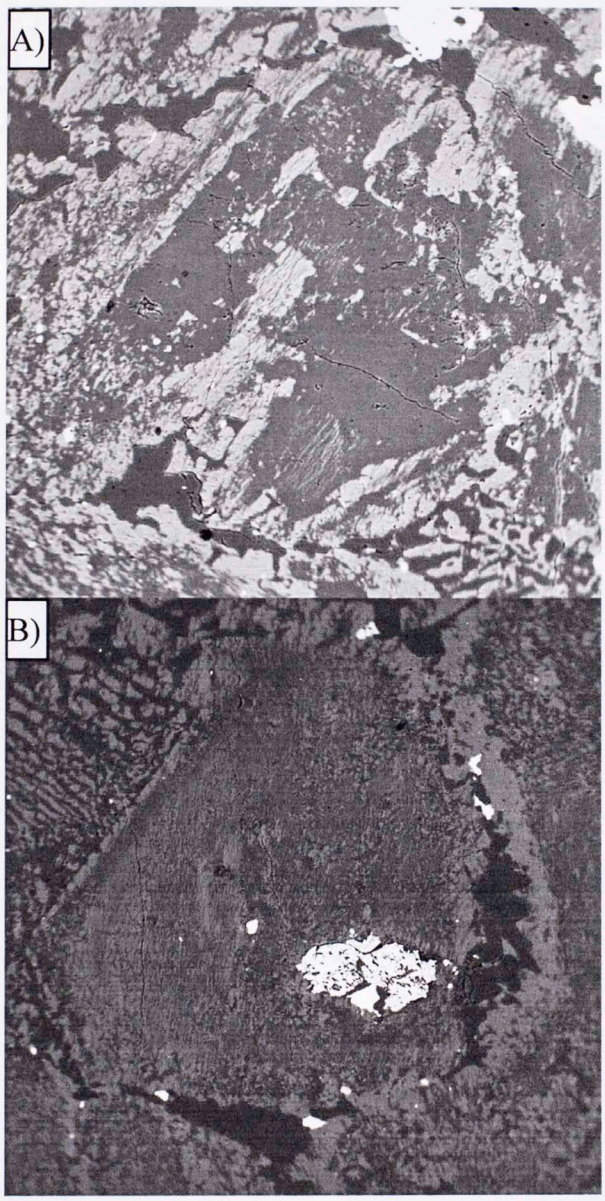

Figure 4.9. A) Anorthoclase phenocryst with partially-resorbed anorthite-rich (up to An21) core. 1317 µm field of view.B) Exsolved anorthoclase phenocryst with hedenbergite inclusion and potassic rim. 1580 µm field of view. Both figures are backscattered electron images.

The feldspars in the rock are, with the exception of the rare plagioclase cores, exsolved alkali feldspars. Both perthite and antiperthite crystals are common. Most

feldspars are finely exsolved, although some exhibit patchy exsolution (Figure 4.10). Even granophyric alkali feldspars exhibit strong exsolution textures.

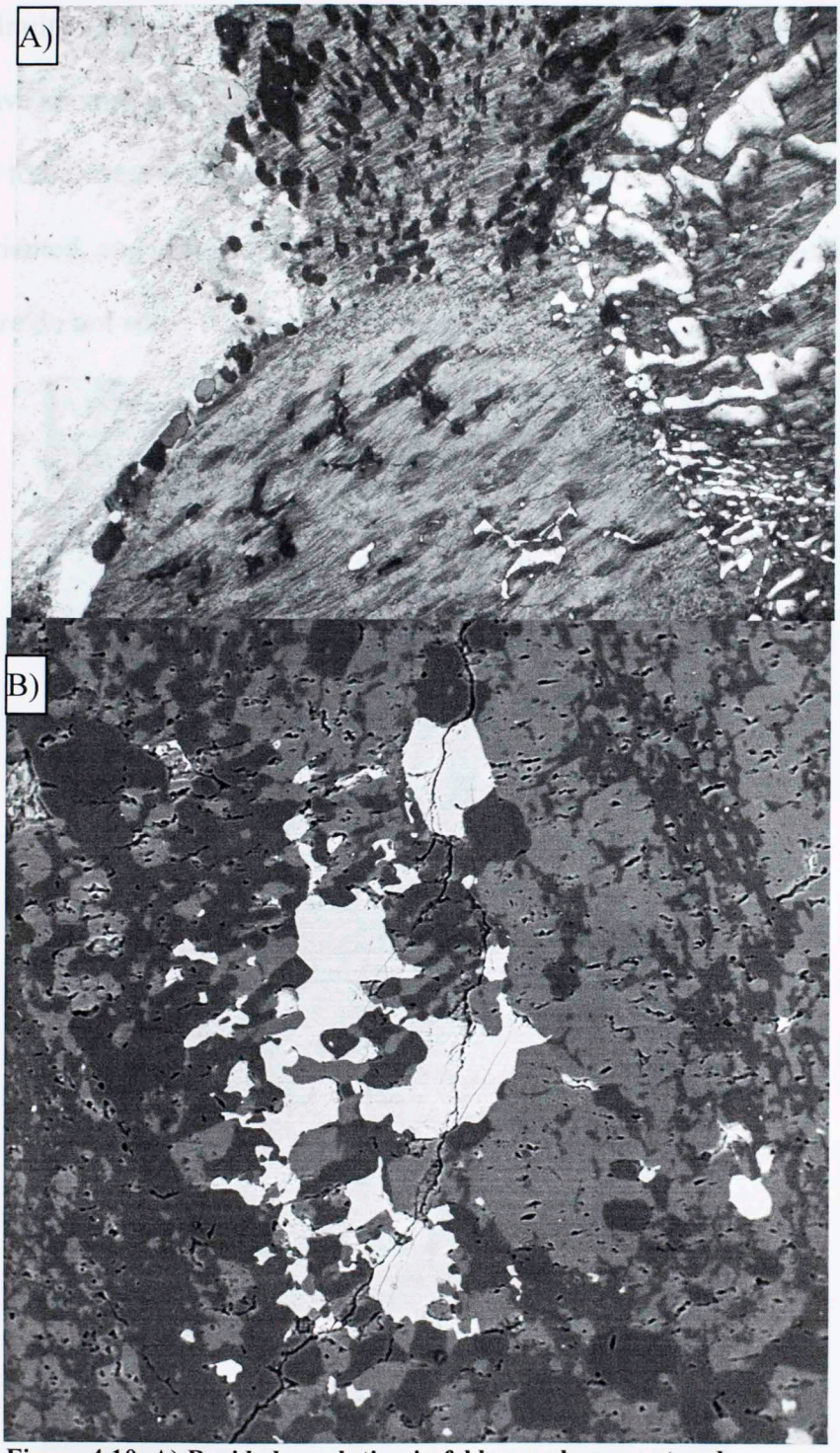

Figure 4.10. A) Braided exsolution in feldspar phenocryst and granophyric feldspars, crossed polarizers, 1.75mm field of view. B) Patchy exsolution in alkali feldspars, backscattered electron image, 790 µm field of view. Bright phase is hornblende.

Quartz, the other major mineral in the Long Mountain Granite, does not appear to be present as phenocrysts. Even the largest, rounded quartz grains exhibit optical continuity with granophyre quartz (Figure 4.11a). Some quartz grains appear to have spongy relict cores in cathodoluminescence imaging; others show what appear to be stress features (Figure 4.11b). These features appear to be randomly oriented, and grains exhibiting them are not typically found together. Those that are do not show the same directions in the lineations.

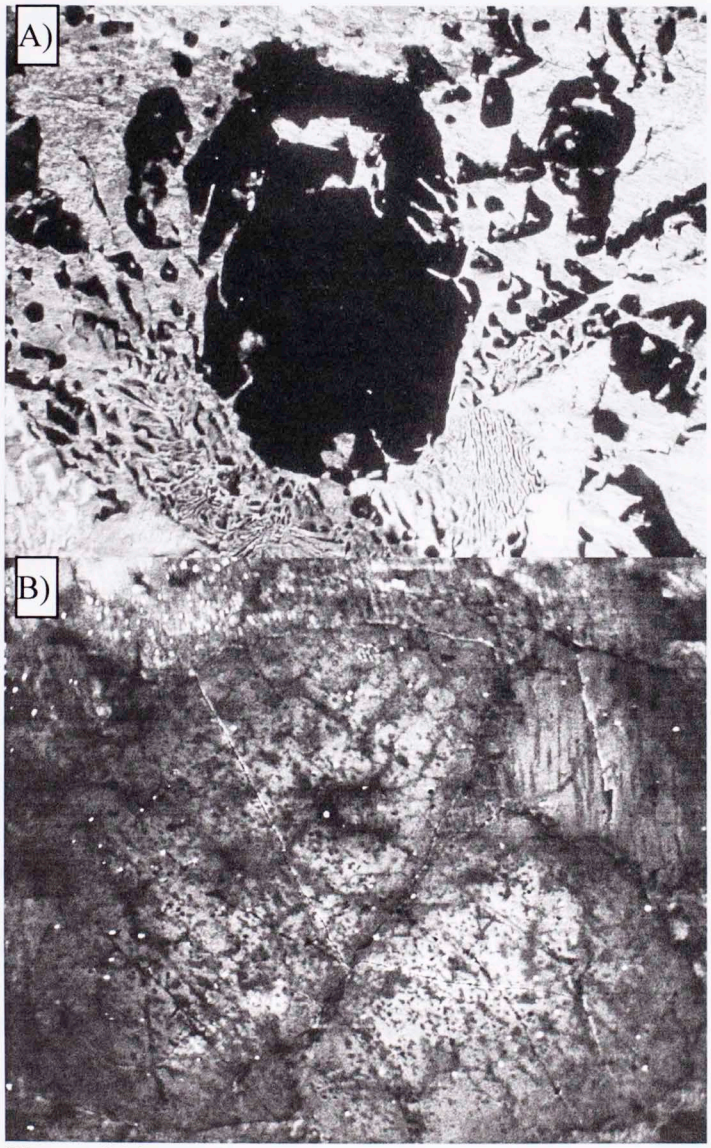

Figure 4.11. A) Quartz grain in optical continuity with granophyre. Crossed polarizers, 3.5 mm field of view. B) CL image of quartz showing spongy relict cores and, inthe upper right grain, stress features. 1436 μm field of view.

In addition to the dominant quartz and alkali feldspars, the Long Mountain Granite contains numerous accessory minerals. The dominant mafic phase appears to be a calcic clinopyroxene; analysis by electron microprobe indicates that this phase is essentially end-member hedenbergite ($CaFeSi_2O_6$). Hedenbergite occurs in a variety of shapes, from nearly euhedral crystals to anhedral blebs. Hornblende, previously reported as the dominant mafic phase (Hessa, 1964), is sparingly present as anhedral masses in some samples, absent in others. Biotite is also sparingly present, although a brown phase that has not been conclusively identified appears to be an alteration product of biotite, indicating that it may have once been a more abundant mineral (Figure 4.12a). The alteration product rarely exhibits a very weak pleochroism and a very strong reddish-brown color. It has a micaceous habit and is easily damaged by steel needle, and contains small rounded grains of biotite. Epidote-group minerals, identified by microprobe as compositionally similar to allanite, are also present.

The most abundant non-mafic accessory minerals in Long Mountain Granite are iron-titanium oxides. Magnetite and ilmenite are present as exsolved grains. Fluorite is frequently present as small grains, both alone and in association with others. Titanite, which has been previously reported as a common accessory mineral (Hessa, 1964), was not found in the current study. This is consistent with the presence of fluorite (Price et al., 1999). Other accessory minerals include zircon, monazite, bastnaesite, and chevkinite. Rare grains of apatite have only been found as cores of monazites or as wholly enclosed inclusions in iron oxides (Figure 4.12b).

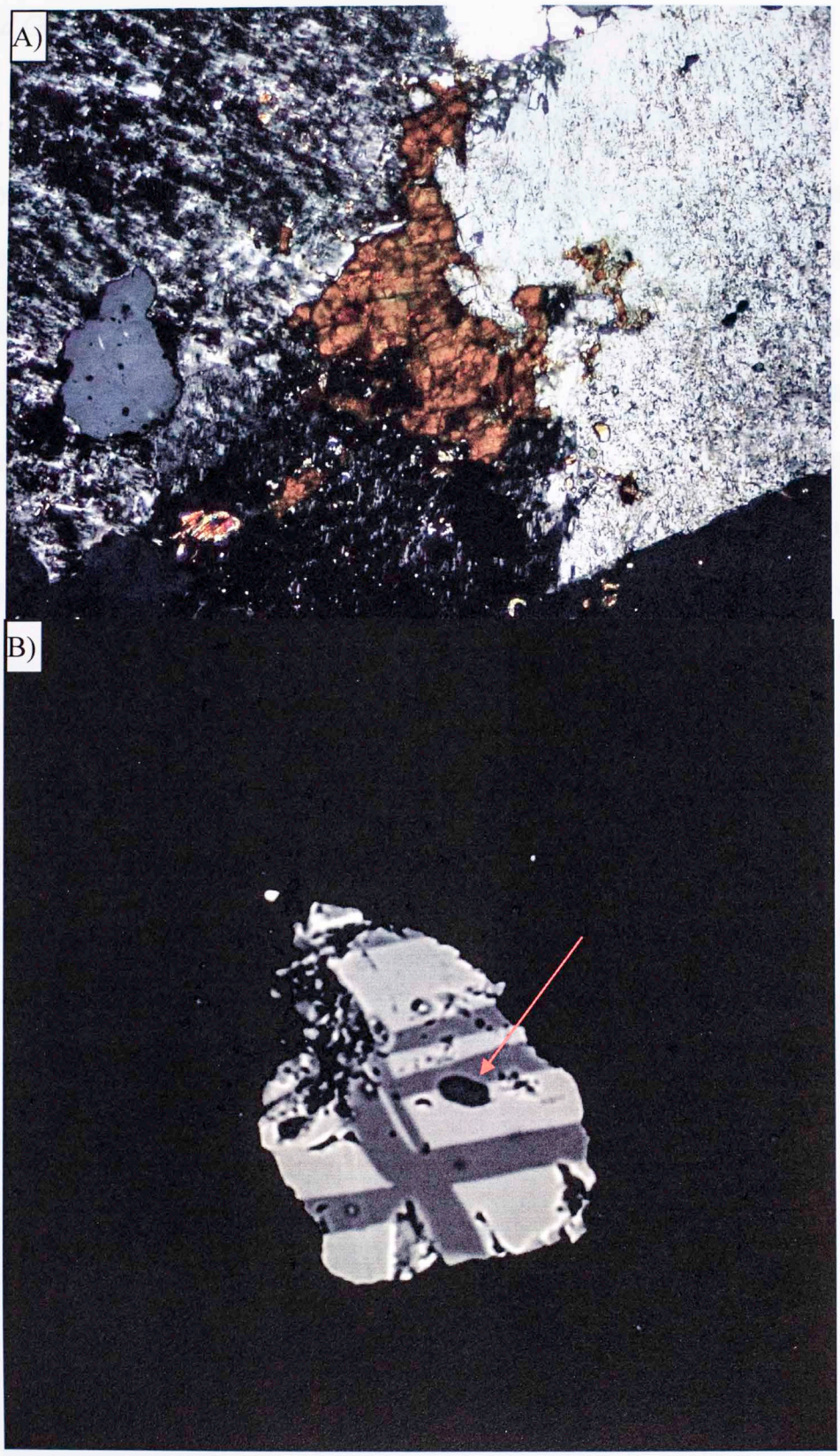

Figure 4.12. A) Brown mineral that appears to be a replacement product of biotite. Brighter rounded grains enclosed are relict biotite. Crossed polarizers, 1.75 mm field of view. B) Magnetite-ilmenite grain with an apatite inclusion (indicated by arrow). Backscattered electron image, 158 μm field of view.

4.3.2 Red Granite

The red granite is in bulk very similar to the green in that it consists mainly of granophyric intergrowths. There are, however, substantial changes in the accessory mineral assemblages. The most obvious change in hand sample is, of course, the red coloration. In thin section, the outstanding difference is that many of the mafic minerals are no longer present. Microprobe analysis indicates that mafic minerals have been altered to a phase that displays what appears to be dessication features and has a chemical composition similar to that of montmorillonite clays (Figure 4.13a). In thin section, these are typically scoured out in the polishing process, leaving behind void spaces (Figure 4.13b). In some cases, these spaces appear to have been evacuated of mafic alteration products prior to sampling, and contain secondary phases such as epidote-group minerals, calcite, and amorphous silica (Figure 4.14). The feldspars also exhibit evidence of substantial alteration such as deep hematite staining, sericitization, and evidence of recrystallization associated with fractures (Figures 4.14b, 4.5). The red granite contains abundant hematite-filled fractures, and strong hematite staining associated with fractures and crystal boundaries is pervasive in a substantial part of the rock (Figure 4.14b).

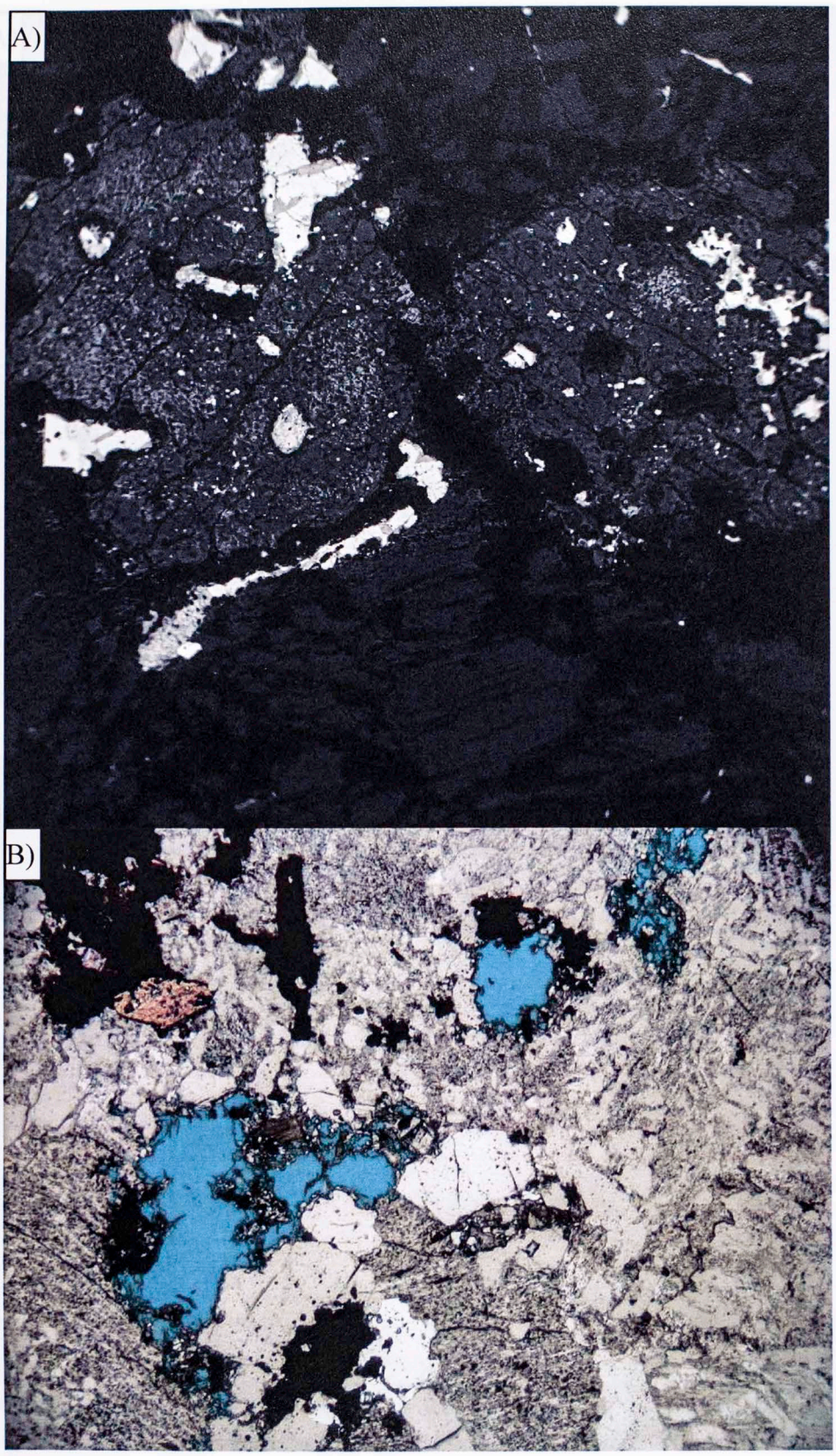

Figure 4.13. A) Mafic grains altered to clays. Backscattered electron image, 1580 μm field of view. B) Void spaces formerly occupied by mafic phases in red granite. Plane-polarized light, 3.5 mm field of view.

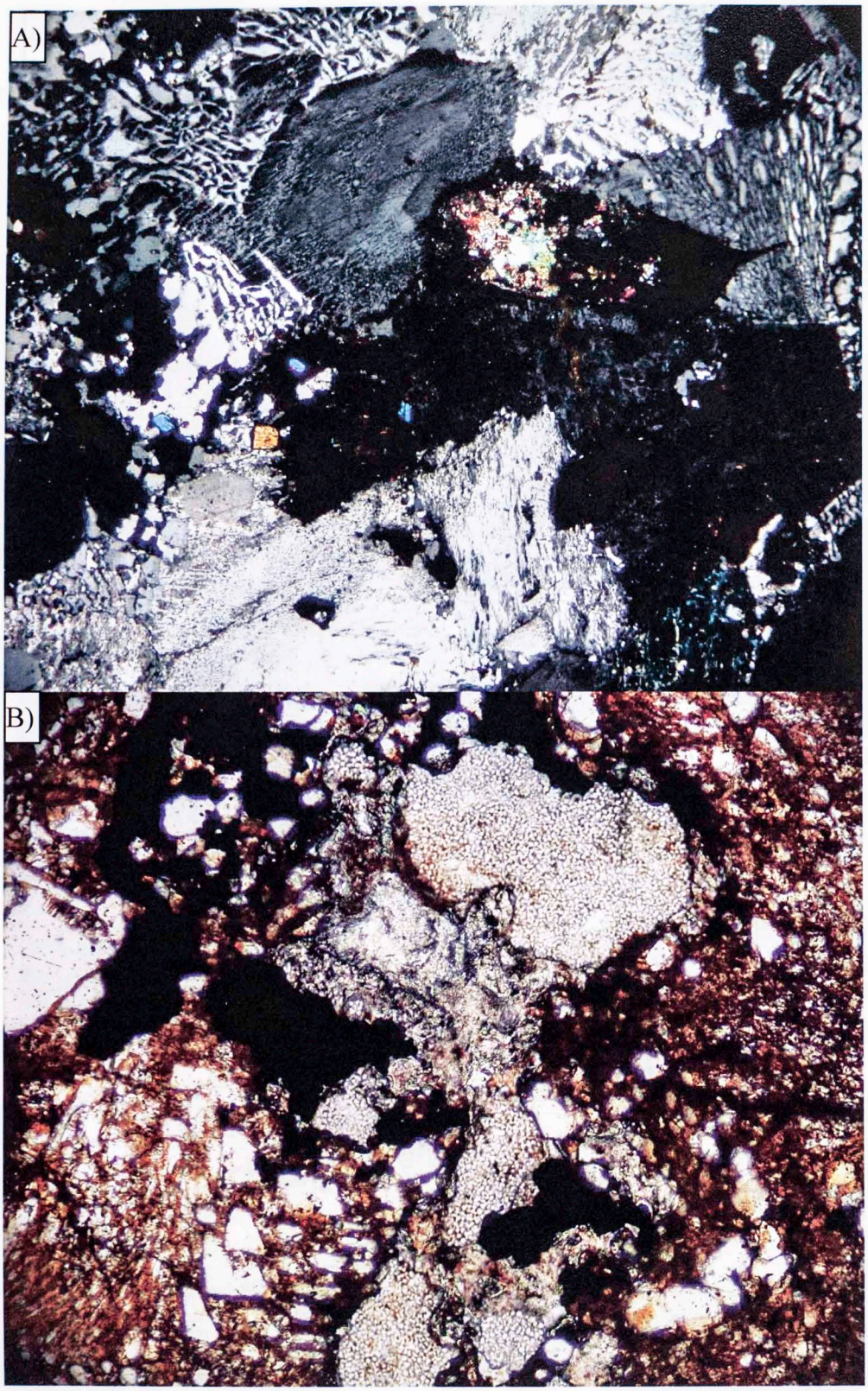

Figure 4.14. A) Relict mafic grains replaced by clays, epidote-group minerals, and calcite. Cross-polarized light, 3.5 mm field of view. B) Void space filled in with amorphous silica. Intense red staining in feldspars and around grain boundaries. Plane-polarized light, 1.75 mm field of view.

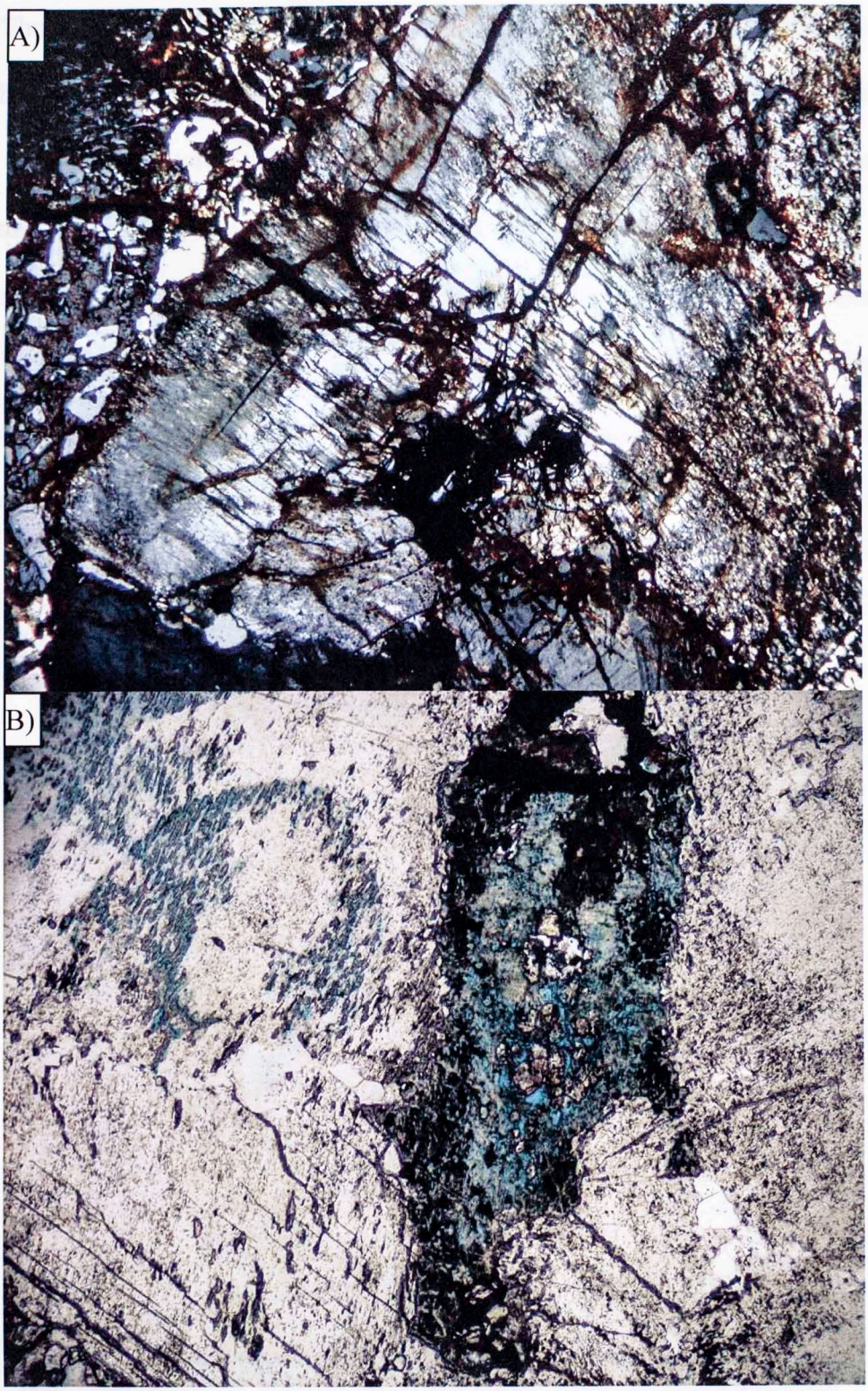

Figure 4.15. A) Feldspar crystal showing hematite staining, sericitization, and recrystallization along fractures. 3.5 mm field of view, cross-polarized light. B) Secondary porosity in feldspars, also a partially-scoured relict mafic grain. 1.75 mm field of view, plane-polarized light.

The hematite staining in the feldspars is largely associated with fractures, although it also commonly takes advantage of perthite lamellae in crystals that retain braided exsolution textures, as visible in Figure 4.15a. Iron oxide grains in the red granite tend to appear slightly red in thin section, and red staining is often seen emanating from them. Quantitative analysis using wavelength-dispersive spectrometry on the electron microprobe shows clear clustering of iron-titanium oxide compositions, one cluster for each color of granite. The cluster for red granite is very close to the ideal for hematite; that for green granite is close to that for ideal magnetite (Figure 4.16).

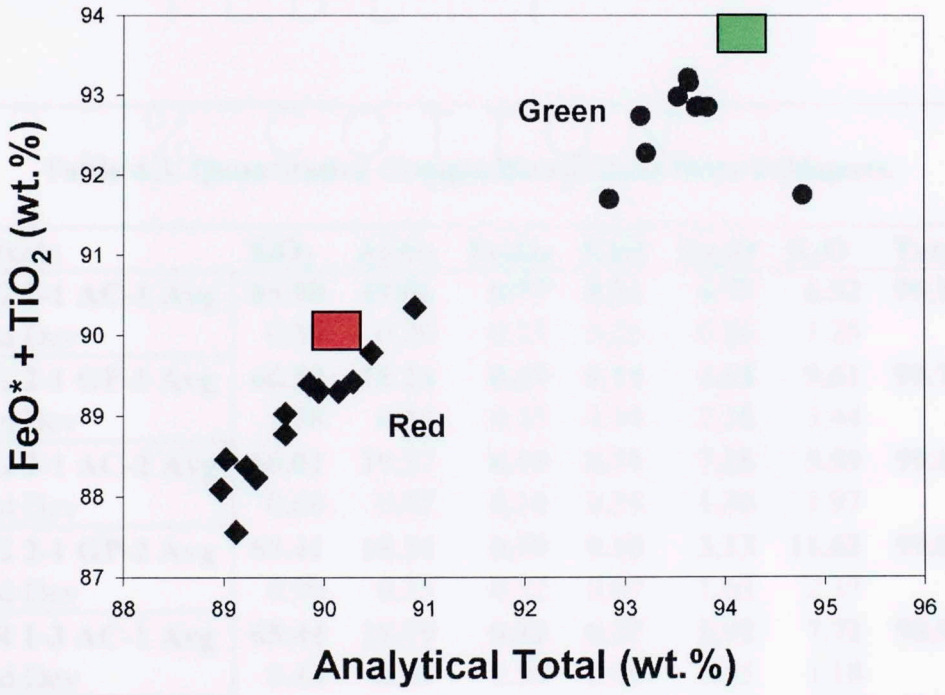

Figure 4.16. Quantitative WDS analyses of Fe-Ti oxide compositions. The ideal compositions for hematite and magnetite are indicated by red and green boxes respectively. Calculations were done assuming all iron as Fe^{2+}.

4.3.3 Distribution of Iron

Quantitative analyses of iron concentration (calculated as Fe_2O_3) were performed along transects in anorthoclase and granophyre feldspars (Figures 4.17, 4.18). Results appear in Table 4.3. Lines designated AC come from anorthoclases; GP indicates granophyre. Iron is consistently higher in granophyric feldspars than in anorthoclases, and consistently higher in the feldspars of red granite than in those of green. High standard deviations are accounted for by inhomogeneity. These data also show that the composition of the alkali feldspars is quite variable between granophyre and anorthoclase phenocrysts. The phenocrysts have subequal Na/K in terms of weight percent, while granophyres are substantially more potassic and less calcic.

Table 4.3. Quantitative Compositional Data from Feldspars.

Oxide	SiO_2	Al_2O_3	Fe_2O_3	CaO	Na_2O	K_2O	Total
SG 2-1 AC-1 Avg	**65.90**	**19.06**	**0.37**	**0.51**	**6.73**	**6.52**	**99.10**
Std Dev	0.36	0.26	0.23	0.25	0.86	1.25	
SG 2-1 GP-1 Avg	**66.58**	**18.24**	**0.49**	**0.14**	**4.65**	**9.61**	**99.70**
Std Dev	1.38	0.45	0.25	0.14	2.28	3.44	
SG 2-1 AC-2 Avg	**66.01**	**19.37**	**0.19**	**0.71**	**7.26**	**5.59**	**99.14**
Std Dev	0.60	0.47	0.10	0.59	1.30	1.97	
SG 2-1 GP-2 Avg	**65.41**	**18.24**	**0.59**	**0.10**	**3.13**	**11.62**	**99.09**
Std Dev	0.90	0.25	0.32	0.07	1.65	2.37	
SR 1-3 AC-1 Avg	**65.44**	**18.79**	**0.82**	**0.27**	**5.92**	**7.72**	**98.97**
Std Dev	0.43	0.21	0.53	0.09	0.85	1.18	
SR 1-3 GP-1 Avg	**65.78**	**18.43**	**1.51**	**0.09**	**5.10**	**9.06**	**99.98**
Std Dev	1.11	0.43	1.12	0.10	3.41	4.77	
SR 1-3 AC-2 Avg	**65.70**	**19.21**	**0.48**	**0.42**	**6.75**	**6.65**	**99.22**
Std Dev	0.53	0.22	0.51	0.28	0.75	1.03	
SR 1-3 GP-2 Avg	**64.56**	**17.64**	**1.00**	**0.10**	**3.92**	**9.91**	**97.12**
Std Dev	0.37	1.30	1.11	0.12	4.83	8.25	

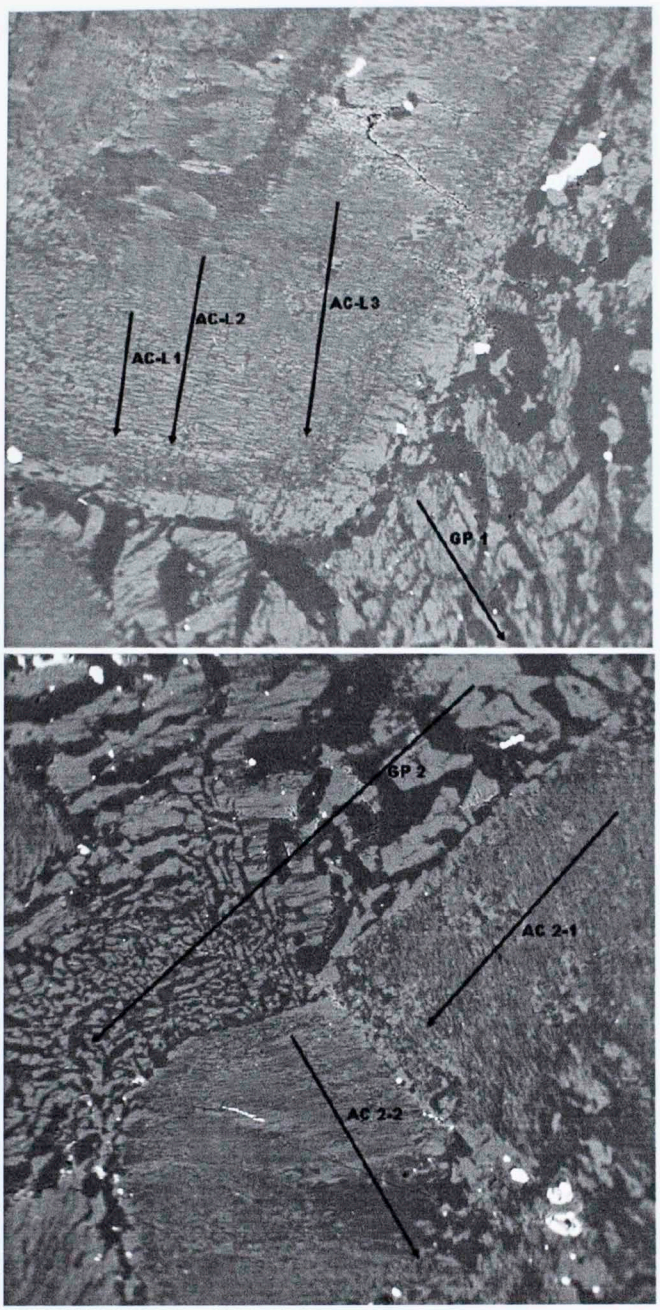

Figure 4.17. Transect lines used for quantitative analysis represented in Table 4.3 from sample SG 2-1. Arrows indicate direction of progressive analyses. 1580 μm field of view.

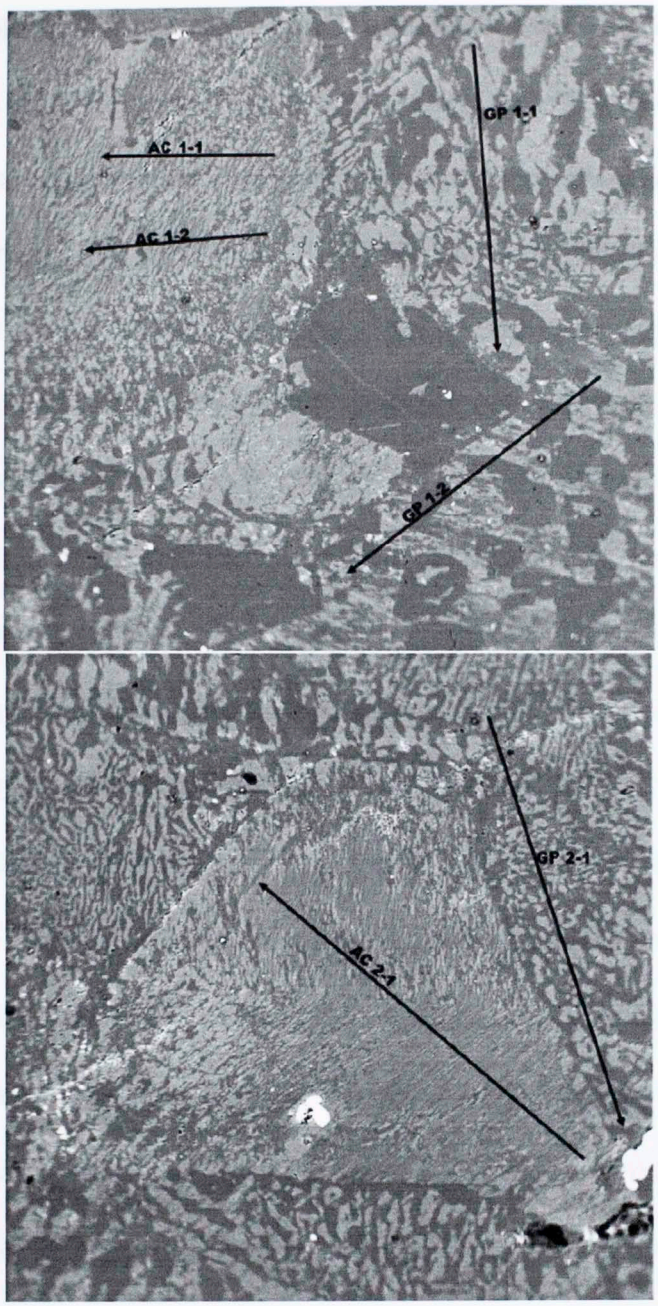

Figure 4.18. Transect lines used for quantitative analysis represented in Table 4.3 from sample SR 1-3. Arrows indicate direction of progressive analyses. 1580 μm field of view.

X-ray mapping of element concentrations in 351x351 μm areas reveals little detectable iron in the feldspars of green granite, whereas in red granite, count rates can exceed 1000 counts per second. Bright spots in the element maps for iron can correlate with pits in the surface of the sample, and these pits likely contained iron-titanium oxide

crystals that were plucked out during sample preparation. Iron abundance in the feldspars of the red granite appears to correlate roughly with increased sodium and decreased aluminum concentrations, possibly indicating some structural substitution in recrystallized feldspars and a preferential recrystallization of albite-rich zones. BSE imaging also shows numerous high-scattering threadlike phases in the feldspars which are consistent with exsolution-plane or cleavage-plane deposition of hematite.

Comparison with backscattered electron imaging shows that most of the more prominent examples of Fe/Al correlations are also correlated with sample topography. As Fe and Al were measured on different spectrometers at different angles, negative correlation between them that follows topography must be considered an artifact in the data. The element maps are shown in Figures 4.19-4.20.

The x-ray map for iron and the corresponding backscattered electron image used in Figure 4.20 were subsequently investigated via image processing via thresholding. For the x-ray map, the lower 50% of the graytone range was discarded as noise; for the BSE image, everything fitting the bimodal distribution of k-feldspar and albite/quartz and below was discarded and only graytones of values between 160 and 255 were included. The thresholded low-resolution x-ray map (Figure 4.21) suggests that about 7% of the area is occupied by iron-rich phases; the same procedure applied to the corresponding backscattered image (Figure 4.22) shows that approximately 4.7% of the area contains these phases. It is prudent to note that the BSE image was not edited to exclude hematite appearing in fractures where incompetent minerals would have been plucked out by polishing; ergo 4.7% is considered an overestimate of the abundance of hematite in feldspar in red granite.

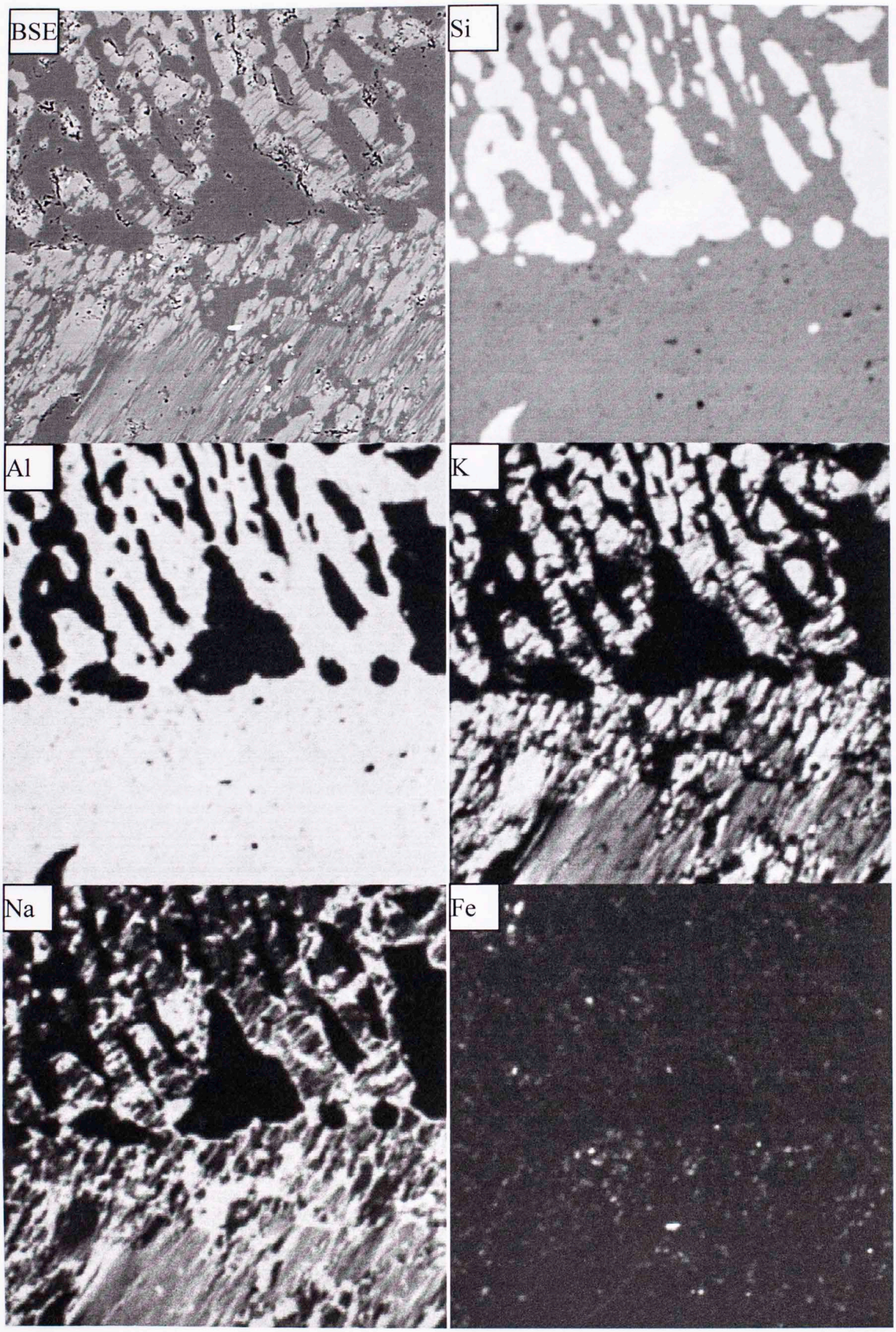

Figure 4.19. Elemental abundance maps in an area of sample SG 2-1. 351 μm field of view.

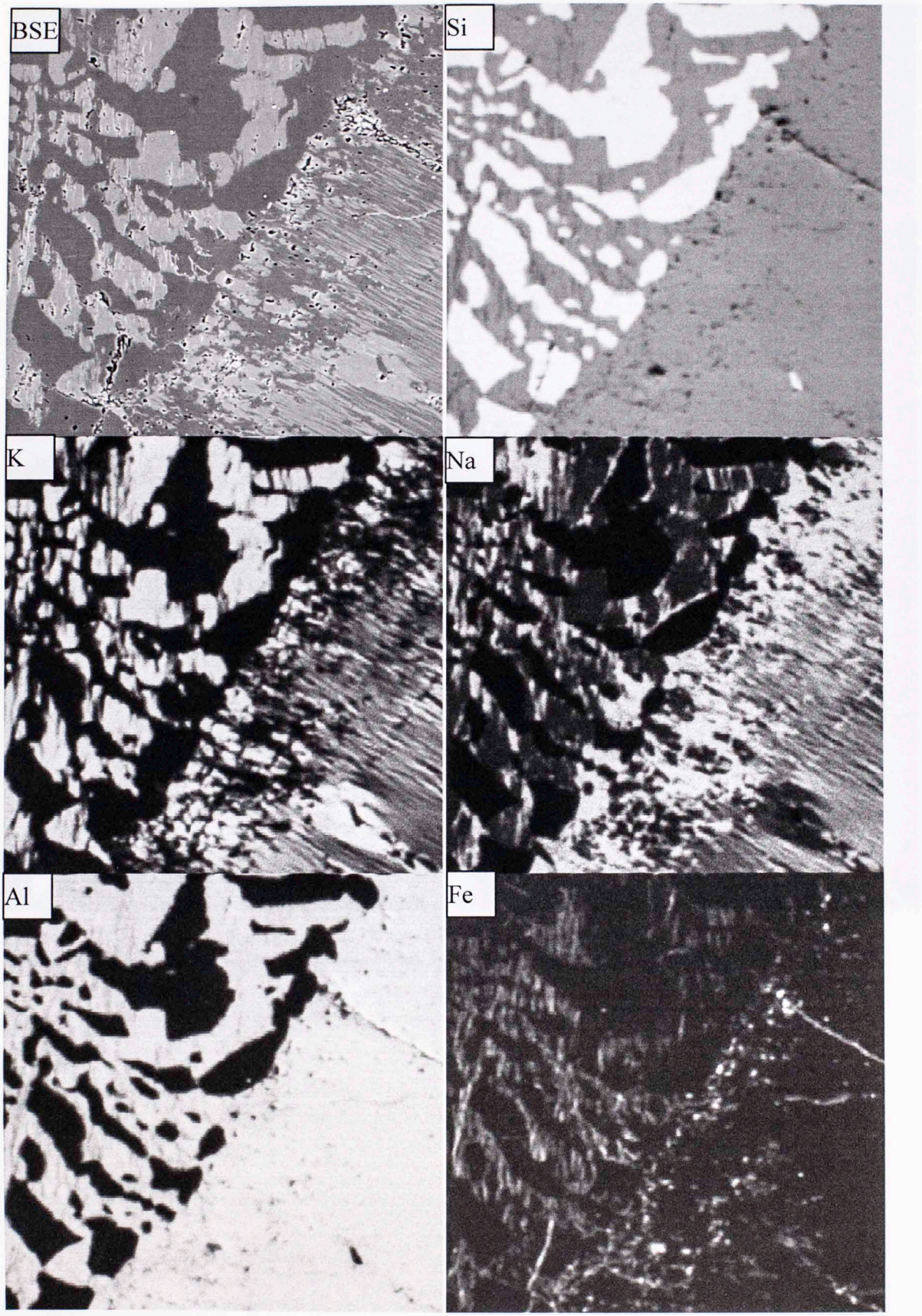

Figure 4.20. Elemental abundance maps from an area of sample SR 1-3. 351 μm field of view.

Figure 4.21. Thresholded x-ray map of Fe from Figure 4.20. Approximately 7% of the area is calculated to contain hematite. Fractures have been erased prior to thresholding and calculation.

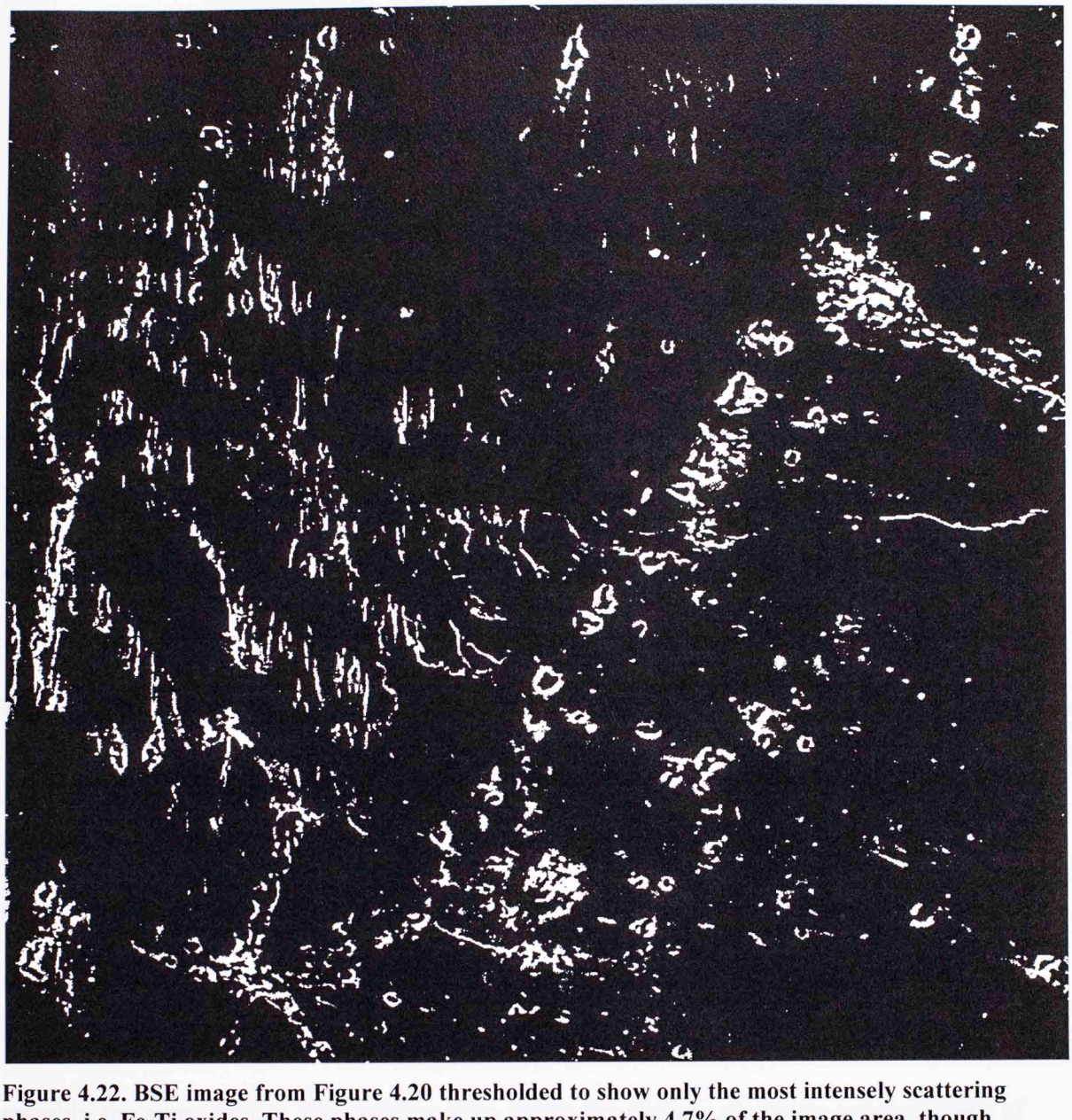

Figure 4.22. BSE image from Figure 4.20 thresholded to show only the most intensely scattering phases, i.e. Fe-Ti oxides. These phases make up approximately 4.7% of the image area, though abundance in fractures and holes left by plucked grains makes this an overestimate of hematite in feldspar. Note wormlike habit of hematite in the center part of the image corresponding to exsolved granophyre feldspars.

5. Results – Paleomagnetism and Rock Magnetism

5.1 Bulk Susceptibility and Natural Remanent Magnetization (NRM)

Table 5.1 lists the mean magnetic susceptibility and natural remanent magnetization (NRM) intensities for the specimens from the sites used in paleomagnetic analysis. NRM intensities displayed a wide range of values, with site SG 5 showing over an order of magnitude of variation. For this reason, median values are given rather than means, which would be strongly skewed for some sites. Sites SG 1-5 and SDH 1 are green granites, site SDD 1 is from a diabase dike, and sites SR 1, ST 1-2, and SQR 1-2 are from red granite. The NRM values are significantly higher in the green granite than the red granite.

The green granite also has a much higher average magnetic susceptibility than the red; in fact all sites in green granite have mean susceptibility more than two orders of magnitude higher than sites SQR 1 and 2. This is consistent with the findings of Price et al. (1998) in their study of effects of weathering on the magnetic properties of the Mount Scott Granite in drill core. Median NRM intensity for red granite is lower by roughly the same factor. The diabase dike yields the highest magnetic susceptibility of all sites, but its remanence intensity is lower than that of green granite by approximately a factor of three.

Table 5.1. Mean susceptibility and median NRM intensity, Long Mountain Granite

Site	Mean Susceptibility (SI)	Median NRM Intensity (mA/m)
SG 1	2.18E-02	156.6
SG 2	2.48E-02	188.75
SG 3	2.15E-02	177.1
SG 4	2.93E-02	330.85
SG 5	2.28E-02	276.25
SDH 1	2.70E-02	222.4
SDD 1	3.27E-02	73.02
SR 1	4.89E-04	4.63
ST 1	3.24E-04	1.215
ST 2	8.90E-04	4.841
SQR 1	1.69E-04	2.1
SQR 2	1.68E-04	3.946

5.2 Anisotropy of Magnetic Susceptibility

Site-mean results are given in Table 5.2. From the data, it is immediately apparent that there is a discrepancy in the degree of anisotropy between the red and green granite. The sites in the green granite all have approximately 3 – 4% anisotropy of magnetic susceptibility (AMS), whereas only one site in red granite even exceeds 1% mean anisotropy.

Table 5.2. Anisotropy magnitude and principal susceptibility axes

Site	Anisotropy degree	K_1	K_2	K_3
SG 1	1.035	N/A	N/A	N/A
SG 2	1.044	72.6, 9.7	340.5, 0.5	249.3, 80.3
SG 3	1.045	184.7, 1.7	94.0, 22.8	278.8, 67.1
SG 4	1.028	93.1, 5.0	359.6, 34.4	190.4, 55.2
SG 5	1.033	122.4, 14.6	212.6, 0.9	305.9, 75.3
SDH 1	1.043	99.7, 8.6	190.3, 4.3	306.5, 80.4
SDD 1	1.040	52.6, 24.7	159.4, 32.1	292.5, 47.5
SR 1	1.012	325.7, 61.1	140.3, 28.8	231.6, 2.3
ST 1	1.008	16.2, 45.8	139.9, 28.4	248.6, 30.7
ST 2	1.006	N/A	N/A	N/A
SQR 1	1.008	7.7, 38.5	249.1, 31.0	292.5, 47.5
SQR 2	1.008	344.1, 54.2	227.2, 18.0	126.5, 29.7

Note: Sites SG 1 and ST 2 were not represented by sufficient samples to allow calculations of principal axes.

Figure 5.1 shows the principal axes calculated for the sites in green granite. Axes K_1 and K_2 appear to be nearly interchangeable, being roughly north-south and east-west, and axis K_3 is near-vertical in 3 of 5 sites. K_1 is the magnetic lineation, and K_3 is perpendicular to magnetic foliation (Archanjo et al., 1994, 2002). Thus, these data indicate that magnetic foliation is subhorizontal, with lineation having a variety of possible directions. This may represent a primary magmatic fabric, as the Wichita granites are essentially large sills and K_3 is commonly normal to the plane of dikes when primary fabric is preserved (Rochette et al., 1991, 1992; Ferré et al., 1999).

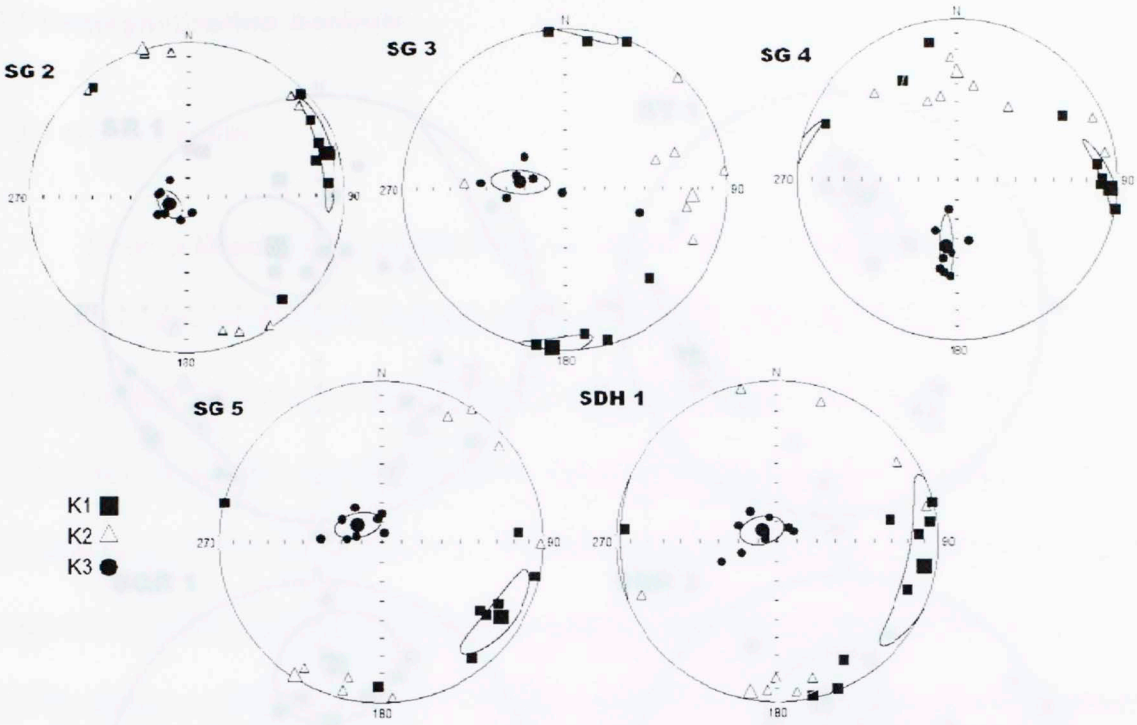

Figure 5.1. Principal axes of magnetic susceptibility in green granite paleomagnetic sites.

Figure 5.2 shows the principal axes for sites in red granite. No axis is as nearly vertical as K_3 in the green granite. Magnetic lineation points somewhat north in all sites, with K_2 and K_3 alternating between NE-SW and southeasterly. The fabric of the red granite is decidedly different than that of the green granite, and therefore is not likely to represent a magmatic fabric. Previous studies of AMS in reddened granites have suggested that the primary fabric is not preserved in them (e.g., Archanjo et al., 2009).

Figure 5.3 displays magnitude of anisotropy (P) plotted against maximum susceptibility (Km) and shape parameter (U). The much higher magnetic susceptibility of green granite is apparent, as is its commonly higher degree of anisotropy. There is also a difference in shape parameter – red granite does not appear to favor any particular shape parameter, whereas green granite is dominated by positive U, i.e. the AMS ellipsoid is oblate (Jelinek, 1978).

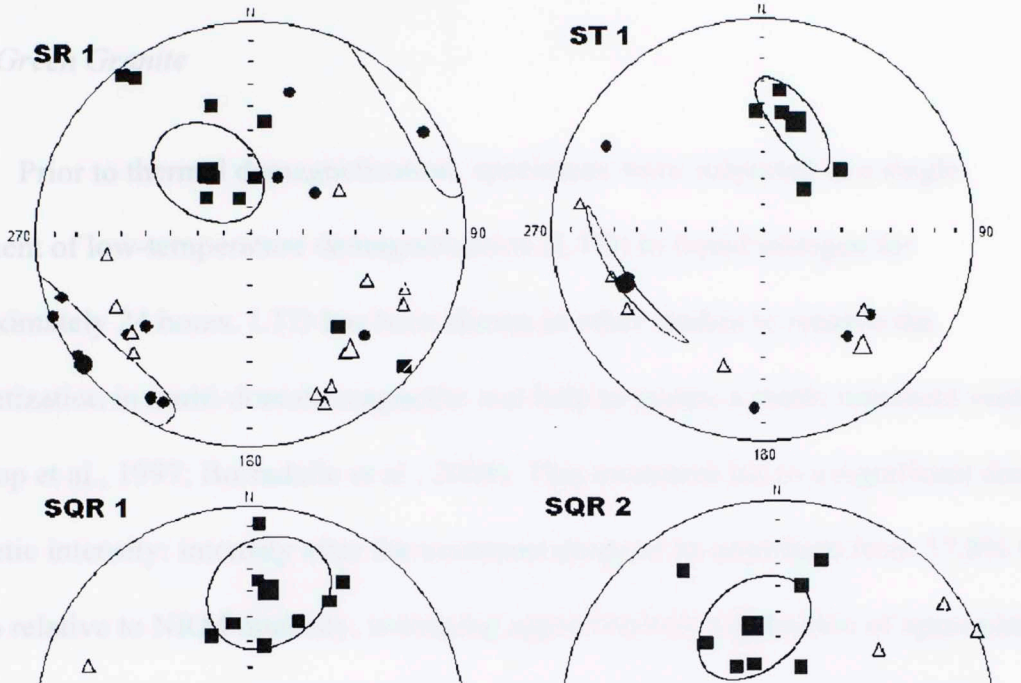

Figure 5.2. Principal axes of magnetic susceptibility in red granite.

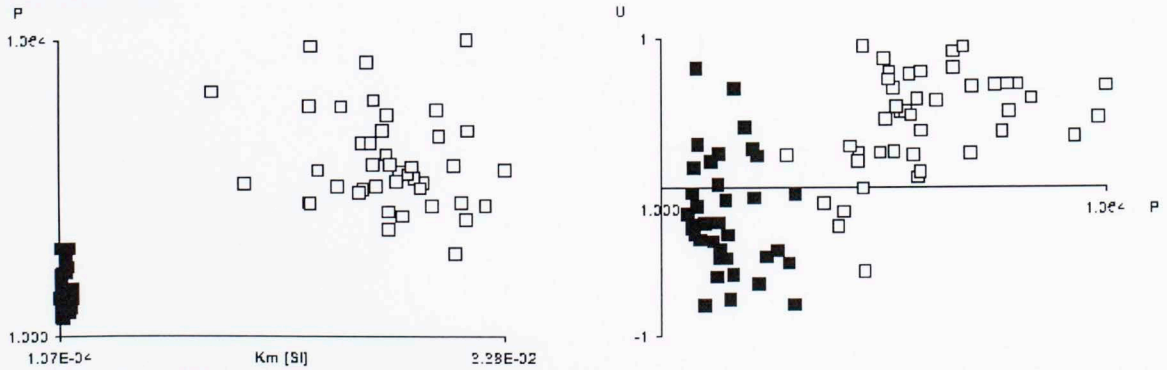

Figure 5.3. (Left) Magnetic anisotropy (P) vs. maximum susceptibility. (Right) Shape parameter vs. P. Closed symbols – red granite, Open symbols are green granite.

5.3 Demagnetization Analysis

5.3.1 Green Granite

Prior to thermal demagnetization, specimens were subjected to a single treatment of low-temperature demagnetization (LTD) in liquid nitrogen for approximately 24 hours. LTD has been shown in other studies to remove the magnetization in multi-domain magnetite and help to isolate a stable remanent vector (Dunlop et al., 1997; Borradaile et al., 2004). This treatment led to a significant drop in magnetic intensity: intensity after the treatment dropped by anywhere from 57.8% to 80.7% relative to NRM intensity, averaging approximately a reduction of approximately 70% (Figure 5.4) for green granite. During thermal demagnetization, all samples showed complete decay by 580°C, indicating that the remanence is likely dominated by magnetite. Additional specimens were demagnetized by alternating field methods and decayed by 120mT; these specimens were not oriented and are not used in the present analysis.

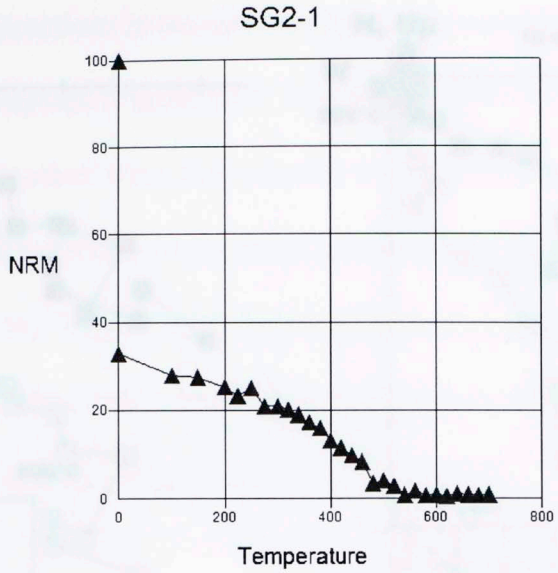

Figure 5.4. Thermal decay profile of sample SG 2-1, showing intensity drop of 67.2% after liquid nitrogen treatment and full decay by 520°C.

Thermal demagnetization of green granite specimens removes a characteristic remanent magnetization (ChRM) with approximately ESE declination and down inclination. The modern viscous remanent magnetization (VRM) is not typically observed in thermal demagnetization data, which is consistent with its removal by LTD. This component is removed in most specimens by 500°C but can persist to 520-540°C (Figure 5.5). Mean angular deviation (MAD) values for this component were typically less than 10°.

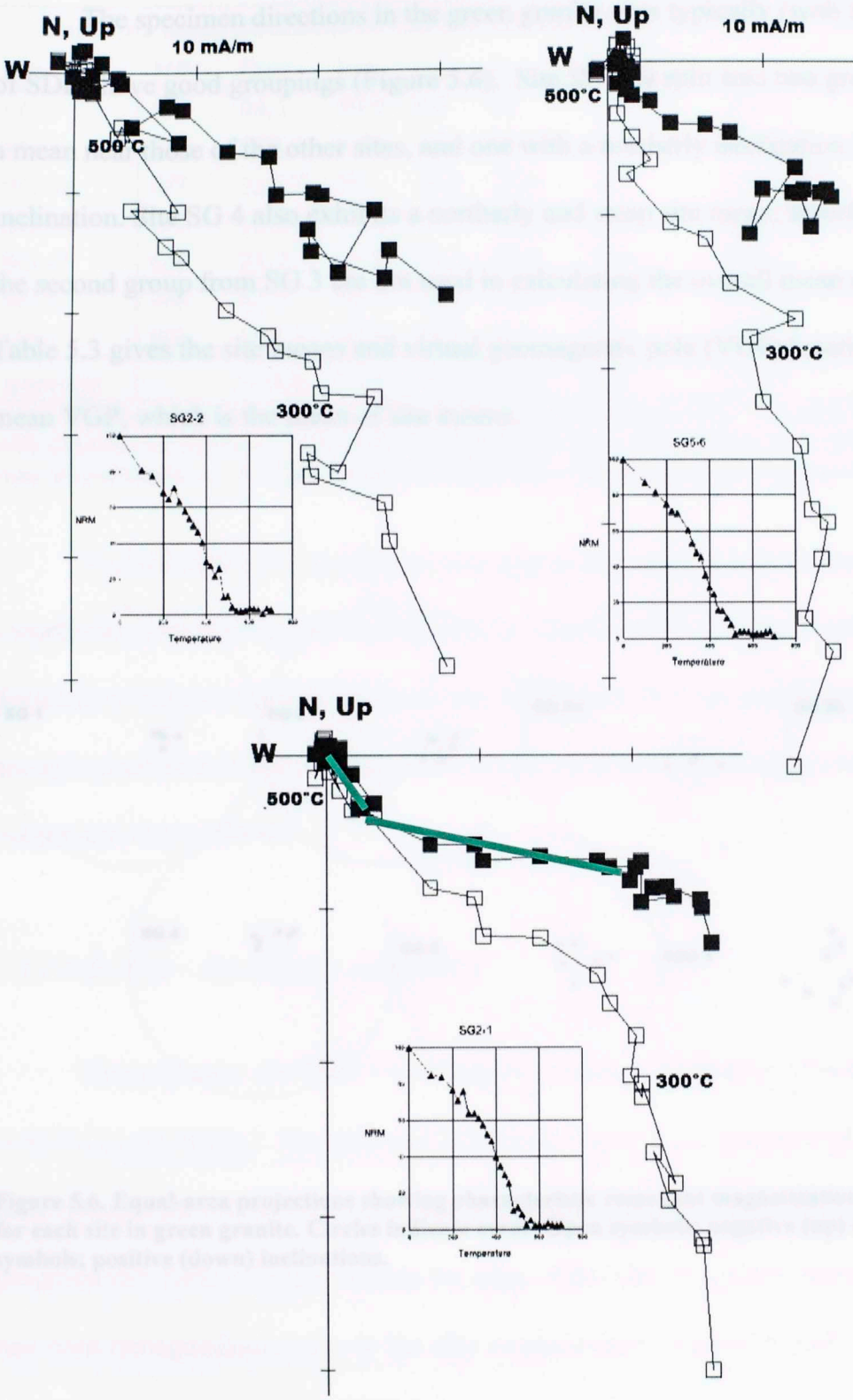

Figure 5.5. Orthogonal vector diagrams (Zijderveld, 1967) for samples SG 2-1, SG 2-2 and SG 5-6, showing the ESE and down component . Note apparent high-temperature component above 500°C in SG 2-1. Green lines overlaying SG 2-1 represent the high-temperature component and the ChRM. Open symbols; vertical component: closed symbols: horizontal component. NRM measurement has been removed from all plots, first point is after liquid nitrogen treatment.

The specimen directions in the green granite sites typically (with the exception of SDH) have good groupings (Figure 5.6). Site SG 3 is split into two groups, one with a mean near those of the other sites, and one with a northerly declination and steep inclination. Site SG 4 also exhibits a northerly and steep site mean; therefore SG 4 and the second group from SG 3 are not used in calculating the overall mean direction. Table 5.3 gives the site means and virtual geomagnetic pole (VGP) locations and the mean VGP, which is the mean of site means.

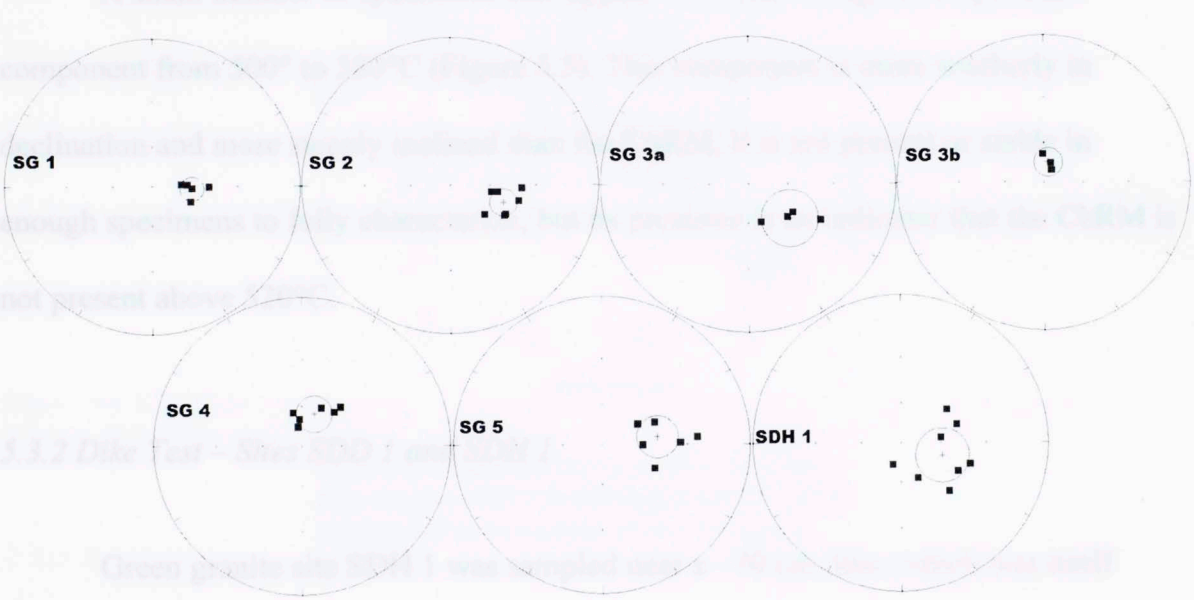

Figure 5.6. Equal-area projections showing characteristic remanent magnetizations in specimens for each site in green granite. Circles indicate error. Open symbols; negative (up) inclination: solid symbols; positive (down) inclinations.

Table 5.3 Mean directions of ChRMs and corresponding VGPs for green granite

Site	N/N_0	Dec	Inc	α_{95}	k	Latitude	Longitude	Dp	Dm
SG 1	5/7	94.1	59.9	8.6	81	19.1	314.1	9.8	13
SG 2	7/8	108.3	47.8	9.2	43.6	3.3	316.7	8	12.1
SG 3a	4/7	129.7	50	19.3	23.6	-9.2	303.1	17.2	25.8
SG 3b*	3/7	12.5	74.3	11	127.3	62.8	274.5	18	19.9
SG 4*	6/8	21.2	64.2	13.2	26.8	70.4	309.5	16.8	21.1
SG 5	7/8	82.5	48.7	14.1	19.3	22	329.4	12.2	18.6
SDH	8/9	107.2	57.4	19.1	9.4	9.1	310.7	20.4	27.9
Average	--	104.6	54.1	11.5	45.4	8.8	314.7	11.3	16.1

***Note: SG 3b and SG 4 not used in calculation of overall average. N/N_0 – Number of specimens with direction vs. number of specimens demagnetized; Dec – Declination; Inc – Inclination; α_{95} – 95% cone of confidence; k – Precision parameter; Dp, Dm – semiaxes of 95% cone of confidence of pole.**

A small number of specimens also appear to contain a higher-temperature component from 500° to 580°C (Figure 5.5). This component is more southerly in declination and more steeply inclined than the ChRM. It is not present or stable in enough specimens to fully characterize, but its presence is an indicator that the ChRM is not present above 520°C.

5.3.2 Dike Test – Sites SDD 1 and SDH 1

Green granite site SDH 1 was sampled near a ~70 cm dike, which was itself sampled as site SDD 1. The dike can be seen in Figure 4.20, sampling of SDD 1 was done towards the left of the image. The 9 specimens of site SDH 1 were taken at progressively further distances from the edge of the dike in order to determine if there had been remagnetization due to the dike emplacement. Specimen SDH 1-1 was taken 10 cm from the dike margin; SDH 1-9 was taken 140 cm (2 dike widths) from the margin.

Specimens from site SDD 1 did not yield a stable magnetization, and decay profiles show variable intensity (e.g., Figure 5.7). This is interpreted as being due to the creation of new magnetic minerals during thermal demagnetization – inspection of a specimen via microprobe indicates the presence of biotite, pyrite and ferro-sphalerite, which can break down to produce iron oxides during heating, in addition to possible oxidation of primary titanomagnetite and ilmenite.

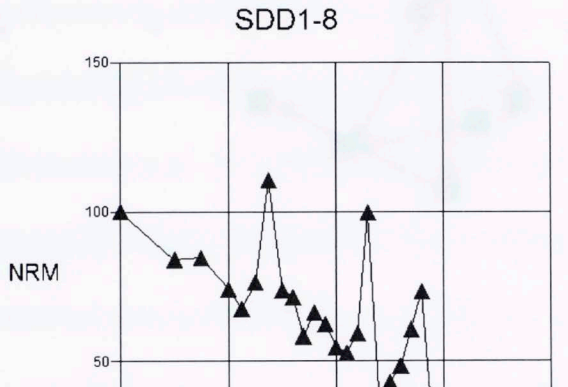

Figure 5.7. Thermal decay profile for diabase dike sample SDD 1-8 showing intensity spikes interpreted as formation of new magnetic minerals.

No substantial, consistent difference or trend in magnetization directions was found between near-dike specimens and those further away. The SDH 1 site does not group well, with a k-value of only 9.4. Figure 5.8 shows the progression of ChRM directions as specimens move away from the dike.

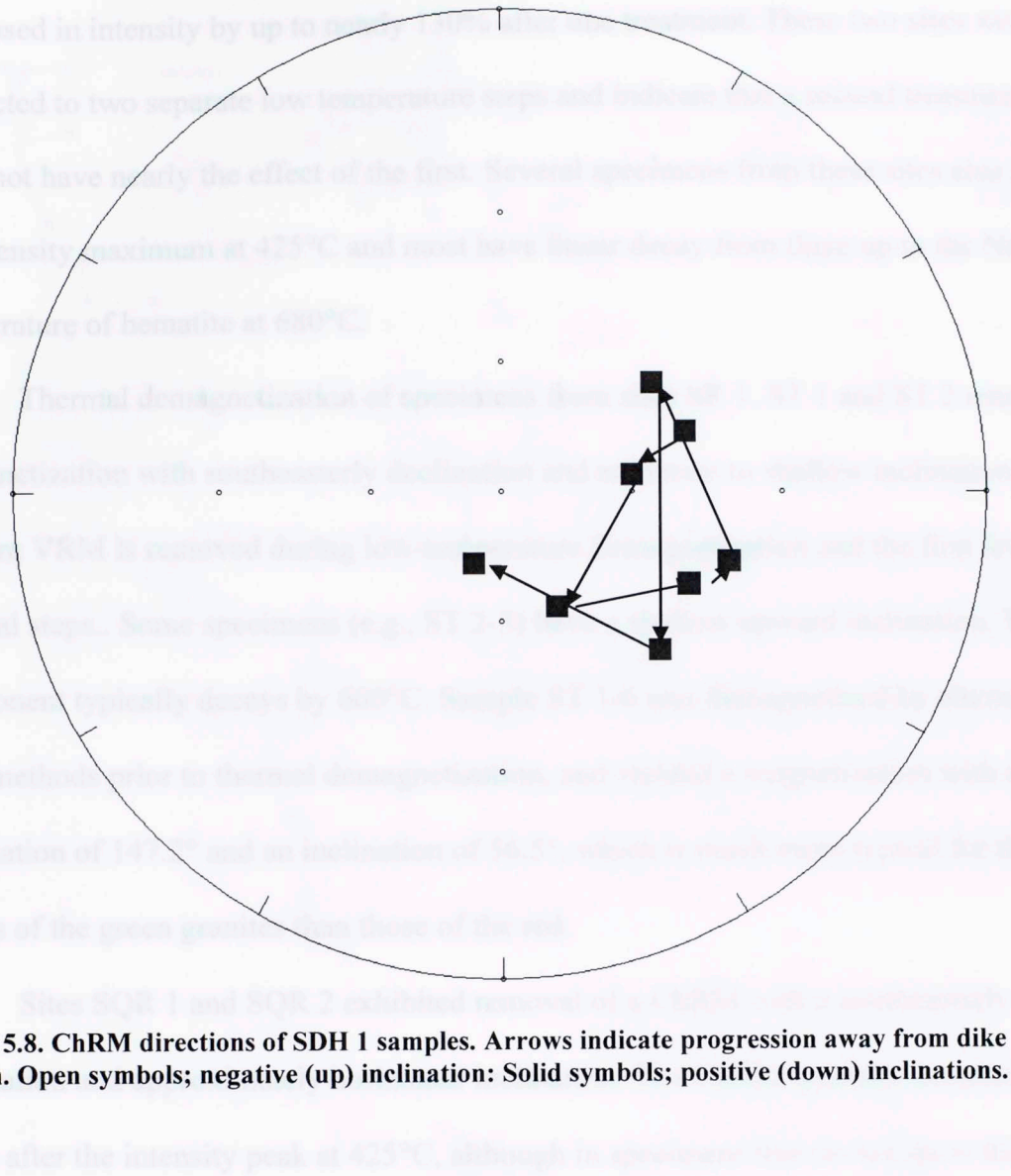

Figure 5.8. ChRM directions of SDH 1 samples. Arrows indicate progression away from dike margin. Open symbols; negative (up) inclination: Solid symbols; positive (down) inclinations.

5.3.3 Red Granite

Like those of the green granite, specimens of red granite from sites SR 1, ST 1, and ST 2 were also subjected to LTD. Specimens from sites SQR 1 and SQR 2 were subjected to two LTD steps. Results were highly variable. Some specimens from sites SR 1, ST 1 and ST 2 exhibited very little intensity drop, as low as 1.9%, after LTD. Others typically lost about 47% intensity, ranging up to as much as 95.7% intensity after a single cooling step. Some specimens from sites SQR 1 and SQR 2 actually

increased in intensity by up to nearly 130% after one treatment. These two sites were subjected to two separate low temperature steps and indicate that a second treatment does not have nearly the effect of the first. Several specimens from these sites also show an intensity maximum at 425°C and most have linear decay from there up to the Neél temperature of hematite at 680°C.

Thermal demagnetization of specimens from sites SR 1, ST 1 and ST 2 removes a magnetization with southeasterly declination and moderate to shallow inclination. Modern VRM is removed during low-temperature demagnetization and the first few thermal steps.. Some specimens (e.g., ST 2-3) have a shallow upward inclination. This component typically decays by 600°C. Sample ST 1-6 was demagnetized by alternating field methods prior to thermal demagnetization, and yielded a magnetization with a declination of 147.2° and an inclination of 56.5°, which is much more typical for the results of the green granites than those of the red.

Sites SQR 1 and SQR 2 exhibited removal of a ChRM with a southeasterly declination and approximately horizontal inclination. The ChRM typically becomes stable after the intensity peak at 425°C, although in specimens that do not show this peak it is stable at lower temperatures. The component is not fully removed until 700°C. Orthogonal vector diagrams (Zijderveld, 1967) for representative specimens from sites in red granite are shown in Figure 5.9.

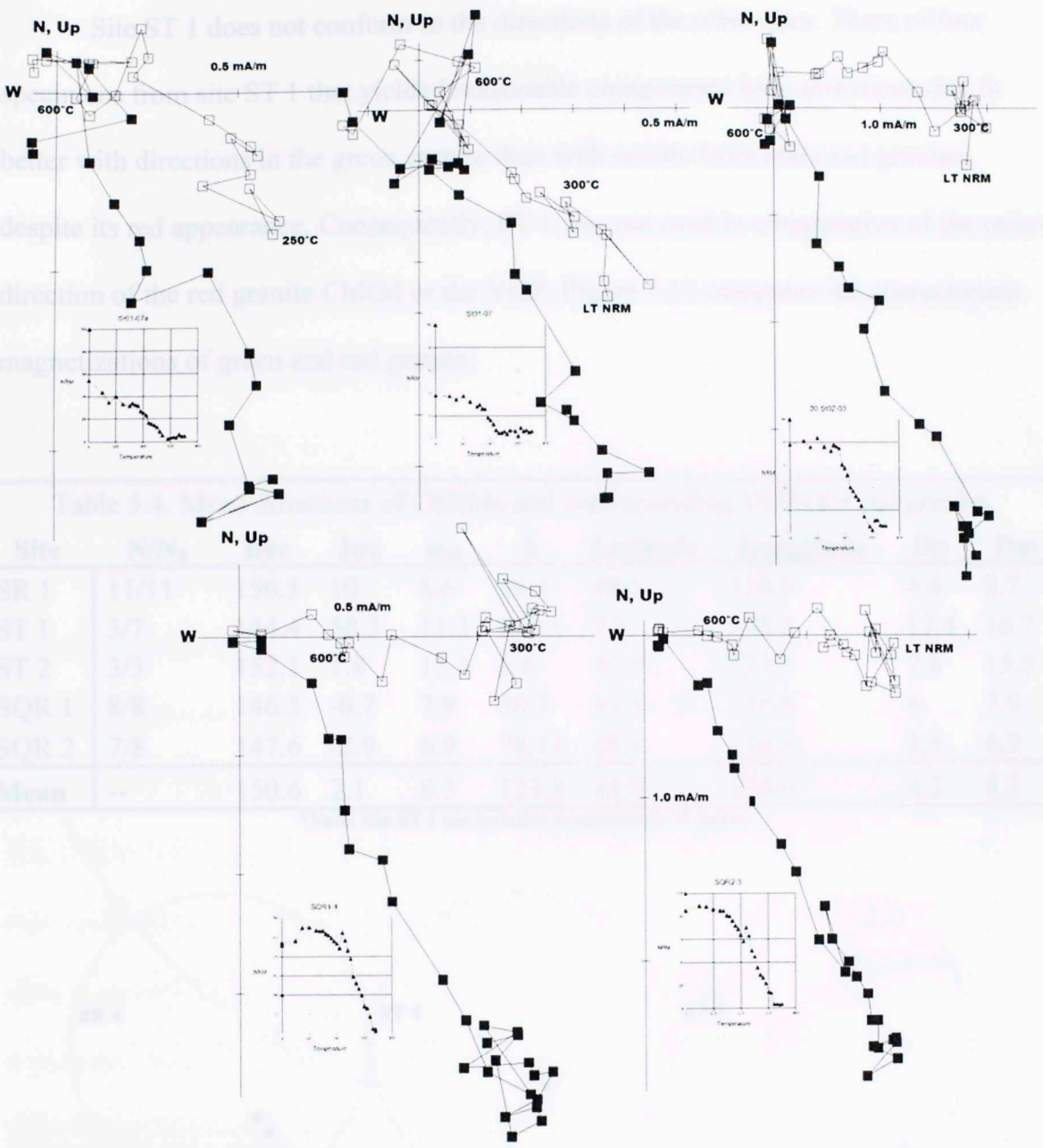

Figure 5.9. Orthogonal vector diagrams for representative specimens from sites in red granite. Open symbols: vertical component; closed symbols: horizontal component. NRM measurement has been removed from all plots.

Sites in red granite are mostly consistent with each other. The two sites that make up SR 1 group together well, the only real difference being that one site has down inclinations and the other up. The three specimens of site ST 2 group together well, as do specimens for sites SQR 1 and SQR 2. Figure 5.10 shows equal area projections of ChRM components from each site. Site means and VGPs are given in Table 5.4.

Site ST 1 does not conform to the directions of the other sites. Three of four specimens from site ST 1 that yielded reasonable components have directions that fit better with directions in the green granite than with results from other red granites, despite its red appearance. Consequently, ST 1 was not used in computation of the mean direction of the red granite ChRM or the VGP. Figure 5.11 compares the characteristic magnetizations of green and red granite.

Table 5.4. Mean directions of ChRMs and corresponding VGPs for red granite.

Site	N/N_0	Dec	Inc	α_{95}	k	Latitude	Longitude	Dp	Dm
SR 1	11/11	156.5	10	8.6	26.4	44.5	114.9	4.4	8.7
ST 1	3/7	144.4	58.3	11.3	120.1	9.3	108.3	12.4	16.7
ST 2	3/3	152.1	1.8	15.5	6.6	45.9	123.3	7.8	15.5
SQR 1	8/8	146.3	-0.7	7.9	50.7	43.5	130.9	4	7.9
SQR 2	7/8	147.6	-2.9	6.9	78.11	45.1	130.4	3.5	6.9
Mean	--	150.6	2.1	8.3	123.8	44.9	124.9	4.2	8.3

***Note: Site ST 1 not included in calculation of means.**

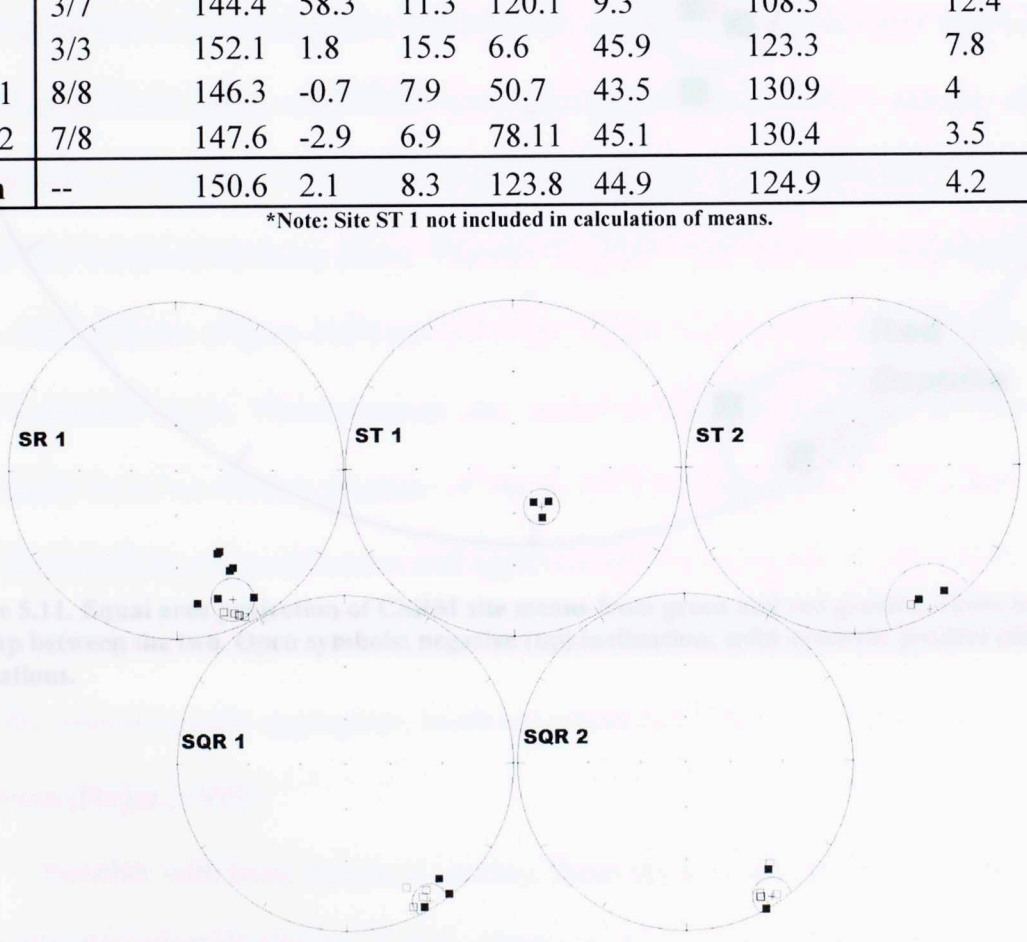

Figure 5.10. Equal area projections showing ChRMs determined via principal component analysis for sites in red granite. Red circles indicate error. Open symbols: negative (up) inclination; solid symbols: positive (down) inclinations.

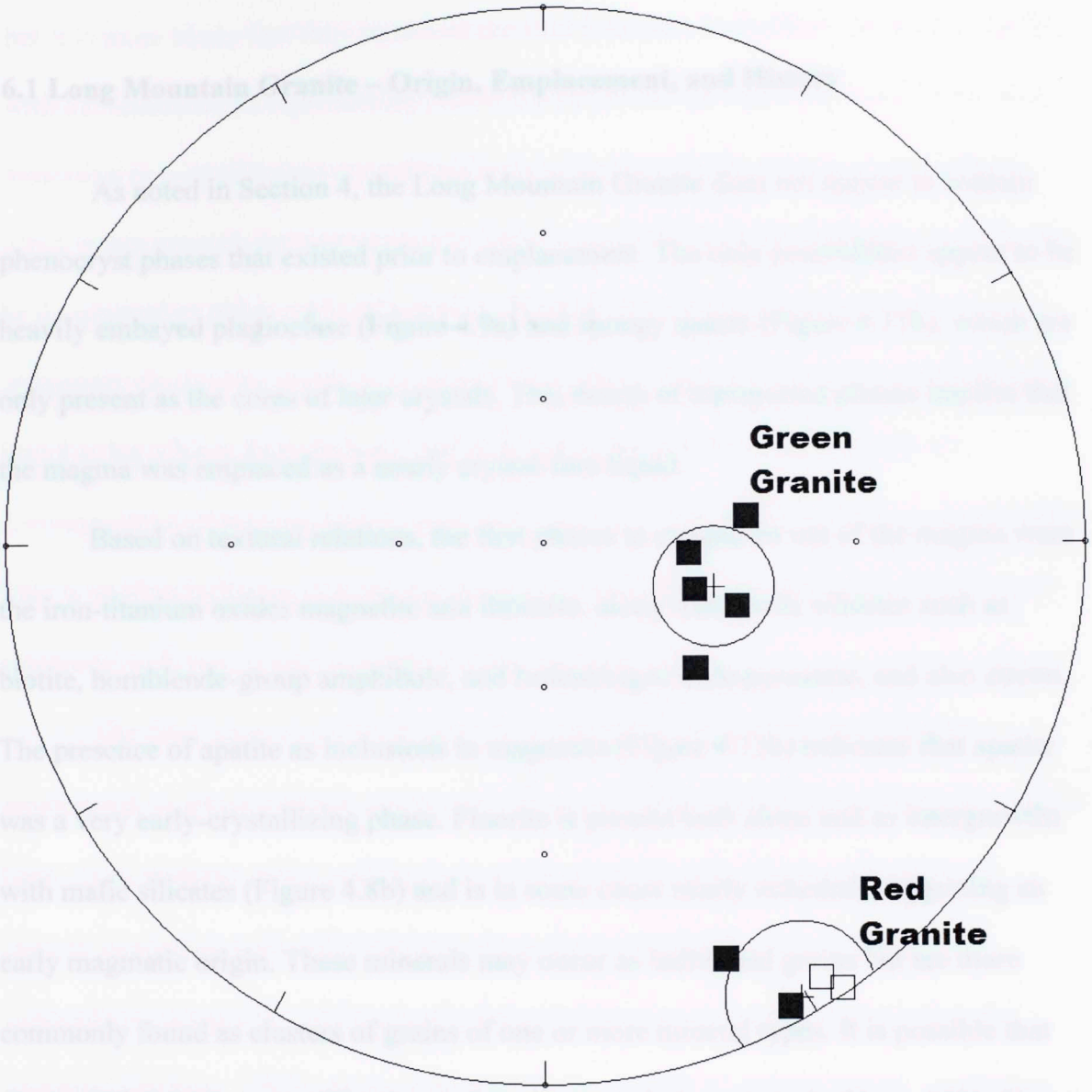

Figure 5.11. Equal area projection of ChRM site means from green and red granite. There is no overlap between the two. Open symbols: negative (up) inclination; solid symbols: positive (down) inclinations.

6. Discussion

6.1 Long Mountain Granite – Origin, Emplacement, and History

As noted in Section 4, the Long Mountain Granite does not appear to contain phenocryst phases that existed prior to emplacement. The only possibilities appear to be heavily embayed plagioclase (Figure 4.9a) and spongy quartz (Figure 4.11b), which are only present as the cores of later crystals. This dearth of transported phases implies that the magma was emplaced as a nearly crystal-free liquid.

Based on textural relations, the first phases to crystallize out of the magma were the iron-titanium oxides magnetite and ilmenite, along with mafic silicates such as biotite, hornblende-group amphibole, and hedenbergite clinopyroxene, and also zircon. The presence of apatite as inclusions in magnetite (Figure 4.12b) indicates that apatite was a very early-crystallizing phase. Fluorite is present both alone and as intergrowths with mafic silicates (Figure 4.8b) and is in some cases nearly euhedral, suggesting an early magmatic origin. These minerals may occur as individual grains but are more commonly found as clusters of grains of one or more mineral types. It is possible that they collided during crystallization and agglomerated via synneusis (Vogt, 1921; Vance, 1969). Other possibilities include crystallization due to local saturation (Bacon, 1989) and, for monomineralic aggregates, localized resorption followed by saturation and regrowth (Hogan, 1993).

Possibly with some temporal overlap, these phases were followed by the crystallization of alkali feldspar grains, which are also seen to commonly occur as clusters. Some of these contain the heavily embayed plagioclase cores mentioned above,

with compositions as calcic as An_{21}. These cores may be pre-emplacement phenocrysts, but it is more likely that they represent the first feldspars crystallized from the magma, with the embayments representing partial resorption as the liquid was depleted in Ca, indicating non-equilibrium crystallization (see London, 2008, Figure 17-13). These cores, when present, are surrounded by highly exsolved alkali feldspars ($An_{<2}$) that may be dominated by either sodic or potassic feldspar. The alkali feldspar grains are commonly rimmed by much more potassic feldspar. The plagioclase-rimmed feldspars found in the Mount Scott Granite, which were interpreted as resulting from the decompression of magma during ascent (Price et al., 1996; Price, 1998), are not present. This is another indicator that the magma that became the Long Mountain Granite was emplaced with few, if any, crystals initially present.

The final stage of crystallization was that of the ubiquitous granophyric intergrowth of alkali feldspar and quartz. The granophyric intergrowths typically radiate from alkali feldspar grains and begin as a rim of nearly pure quartz, with feldspar content increasing with radial distance from the nucleation surface (Figure 6.1). Granophyric texture is a hallmark of substantial undercooling of magma below its liquidus (Dunham, 1965) and is considered to be a result of compositional oscillation about the alkali feldspar-quartz cotectic (Fenn, 1986; London et al., 1989; London, 2008).

Dunham (1965) also noted a common relationship of granophyres with extrusive rocks. Lowenstern et al. (1997) investigated an occurrence of co-magmatic granophyre and rhyolite and concluded that the granophyre was the result of undercooling due to loss of volatiles via volcanism. Their study indicated that the

granite pluton was emplaced under conditions similar to the emplacement of the Wichita Granites, with the exception of a final explosive eruption, for which there is no evidence preserved in the Wichitas. This comparison does suggest, however, that some of the Wichita Granite Group, especially the ubiquitously granophyric Long Mountain Granite, may represent exposed magma chambers of Cambrian volcanoes. This argument is consistent with the accepted interpretation of the Saddle Mountain Granite as being a derivative of the Mount Scott Granite that broke through the overlying Carlton Rhyolite and extruded onto the surface (Myers et al., 1981).

Counter to this argument is the fact that sudden dehydration of a granitic magma should lead to immediate crystallization of feldspar (London, 2008, Fig. 13-5). Loss of volatiles displaces the liquidus surface towards more quartz-rich compositions, causing feldspar to crystallize out. This is exactly the opposite of what is seen in the Long Mountain Granite granophyres, where quartz is the first phase to nucleate.

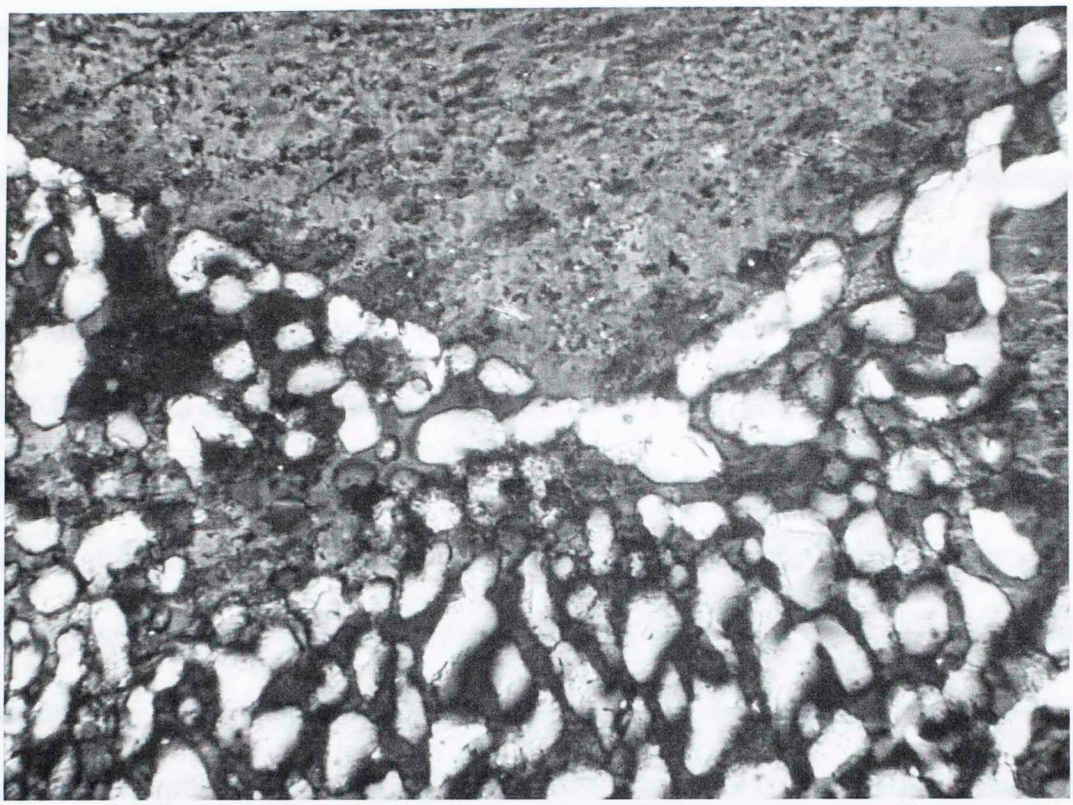

Figure 6.1. Granophyric nucleation from an alkali feldspar grain surface. The near edge is virtually 100% quartz. Cross-polarized light, 0.44 mm field of view.

Titanite is absent in all samples examined in the current study, though it was previously reported (Hessa, 1964) in other locations. Price et al. (1999) determined experimentally that magma prepared from Mount Scott Granite would precipitate fluorite, but not titanite, at fluorine contents above 1 wt. %. If this was the case for the Long Mountain Granite, substantial amounts of fluorine have since been lost, as the chemical analyses presented in Table 4.1 show a maximum of 0.24 wt. % F. Price (1998) believed that the Mount Scott Granite does not preserve the original F content of the magma, and this appears to likewise be the case for the Long Mountain Granite.

The unidentified brown mineral phase (Figure 4.12a) is taken to be an alteration product of primary biotite, as it contains rounded grains of biotite and has a habit similar to that of rare intact biotite. The rock also contains a hornblende-group

amphibole, which is not commonly found adjacent to biotite. It is possible that biotite and amphibole crystallized at different times, depending on the activities of fluorine and water in the magma. Quantitative analysis of two amphibole grains yields an average of 1.073 aluminum atoms per 23 atoms of oxygen. Using the geobarometer of Johnson and Rutherford (1989), this suggests that hornblende crystallized at a pressure of 80 to 145 (±50) MPa, which corresponds to a depth range of 2.5 to 4.5 km. Only the highest end of this pressure range corresponds with the lowest end of the range reported for the Mount Scott Granite (Hogan and Gilbert, 1995), which was interpreted to represent partial crystallization at 7-8 km depth for that body. The lowest pressure estimate, when the uncertainty of the geobarometer is incorporated, is only 30 MPa, which would be an emplacement depth of approximately 1 km. All estimates of crystallization pressure for the amphibole are lower than the range the Johnson and Rutherford geobarometer was calibrated over, and therefore may not be reliable. The fact that they are consistently lower, however, suggests that the amphibole formed *in situ* and was not partially crystallized at depth, as was that of the Mount Scott (Hogan and Gilbert, 1995). This, along with the textural features mentioned previously, strengthens the argument that the Long Mountain magma was virtually crystal-free when emplaced.

Genesis of crystal-poor rhyolite magmas is thought to require separation from a crystalline mush in large granitic plutons in the middle and upper crust (Bachmann and Bergantz, 2004), which have not been exposed in the Wichita Mountains, but which have been invoked in geophysical modeling (Keller and Stephenson, 2007, see Figure 2.2 of this thesis). This is consistent with the geochemical data, which suggests that the Long Mountain Granite was derived by evolution of something with similar

composition to the Mount Scott Granite. The Mount Scott is thought to represent liquid emplaced from a deeper magma reservoir (Hogan and Gilbert, 1995), and it is possible that further crystallization of this reservoir would result in expulsion of a largely crystal-free liquid via the mechanism of Bachmann and Bergantz (2004).

The absence of apatite outside of inclusions in magnetite or cores of monazite may be another indicator of alteration in the green facies of Long Mountain Granite. Apatite has been shown experimentally to be replaced by monazite under hydrothermal conditions at temperatures above 300°C (e.g., Harlov et al., 2005) for certain fluid compositions. The textural relations of apatite to monazite (Section 4.3.1 of this thesis) are therefore taken as possible evidence that monazite is not a primary magmatic mineral at Long Mountain, and therefore is possibly unsuitable for geochronological analysis, although it may yield a date for hydrothermal alteration if the age of monazite is demonstrably different from that of zircon. Conversely, apatite has been shown to be replaced by monazite under magmatic conditions in peraluminous granite liquids when phosphorous content is diminished (Wolf and London, 1995), in which case it may be a primary mineral. Epidote is considered to be a secondary mineral.

The feldspars of Long Mountain also show evidence of alteration. Coarsened and patchy exsolution features have long been interpreted to result from recrystallization of perthite and antiperthite under deuteric and hydrothermal conditions (Parsons, 1978; Worden et al., 1990; Parsons and Lee, 2009). These features are evident in the feldspars of Long Mountain Granite (Figure 4.10). In conjunction with the aforementioned mineralogical relationships, this is a strong indicator that the Long Mountain Granite underwent significant hydrothermal modification following its

emplacement and crystallization, and these assumedly deuteric interactions did not result in the red coloration seen in outcrop.

It is also prudent to note that patchy and coarse alkali feldspar intergrowths have been generated as primary features of crystallization during experiments (e.g., Petersen and Lofgren, 1986; London et al., 1989). These experiments were under strongly undercooled conditions, which is the model promoted by London (2008) for the formation of quartz-first granophyre. This provides an alternate possible origin for the patchy feldspars in green granite, though it does not rule out deuteric recrystallization.

6.2. Origin of Red Granite

6.2.1 Historical Studies of Clouded Feldspars and Red Coloration in Granites

Natural feldspar minerals have been shown to sometimes incorporate up to a few weight percent iron substituting for aluminum in their structures (e.g., Coombs, 1954). Iron-bearing feldspars have also been synthesized in experiments (e.g., Rosenqvist, 1951; Wones and Appleman, 1961; Lindqvist, 1966). Rosenqvist (1951) and Lindqvist (1966) interpreted their experiments as showing that iron-rich feldspars ($KFeSi_3O_8$) could crystallize under magmatic conditions in aluminum-poor environments and subsequently undergo subsolidus exsolution into potassium feldspar plus hematite. This interpretation was used to explain hematite lamellae in aventurine plagioclase (Neumann and Christie, 1962) as well as red coloration in other plagioclase minerals (e.g., Isshiki, 1958; Ernst, 1960). Zhang and Halls (1995) found magnetite in clouded plagioclases and concluded from paleomagnetic analysis that the magnetite was exsolved during cooling of primary iron-bearing feldspar.

Boone (1969) performed a thorough petrologic examination of a Canadian granite porphyry in order to understand the conditions of hematite formation. He found that plagioclase in red-colored rocks had been recrystallized to albite and muscovite and lost its compositional zoning. He also observed that biotite and hornblende had been largely replaced by chlorite, and concluded that the iron lost by these minerals had been deposited as hematite in micropores in feldspar during post-magmatic reactions. This interpretation was bolstered by the work of Wenner and Taylor (1976; Taylor, 1977), who found that red granite in the St. Francois Mountains of Missouri was enriched in

^{18}O relative to non-reddened granites of the same suite. They concluded that this was due to the interaction of low-temperature waters, which are isotopically heavier. Based on anomalously young K-Ar and Rb-Sr dates, Wenner and Taylor (1976) concluded that the alteration event likely occurred 200-300 million years after the emplacement of the granites.

Parsons (1978) suggested that coarsening of perthite exsolution features is an indicator of recrystallization of feldspars under hydrothermal conditions. This was further investigated by Worden et al. (1990), who showed that this coarsening was associated with the development of micrometer-sized porosity. Nakano et al. (2005) inspected these micropores and found that the majority of them contained mineral inclusions. Putnis et al. (2007) showed that most of these mineral inclusions were actually hematite precipitated during feldspar replacement reactions. These reactions are generally thought to occur at conditions between 250° and 400°C based on feldspar structural constraints (Worden et al., 1990; Waldron and Parsons, 1992; Parsons and Lee, 2009) and associated mineralogy (Ferry, 1985; Drake et al., 2008; Sandström et al., 2010). The fluids involved have been postulated to be deuteric waters cooling from magmatic temperatures (Parsons and Becker, 1986; Putnis et al., 2007).

Reddened granites have been observed to be often associated with fractures (e.g., Drake et al., 2008; Plümper and Putnis, 2009; Sandström et al., 2010). They exhibit reduced magnetic susceptibility and density (Eliasson, 1993; Mattsson and Thunehed, 2004) and their iron content is typically more oxidized and their porosity increased (Eliasson, 1993). Drake et al. (2008) observed that, in their samples, plagioclase feldspars were replaced by either micas or k-feldspar. They also reported partial

replacement of magnetite by hematite and replacement of biotite by an assemblage of titanite, chlorite, fluorite, k-feldspar, quartz, muscovite and prehnite. Plümper and Putnis (2009) also found evidence of feldspar replacement reactions and hematite precipitation near fractures. Sandström et al., (2010) showed that there can be significant redistribution of major and trace elements among mineral phases, while the whole-rock chemistry exhibits only limited change during the alteration.

6.2.2 Long Mountain

As shown in Tables 4.1 and 4.2, the red facies of Long Mountain Granite may be slightly enriched in volatiles and Fe_2O_3 relative to green granite, and in turn relatively depleted in K_2O, SiO_2, MnO, and FeO. With the exception of the different valences of iron, however, these differences are relatively minor (always less than 1 wt.%) and with increased numbers of samples may even prove statistically insignificant. On the whole, the alteration from green to red granite at Long Mountain was nearly isochemical, which is consistent with the results of Sandström et al. (2010), though some of the details are different (e.g., reduction in K rather than Na).

Red Long Mountain Granite shows extensive destruction of mafic silicate grains as well as hematization of primary titanomagnetite and ilmenite. This, coupled with the fact that total iron content is the same as that of green granite, indicates that the iron for the hematite was sourced from the granite itself and was not externally derived. As in the studies mentioned in the previous section, red granite at Long Mountain appears to spatially correlate with fractures and density. In the upper and outer parts of the granite body, the rock is thoroughly red well away from open fractures, but there is evidence of

previous fractures that have been cemented by silica; there are also silica-filled voids such as the one in Figure 4.14b.

Feldspars in red granite commonly show evidence of alteration above and beyond that exhibited in green granite (Figure 4.15). In some cases, they have developed much patchier exsolution textures (Figure 6.2); in others they become strongly turbid in addition to reddening (Figure 6.3). Hematite can also be seen permeating the feldspars along exsolution lamellae in granophyric feldspars (Figures 4.20, 6.4).

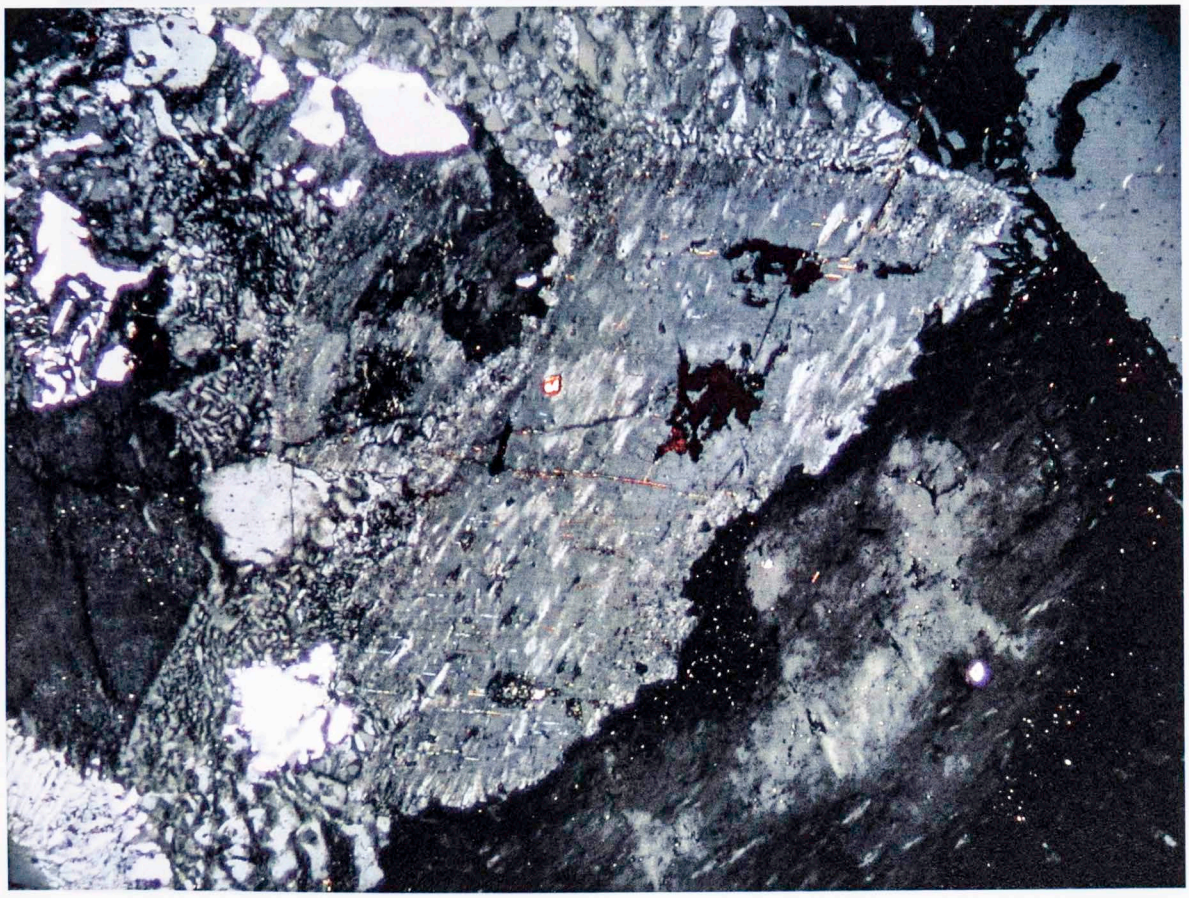

Figure 6.2. Coarsened, patchy exsolution in feldspar of red Long Mountain Granite. Cross-polarized light, 3.5mm field of view.

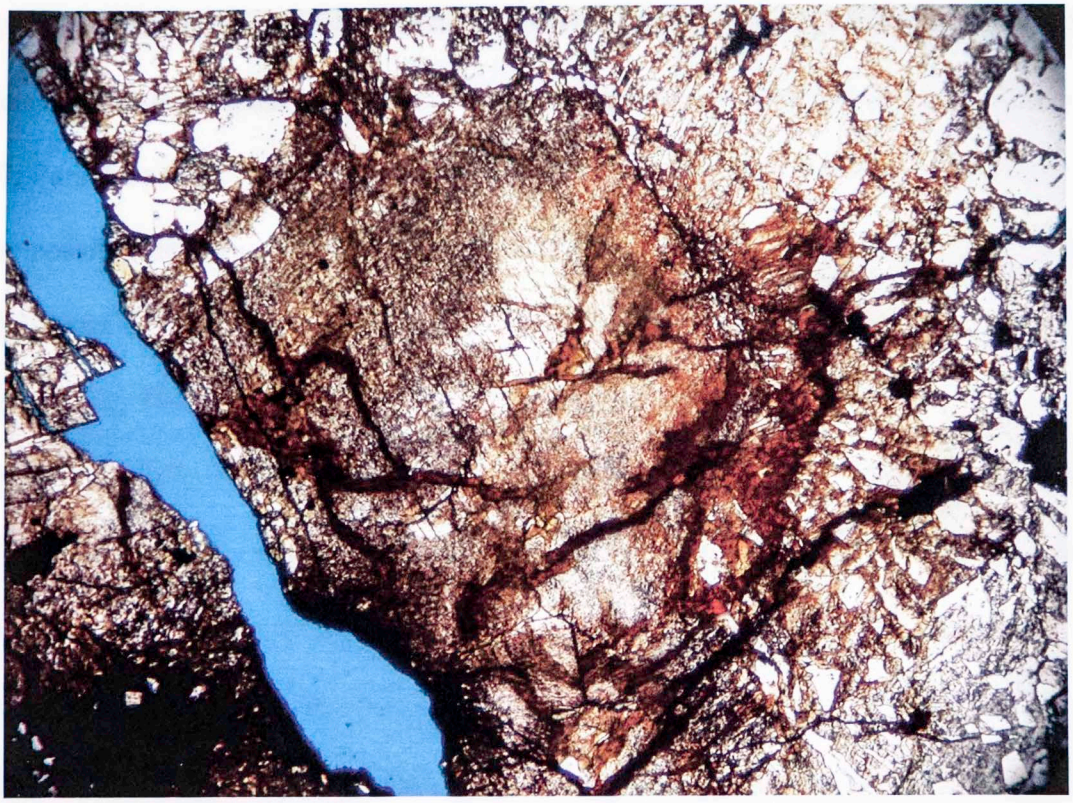

Figure 6.3. Turbid red-stained feldspar. Plane-polarized light, 3.5m field of view.

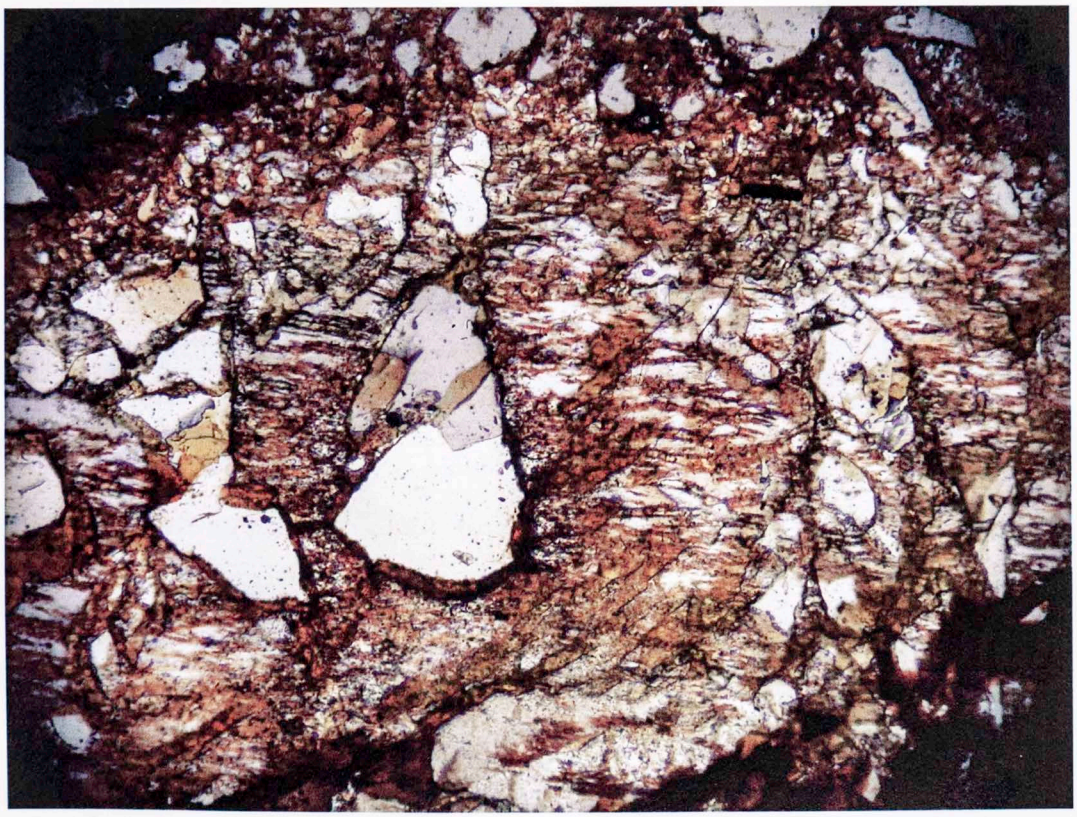

Figure 6.4. Hematite staining permeating along exsolution lamellae. Plane-polarized light, 1.75mm field of view.

The coarsened, patchy exsolution features, turbidity and permeation of hematite indicate that at least some of the feldspars in red granite have recrystallized (Putnis et al., 2007; Parsons and Lee, 2009; Plümper and Putnis, 2009), and have done so subsequent to the possibly deuteric coarsening noted in Section 6.1. Figure 4.20 shows that iron in the feldspars of red granite is much more abundant than in those of green granite (Figure 4.19). There is also a positive correlation with sodium abundance, which suggests that albite was more susceptible to recrystallization than the potassic feldspars.

Void spaces in red granite left by destruction of mafic grains are variably filled with calcite and epidote-group minerals. While epidote is present as a secondary accessory mineral in green granite, it appears to be more abundant in red granite and occurs as larger grains. Epidote has also been found coating fractures in red granite (Figure 4.3), though it has not been observed to do so in green granite. Epidote is typically formed at temperatures of 320°C or above (Deer et al., 1992). While it has been found in natural hydrothermal systems at lower temperatures, many of these occurrences are believed to be relics of prior high-temperature alteration events (Bird and Spieler, 2004). Its occurrences in red granite above and beyond those in green granite suggest that the alteration process that resulted in red coloration occurred at temperatures in excess of 300°C. This estimate overlaps with other temperature estimates for development of feldspar turbidity (Ferry, 1985; Worden et al., 1990; Waldron and Parsons, 1992; Drake et al., 2008; Parsons and Lee, 2009; Sandström et al., 2010).

Oxygen isotope studies may be of use in further constraining the temperature of alteration; however, the rocks may have undergone later isotopic equilibration with low-

temperature groundwaters, which could mask the isotopic signal of high-temperature fluid interactions (Wenner and Taylor, 1976; Taylor, 1977; Donoghue et al., 2010). Alternatively, if epidote fracture coatings are found in green granite, it would suggest that the alteration could have occurred at lower temperatures, as postulated by Wenner and Taylor (1976).

6.3. Paleomagnetism of Green Granite

6.3.1 Origin of Remanent Magnetization

The green facies of Long Mountain Granite contains a ChRM which is thermally removed over the temperature interval between 275°C and 520°C. The ChRM in green granite appears to be wholly contained within magnetite as evidenced by observation of primary magnetite by petrography and concurrent absence of hematite with the exception of a few fracture faces, large drops in magnetic intensity after liquid nitrogen treatment (Dunlop et al., 1997; Borradaile et al., 2004), nearly complete thermal decay by 520°C, and nearly complete decay under alternating field (AF) demagnetization by 120 mT of applied field.

The ChRM of the green granite is interpreted as either a thermal (TRM) or thermoviscous (TVRM) remanent magnetization based on time-temperature relaxation curves from Pulliah et al. (1975). The maximum unblocking temperature of the ChRM is in the range of 500-520°C. Finite element analysis using the KWare Heat3D software by Ken Wohletz (2008) shows that the center of a granitic magma body with a temperature of 950°C and a thickness of 500m intruded into granite at a depth of 1km and a geothermal gradient of 30°C/km will take approximately 10^4 years to cool to a

maximum core temperature of around 580°C. It can then be expected to remain at elevated temperatures above 350°C for a period of over 10^5 years. This estimated thermal history of the Long Mountain Granite agrees with an interpretation of the ChRM as a TRM or TVRM based on the curves given by Pulliah et al. (1975) as shown in Figure 6.5.

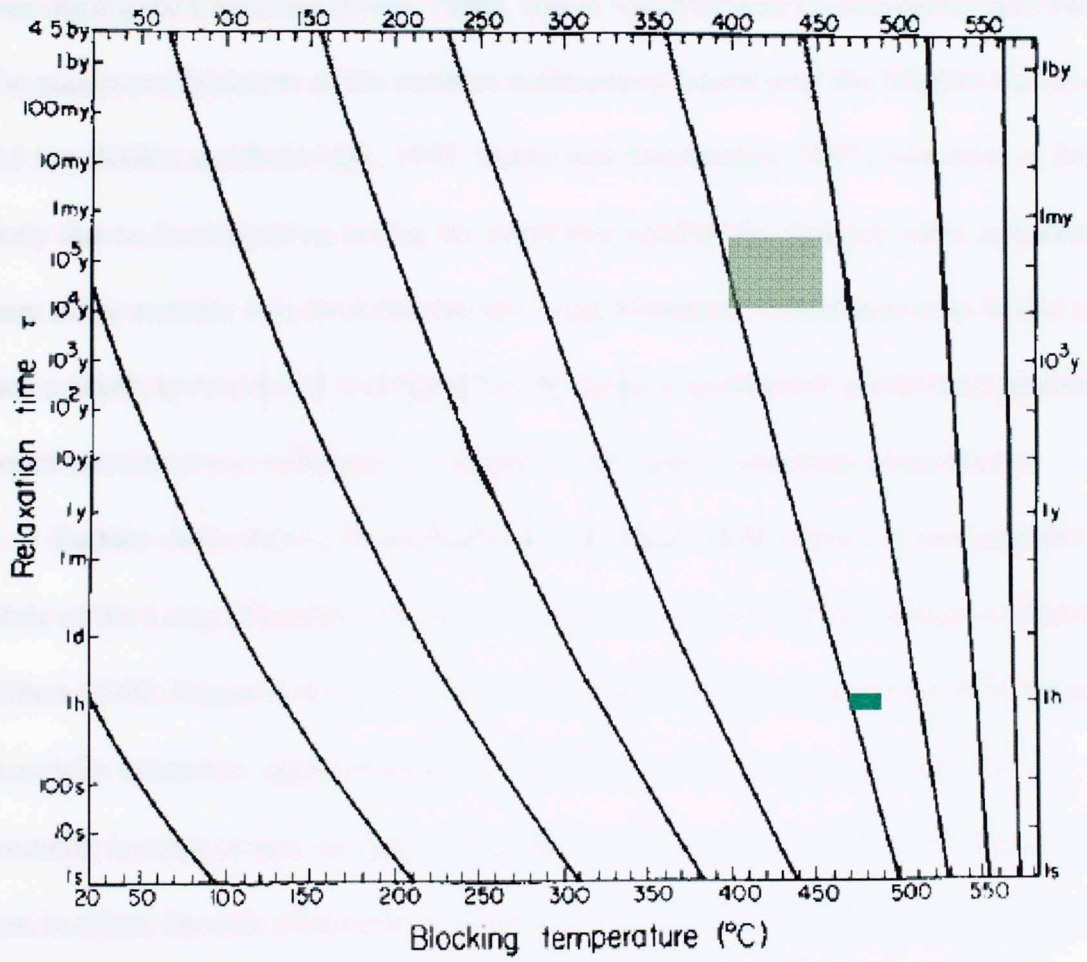

Figure 6.5. Time-temperature relaxation curves for magnetite, modified from Pulliah et al. (1975). Laboratory heating time and unblocking temperature of green granite ChRM shown in bright green, plausible geological thermal history indicated by dull green rectangle.

A TRM or a TVRM in the green granite is likely to be a primary magnetization. There is no reason to believe that the granite should have ever been exposed to elevated

temperatures following its emplacement. Hogan et al. (2000) argue that the volcanic pile into and beneath which the Wichita Granite Group was emplaced is unlikely to have ever exceeded a thickness of approximately 4 km; the maximum preserved thickness of the Carlton Rhyolite Group is only about 1.4km (Ham et al., 1964). There was considerable uplift and erosion of Carlton group rhyolites and Wichita granites even during the Cambrian (Price, 1998), which was followed by subsidence and burial. The maximum thickness of the modern sedimentary basins near the Wichita Uplift is ~15 km (Keller and Baldridge, 1995; Keller and Stephenson, 2007), but some of this is likely due to downwarping during the event that uplifted the igneous rocks and returned them to the surface; it is doubtful that the Long Mountain Granite was ever buried at such a depth, and burial at that depth with a standard continental geothermal gradient would not have been sufficient to account for the high unblocking temperatures.

Further evidence for the existence of a primary magnetization is the magnetic fabric of the Long Mountain Granite. As previously mentioned, according to Hogan and Gilbert (1997; Hogan et al., 2000), the Wichita Granite Group was essentially intruded as aerially extensive, approximately horizontal sills of thickness ≤ 0.5 km. This geometry is more or less the same as smaller dikes. Previous AMS studies have shown that, in dikes, the axis of minimum susceptibility (K_3) is typically perpendicular to the plane of the dike (e.g., Rochette et al., 1991, 1992; Herrero-Bervera et al., 2001). Likewise, the P-Km relations for the Long Mountain Granite (Figure 5.1) are similar to those found by Rochette et al. (1991) in dikes (see Rochette et al., 1992, Figure 6d).

Ferré et a. (1999) performed an AMS study on the A-type Bushveld granites of South Africa. Their summary of the geologic setting of the Bushveld complex suggests

a great deal of similarity to the Wichita Igneous Province, though the Bushveld province is much older and much larger, with thicker granite bodies. In those granites, they identified magnetic foliations that were dominantly indicative of an approximately horizontal planar fabric. "Abnormal" fabrics were attributed to development of mineralogical layering and higher abundances of paramagnetic minerals. They concluded that in "magnetite-rich" granites, the AMS fabric was largely controlled by magma flow orientation of magnetite, and that the granites had been emplaced with very low ratios of solid to liquid.

Though high-field measurements would be needed to quantitatively evaluate the contributions of paramagnetic minerals to the AMS fabric of the Long Mountain Granite, to a first approximation they appear to be negligible. Biotite and amphibole are the main paramagnetic influences on granite AMS, along with other less common accessory minerals such as tourmaline (Rochette et al., 1992). Tourmaline is absent in the Long Mountain Granite, and as mentioned in Section 4, amphibole and unaltered biotite are quite scarce. When they are present, they do not appear to have a preferred orientation. Based on these observations, the absence of a petrographic strain fabric, and the similarity of the AMS fabric of Long Mountain to the dominant fabric found in the Bushveld granites by Ferré et al. (1999), it seems likely that the AMS fabric of the green facies of the Long Mountain Granite is a primary fabric controlled by magma flow orientation of magnetite grains. If this is the case, it implies that magnetite-bearing glomerocrysts may predate intrusion, as they would not have been aligned by flow if they had crystallized post-intrusion.

The AMS fabric in the Bushveld granites was interpreted as representing laccolith-style emplacement of the granites by roof uplift (Ferré et al., 1999). The Eastern Mourne pluton in Ireland yields similar fabrics and was likewise interpreted to represent laccolith-style roof uplift emplacement (Stevenson et al., 2007). The similar fabric of the Long Mountain Granite to these granite bodies suggests a similar emplacement style, which is consistent with previous interpretations of the emplacement style of the nearby Mount Scott Granite (Hogan and Gilbert, 1995, 1997; Hogan et al., 2000), further strengthening the argument for a primary AMS fabric. The presence of a primary magnetic fabric in the green facies of the Long Mountain Granite is considered as further evidence that the rock carries a primary paleomagnetic remanence. It is also worth noting here that the sites that yielded aberrant paleomagnetic directions (SG 4 and part of SG 3) also exhibit the greatest deviation from a vertical K_3 axis (Figure 5.1).

One argument against a primary remanence is the failed contact test (Section 5.3.2). The heating due to intrusion of a mafic dike should have been sufficient to reset the magnetization near the dike margin, but this does not appear to have occurred. At the same time, there is no petrographic evidence for alteration that could have reset the magnetization after the emplacement of the dike. Given that most models of the evolution of the Southern Oklahoma Aulacogen suggest a short duration of felsic magmatism overlapping with and followed by diabase, it is tentatively postulated here that there may simply have not been sufficient time between the granite emplacement and the dike intrusion to allow sufficient apparent polar wander to create a measurable change in magnetic direction.

6.3.2 Green Granite VGP – Location and Implications

The virtual geomagnetic pole (VGP) calculated for the green facies of Long Mountain Granite lies at the location 8.8°N, 314.7° E. Figure 6.6 shows the reverse of this pole plotted relative to the North American Apparent Polar Wander Path (APWP) of Van der Voo (1993). The pole does not overlap with the APWP, and lies well away from the projected path for the middle to late Cambrian, the supposed age of the granite.

While the VGP for the green granite does not appear to be consistent with the APWP of Van der Voo (1993), it is consistent with other paleomagnetic poles from rocks of approximately the same age. Spall (1968) obtained a paleopole from the Wichita Granite Group at coordinates 2°N, 147°E that he believed to be of Cambrian age. Elmore et al. (1998) reported a possible primary pole from the Colbert Rhyolite (presumably an extension of the Carlton Rhyolite Group) in the Arbuckle Mountains of southern Oklahoma. This pole was found to lie at coordinates 11° S, 151°E. Barr and Kirschvink (1983) obtained a pole with position 20°S, 137°E in volcanoclastic deposits from Mexico with a reported age of ~524 Ma (Kirschvink et al., 1997). Kirschvink et al. (2006) re-investigated the same unit and derived a pole position of 21°S, 142°E. Figure 6.6 shows these additional poles plotted alongside that calculated for the green Long Mountain Granite in this study.

These five paleomagnetic poles group well, as shown in Figure 6.6. While Dp and Dm values for the Barr and Kirschvink (1983) and Kirschvink et al. (2006) poles are not available, it appears likely that they would at least partially overlap the area overlapped by the poles of Spall (1968), Elmore et al. (1998) and that of the present study. This

clustering is evidence for the existence of a primary Cambrian VGP for North America in this direction at approximately 530 Ma. Based on these poles and others given in Table 3 of McCausland et al. (2007), a revised late Ediacaran to Cambrian APWP is shown in Figure 6.7. This path shows a polar drift of about 50-60° over a 75 Ma interval, consistent with the APWP utilized by Kirschvink et al. (1997), although it is not temporally constrained enough for interpretation of rapid continental motion. The apparent wander in Ediacaran times prior to 575 Ma is, however, quite large and will need to be more thoroughly constrained before a meaningful interpretation can be made.

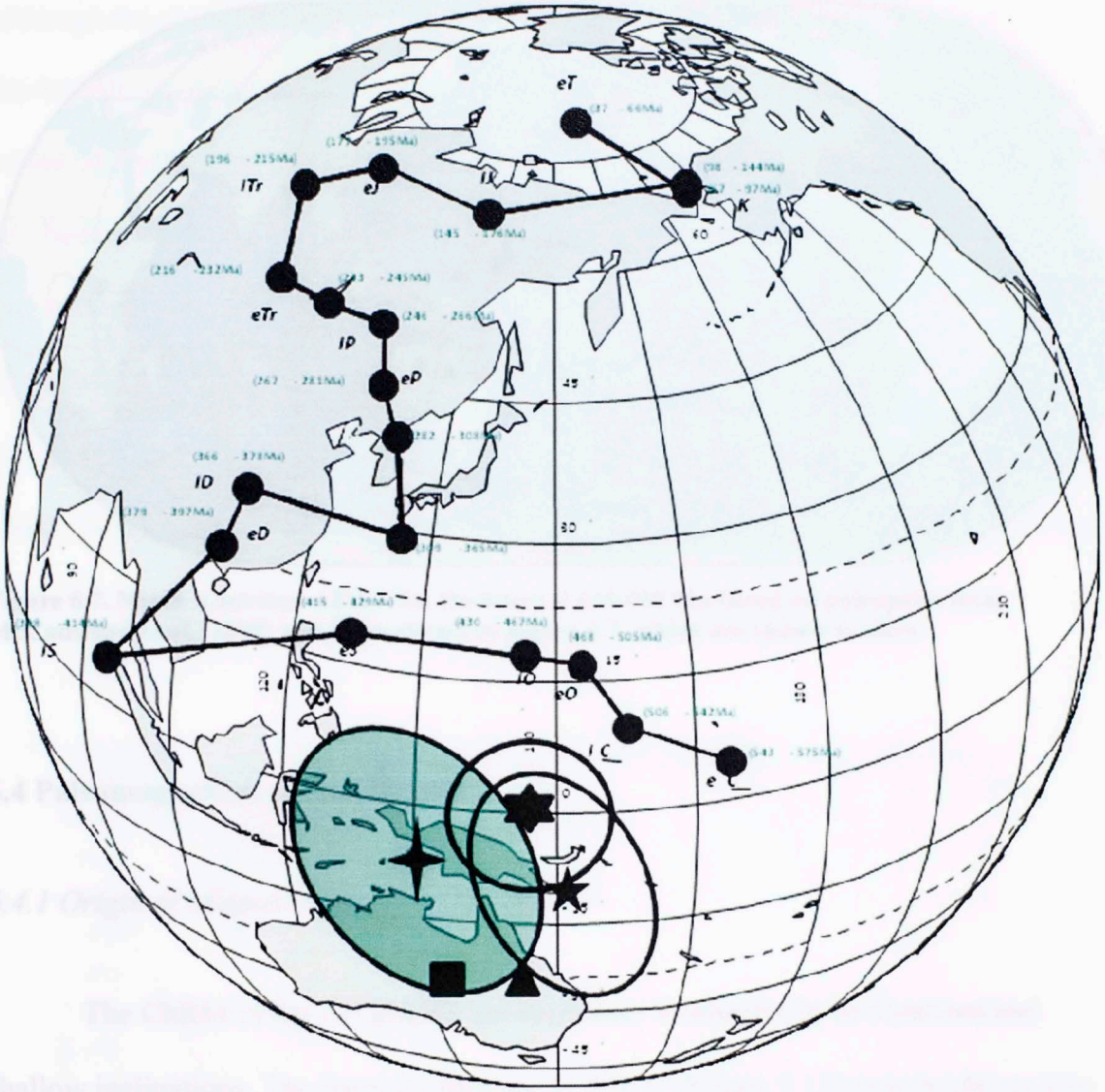

Figure 6.6. North American Phanerozoic APWP and paleopole of Long Mountain Granite green facies compared to poles from similarly-aged rocks. Four point star with green error ellipse is Long Mountain Granite, five point star is ~530 Ma Colbert Rhyolite (Elmore et al., 1998), six point star is from other Wichita Granites (Spall, 1968). Square is pole of Barr and Kirschvink (1983), triangle is pole of Kirschvink et al. (2006). Barr and Kirschvink (1983) and Kirschvink et al. (2006) poles were reported in AGU meeting abstracts that did not contain values for Dp or Dm, and are both from ~524 Ma volcanoclastic deposits in the Puerto Blanco Formation in Mexico (McMenamin, 1987) APWP poles from Van der Voo, 1993.

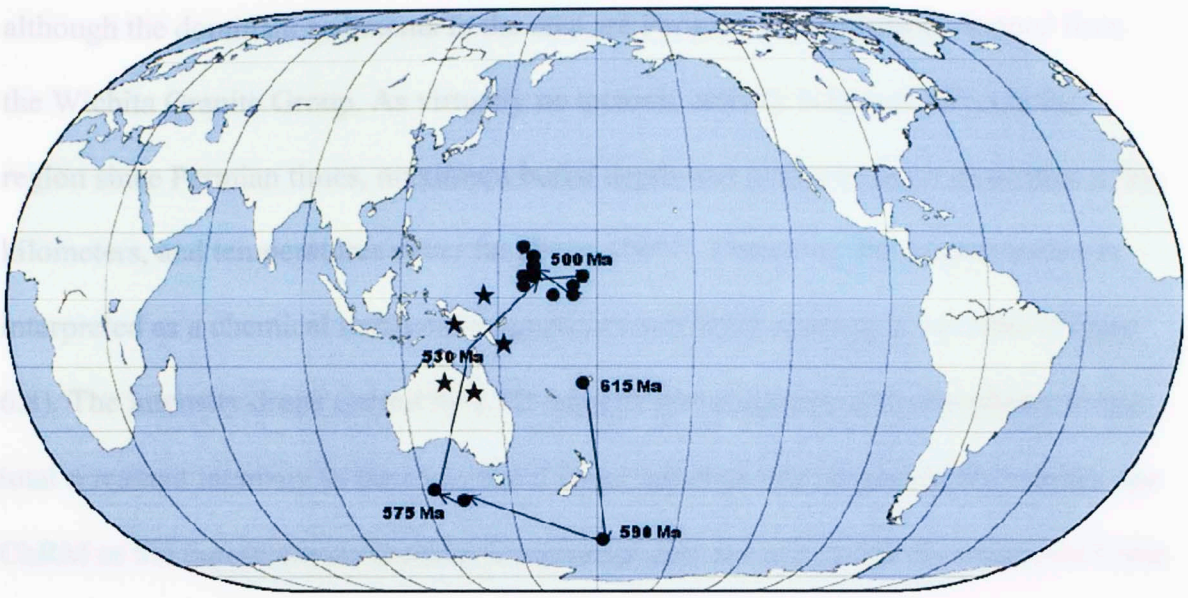

Figure 6.7. North American APWP for the interval 615-500 Ma based on paleopoles from McCausland et al. (2007) and those shown in Figure 6.7, which are shown as stars.

6.4 Paleomagnetism of Red Granite

6.4.1 Origin of Magnetization

The ChRM of the red granite has consistent southeasterly declinations and shallow inclinations. The intensity increase at 425°C (Figure 5.12) may be due to low-temperature removal of a component that is reversed relative to the ChRM; however, this possible low-temperature component cannot be resolved in the current data set.

The ChRM persists to 680°C. In order for this to be a TVRM, the rock would need to have been held at temperatures in excess of 650°C for over 10^9 years according to the time-temperature relations given by Pulliah et al. (1975). There are no indications that the Long Mountain Granite has been exposed to such high temperatures since it crystallized, not to mention the fact that the holding time would be greater than the age of the rock itself. No estimates of maximum burial depth were found in the literature,

although the dominant sediments in the area are Permian conglomerates formed from the Wichita Granite Group. As virtually no tectonic activity is known affected the region since Permian times, maximum burial depth was probably never more than a few kilometers, and temperatures never far above 100°C. Therefore, the magnetization is interpreted as a chemical remanent magnetization (CRM) residing in hematite (Figure 6.8). The intensity drops caused by LTD suggest that magnetite also contributes to the total remanent intensity in the rock, but it is not apparent that magnetite also carries the ChRM as the maximum unblocking temperature persists well above the magnetite Curie temperature.

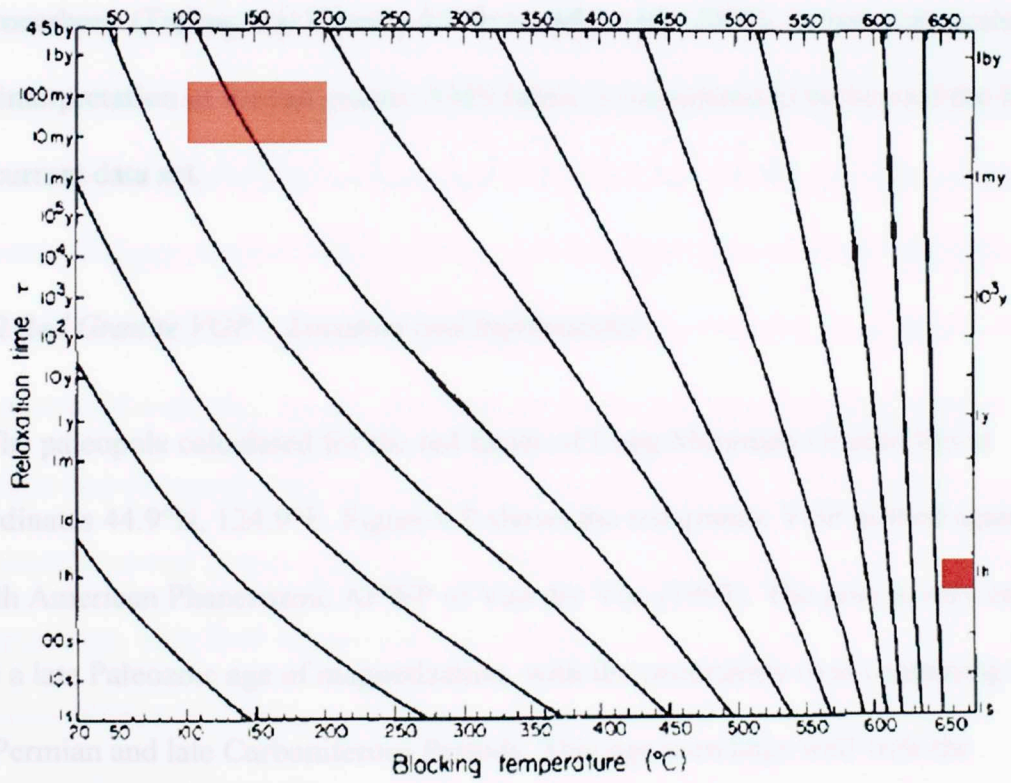

Figure 6.8. Time-temperature relations for hematite from Pulliah et al. (1975). Thermal demagnetization for 1 hour and the highest unblocking temperature for the ChRM of red Long Mountain Granite is indicated by solid red rectangle, likely burial conditions by light red rectangle.

The AMS fabric of the red granite is difficult to interpret. Most studies of secondary AMS fabric in granites are done for purposes of structural geology and seek to correlate AMS fabric with regional strain (Tarling and Hrouda, 1993; e.g., Archanjo et al., 1994, 2002). It is possible that the AMS fabric of the red granite represents a strain fabric; however, strain fabrics generally exhibit a higher degree of magnetic anisotropy than undeformed rocks (Tarling and Hrouda, 1993), and the red facies of the Long Mountain Granite shows much lower levels of anisotropy than does the green facies. There is also no evidence for significant deformation. Another possibility would be to consider the red granite AMS fabric to be analogous to late diagenetic fabrics in sedimentary rocks, which have been interpreted to represent circulation directions of diagenetic fluids and hydrocarbons (Tarling and Hrouda, 1993; Essalhi et al., 2009). A thorough evaluation and interpretation of the red granite AMS fabric is considered to be beyond the limits of the current data set.

6.4.2 Red Granite VGP – Location and Implications

The paleopole calculated for the red facies of Long Mountain Granite lies at coordinates 44.9°N, 124.9°E. Figure 6.9 shows the red granite VGP plotted against the North American Phanerozoic APWP of Van der Voo (1993). The pole is very consistent with a late Paleozoic age of magnetization, with the uncertainty oval containing most of the Permian and late Carboniferous Periods. This age correlates well with the hypothesis of Gilbert (1982) that the Wichita Mountains were uplifted during the Ouachita Orogeny and were exposed during the early and middle Permian.

Recent work on the North American APWP for the Paleozoic has suggested that many of the poles used to constrain the path may be inaccurate due to the effects of inclination shallowing. Bilardello and Kodama (2010a,b) have shown that pole positions from the Carboniferous shift by ~6° or more to the south after correction for inclination shallowing. If their results also apply to the rocks used to constrain the late Paleozoic and Mesozoic parts of the APWP, then the shift of the path would place the paleopole for red Long Mountain Granite at about the late Permian, which is when the rock would have been reburied after surface exposure during the late Paleozoic (Gilbert, 1982).

The presence of epidote along fractures in red granite (Figure 4.3) suggests that the alteration process took place at temperatures in excess of 300°C. These temperatures are too high to be consistent with near-surface groundwaters, but could be attainable by interaction with fluids mobilized during the uplift of the Wichita Mountains Igneous Province. Oxygen isotope studies could potentially shed light on the temperature of alteration, although it is quite possible that low-temperature isotopic equilibration could have occurred well after the alteration that produced the recrystallization textures and hematite and obscured evidence of a high-temperature signal. The temperature range of the alteration event cannot at present be adequately constrained to make a definitive interpretation. This fluid interaction was sufficient to recrystallize some of the alkali feldspars (Figures 6.2, 6.3); possibly even forcing iron into the crystal structure as substitutes for aluminum (Figure 4.20). The paleomagnetic signature of the hematite clearly shows that the red coloration in Long Mountain Granite exposures post-dates intrusion by ~250-300 Ma and is related to tectonic events and/or weathering rather than

deuteric alteration in a magmatic hydrothermal system. The presence of epidote on fracture faces suggests a high temperature of alteration, as does the presence of turbid feldspar (see Section 6.2.1), but without a detailed characterization of epidote occurrence it cannot be definitive.

It is possible that the reddening was caused by weathering fluids, which were postulated by Price et al. (1998) as being responsible for the changes in magnetic properties of the Mount Scott Granite. Wenner and Taylor (1976) proposed, on the basis of oxygen isotopic data, that the red coloration of granites in the St. Francois Mountains of Missouri came about due to interactions with fluids of temperatures below 150°C. Oxygen isotopic data may be useful in this field site, though low-temperature re-equilibration following a high-temperature reddening event could not be ruled out. On the other hand, it could be confirmed by bimodal $\delta^{18}O$ values of red granite samples. A definitive answer cannot be derived from the current data set; although a southward shift of the APWP to correct for inclination shallowing would place the red granite paleopole in the late Permian, which would make it temporally more consistent with alteration via low-temperature weathering fluids rather than hot fluids mobilized by uplift.

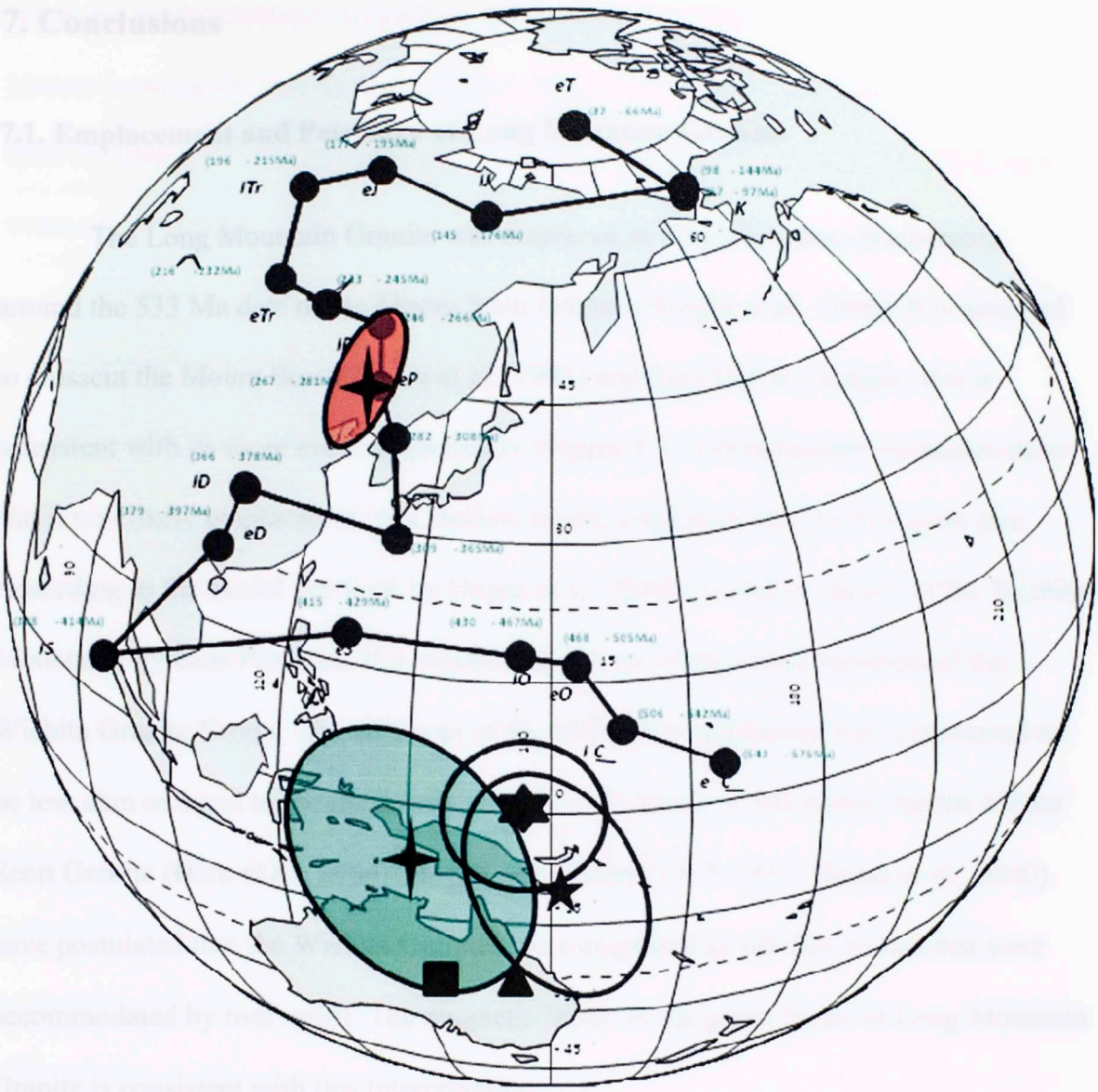

Figure 6.9. Phanerozoic APWP of Van der Voo (1993) with Cambrian paleopoles from Section 6.3 and paleopole from red Long Mountain Granite (with red uncertainty interval.).

7. Conclusions

7.1. Emplacement and Petrology of Long Mountain Granite

The Long Mountain Granite was emplaced in Cambrian time, presumably around the 533 Ma date of the Mount Scott Granite (Wright et al., 1996). It is assumed to crosscut the Mount Scott (Myers et al., 1981) and therefore be younger; this is consistent with its more evolved chemistry (Figure 4.7). Geobarometry estimates show that it was likely emplaced at very shallow levels, consistent with its fine grain size. According to the model put forth by Hogan et al. (2000) for the evolution of the Wichita Mountains Igneous Province, this would make it one of the oldest members of the Wichita Granite Group. The thickness of the sill itself is not known but is presumed to be less than or equal to the maximum published thickness of 500 meters for the Mount Scott Granite (Ham et al., 1964). Hogan and Gilbert (1995, 1997; Hogan et al., 2000) have postulated that the Wichita Granites were emplaced as sill-like bodies that were accommodated by roof uplift. The magnetic fabric of the green facies of Long Mountain Granite is consistent with this interpretation.

The petrography of the Long Mountain Granite is here updated with modern observations. The rock is a microporphyritic alkali feldspar granite composed almost entirely of granophyric intergrowth of quartz and alkali feldspar. All quartz is in optical continuity with granophyre, though in some areas it exhibits evidence of spongy relict cores (Figure 4.11b). Feldspars are universally exsolved perthitic or antiperthitic crystals, even in granophyric feldspar. Some non-granophyric feldspars contain anorthoclase cores with anorthite contents as high as An_{21}, which are interpreted to

represent the first feldspar crystallized from the magma. The feldspars lack the rapakivi texture found in the Mount Scott Granite (Price et al., 1996) and are thought to have been crystallized *in situ*. Variations in exsolution textures of feldspars are interpreted to evince deuteric recrystallization.

Accessory minerals of the Long Mountain Granite include magnetite, ilmenite, zircon, hedenbergite clinopyroxene, hornblende-group amphibole, biotite, fluorite, monazite, chevkinite, bastnaesite, allanite, and relict apatite. Monazite appears to occur as a replacement product of apatite, which is only found as relict cores in monazite or as inclusions in magnetite. Biotite is rarely intact, but an unidentified brown mineral that commonly contains rounded biotite inclusions and has the same morphology as intact biotite grains is interpreted as a deuteric alteration product of primary biotite. Titanite, previously reported as an abundant accessory mineral by Hessa (1964) is not found in samples examined in the current study. The presence of fluorite without biotite is indicative of magmatic fluorine contents in excess of 1 wt. % (Price et al., 1999), though the samples analyzed in this study contain no more than 0.24 wt. % F, indicating fluorine loss. Hornblende has previously been reported as the dominant mafic mineral (Hessa, 1964; Myers et al., 1981) in Long Mountain Granite, but those analyzed in this study appear to contain substantially more hedenbergite than amphibole. Grains tentatively identified as amphibole by petrographic microscope are in actuality stoichiometrically hedenbergite; the essentially Mg-free composition and consequent optical properties may be responsible for previous misidentification. The accessory minerals tend to occur as monomineralic or polymineralic cumulocrysts; the origin of these remains unexplored in detail.

7.2 Paleomagnetism of Long Mountain Granite

Five of six sites in green granite from the study location yield a southeasterly and modern characteristic remanent magnetization. The magnetic fabric of sites in green granite is consistent with results of other workers that have been interpreted as primary fabrics imparted during intrusion of magma bodies. The thermal decay profile is consistent with the ChRM being a thermal or thermoviscous remanent magnetization housed in magnetite. Petrological indicators of alteration of oxide minerals are absent with the exception of rare fractures that contain hematite. These factors suggest that the ChRM represents a primary Cambrian magnetization.

The VGP calculated for the green facies of Long Mountain Granite lies at coordinates .8°N, 314.7° E. These coordinates are consistent with others published for igneous rocks of the Southern Oklahoma Aulacogen (Spall, 1968; Elmore et al., 1998) and with some published from similarly-aged volcanoclastic rocks from Mexico (Barr and Kirschvink, 1983; Kirschvink et al., 2006). In conjunction with these poles, the new results from the Long Mountain Granite are used to constrain the Cambrian apparent polar wander path for North America at ~530 Ma (Figures 6.7, 6.8). This constrained APWP suggests approximately 50-60° of apparent polar wander in the time range of 575 to 500 Ma.

7.3 Origin of Red Granite

The red facies of the Long Mountain Granite in the field is more heavily fractured than the presumably primary green facies and occurs as something of a carapace around the sill. Diabase dikes in wholly reddened granite are much more fissile and heavily altered than their counterparts in green granite. Red coloration is observed to permeate further into the mass of the granite along fracture faces.

Geochemically, the alteration may not have had any significant effects. Few elemental abundances are discernibly different in the current data set, and it is not immediately apparent if any of these are statistically significant. These results are broadly consistent with those of Drake et al. (2008) and Sandström et al. (2010), though there are variations in the specific differences noted.

Petrographically, the formation of red granite coincided with destruction of mafic crystals. Voids left by mafic grains were variably filled with clays, amorphous silica, calcite, and epidote-group minerals. Epidote is also observed to occur along fracture faces in red granite but not in green, indicating that the alteration may have occurred under hydrothermal conditions in excess of 300°C. Most large oxide grains in red granite appear to have been converted to hematite, which is scarce to absent in green granite.

There is evidence of extensive feldspar recrystallization in red granite (e.g., Figures 6.2, 6.3) which led to patchy, turbid, red feldspars. This is consistent with the model of Putnis et al. (2007), who concluded that red coloration in granites is due to hematite precipitation in pore spaces during feldspar recrystallization. Hematite is also dispersed along fractures (e.g., Figure 6.3) and even exsolution planes (Figure 6.4).

Quantitative analysis (Table 4.3) and elemental abundance mapping (Figures 4.19, 4.20) of feldspars indicates that feldspars in red granite contain significantly more iron than do feldspars in green granite. Visual inspection of the X-ray element maps suggests that abundance of iron correlates negatively with that of aluminum (Figure 4.20), suggesting some of it may have been structurally substituted into recrystallized feldspar in addition to precipitation as hematite. Overall iron abundance is the same as green granite, indicating the iron was liberated from destruction of Fe-Ti oxides and mafic silicates rather than externally sourced.

The anisotropy of magnetic susceptibility (AMS) fabric of the Long Mountain Granite was destroyed in the process of reddening. Degree of anisotropy decreased to an average of less than 1%, and susceptibility axes were not retained. The AMS fabric of red granite may preserve a signal of either fluid flow direction during alteration or the stress field at the time; full interpretation of the magnetofabric is beyond the scope of the present study.

Low-temperature demagnetization of red granite shows that at least some multidomain magnetite is still present, but the extent to which this contributes to the ChRM of red granite was not delineated. Under thermal demagnetization, the characteristic component removed is a southeasterly and shallow magnetization that persists up to the Neél temperature of hematite (680°C). In accordance with the time-temperature relaxation relationships given by Pulliah et al. (1975), this is interpreted as a CRM residing in hematite with possible contribution from magnetite. A VGP calculated from six sites in red granite gives a paleopole position of 44.9°N, 124.9°E, which is consistent with the North American APWP for the late Carboniferous and

Permian Periods. This suggests that the hematite responsible for the red coloration was formed by interaction with high-temperature fluids during uplift in late Paleozoic times.

Correction of the APWP may shift the path southward several degrees (Bilardello and Kodama, 2010a, b), which would push back the age of hematite formation to the late Permian. A late Permian alteration would be more consistent with low-temperature weathering fluids than high-temperature fluids associated with uplift; the current study is incapable of fully discerning the conditions of alteration. This would likely require a detailed study of the rock's oxygen and hydrogen isotopic ratios.

The results of this work are not consistent with the hypothesis that red granite is formed deuterically from magmatic-hydrothermal system interactions. Here, there is evidence of deuteric alteration but no evidence that it resulted in red coloration. In the Long Mountain Granite, and likely in other Wichita granites as well, the hematite responsible for the red coloration post-dates the crystallization of the granite by 250-300 million years.

8. References

Abrajevitch, A. and Van der Voo, R. 2010. Incompatible Ediacaran paleomagnetic directions suggest an equatorial geomagnetic dipole hypothesis. *Earth and Planetary Science Letters* **293**, 164-170

Archanjo, C.J., Bouchez, J.L., Corsini, M. and Vauchez, A. 1994. The Pombal granite pluton: magnetic fabric, emplacement and relationships with the Brasiliano strike-slip setting of NE Brazil (Paraiba State). *Journal of Structural Geology* **16**, 323-335

Archanjo, C.J., Launeau, P., Hollanda, M.H.B.M., Macedo, J.W.P. and Liu, D. 2009. Scattering of magnetic fabrics in the Cambrian alkaline granite of Meruoca (Ceará state, northeastern Brazil). *International Journal of Earth Sciences* **98**, 1793-1807

Archanjo, C.J., Trinade, R.I.F., Bouchez, J.L. and Ernesto, M. 2002. Granite fabrics and regional-scale strain partitioning in the Serido belt (Borborema Province, NE Brazil). *Tectonics* **21**, 1-14

Bachmann, O. and Bergantz, G.W. 2004. On the origin of crystal-poor ryolites: Extracted from batholithic crystal mushes. *Journal of Petrology* **45**, 1565-1582

Bacon, C.R. 1989. Crystallization of accessory phases in magmas by local saturation adjacent to phenocrysts. *Geochimica et Cosmochimica Acta* **53**, 1055-1066

Barr, T.D. and Kirschvink, J.L. 1983. The paleoposition of North America in the early Paleozoic: New data from the Caborca Sequence in Sonora, Mexico. *EOS Transactions of the American Geophysical Union* **64**, 689-690

Bilardello, D. and Kodama, K. P. 2010a. Palaeomagnetism and magnetic anisotropy of Carboniferous redbeds from the Maritime Provinces of Canada: evidence for shallow palaeomagnetic inclinations and implications for North American apparent polar wander. *Geophysical Journal International,* **180**, 1013–1029

Bilardello, D. and Kodama, K. P. 2010b. A new inclination shallowing correction of the Mauch Chunk Formation of Pennsylvania, based on high-field AIR results: Implications for the Carboniferous North American APW path and Pangea reconstructions. *Earth and Planetary Science Letters,* **299**, 218–227

Bird, D. and Spieler, A.R. 2004. Epidote in geothermal systems. *Reviews in Mineralogy and Geochemistry* **56**, 235-300

Bonin, B. 2007. A-type granites and related rocks: Evolution of a concept, problems and prospects. *Lithos* **97**, 1-29

Boone, G.M. 1969. Origin of clouded red feldspars: Petrologic contrasts in a granitic porphyry intrusion. *American Journal of Science* **267**, 633-668

Borradaile, G.J., Lucas, K. and Middleton, R.S. 2004. Low-temperature demagnetization isolates stable magnetic vector components in magnetite-bearing diabase. *Geophysical Journal International* **157**, 526-536

Bowring, S.A. and Hoppe, W.J. 1982. U-Pb ages from the Mount Sheridan Gabbro, Wichita Mountains. *In* Gilbert, M.C. and Donovan, R.N. (eds) *Geology of the eastern Wichita Mountains, southwestern Oklahoma.* Oklahoma Geological Survey Guidebook **21**, 54-59

Burke, W.H., Otto, J.B. and Denison, R.E. 1969. Potassium-argon dating of basaltic rocks. *Journal of Geophysical Research* **74**, 1082-1086

Coombs, D.S. 1954. Ferriferous orthoclase from Madagascar. *Mineralogical Magazine*, **226** 409-427

Deer, W.A., Howie, R.A. and Zussman, J. 1992. *An Introduction ot the Rock-Forming Minerals. 2nd Edition.* Pearson Prentice Hall. 696 pp.

Donoghue, E., Troll, V.R. and Harris, C. 2010. Fluid-rock interaction in the Miocene, post-caldera, Tejeda Intrusive Complex, Gran Canaria (Canary Islands): Insights from mineralogy, and O- and H- isotope geochemistry. *Journal of Petrology* **51**, 2149-2176

Donovan, R.N. 1982. Geology of Blue Creek Canyon, Wichita Mountains Area. *In* Gilbert, M.C. and Donovan, R.N. (eds) *Geology of the Eastern Wichita Mountain, Southwestern Oklahoma.* Oklahoma Geological Survey Guidebook **21**, 65-77

Drake, H., Tullborg, E.-L. and Annersten, H. 2008. Red-staining of the wall rock and its influence on the reducing capacity around water conducting fractures. *Applied Geochemistry* **23**, 1898-1920

Dunham, A.C. 1965. The nature and origin of groundmass textures in felsites and granophyres from Rhum, Inverness-shire. *Geolgical Magazine* **102**, 8-23

Dunlop, D.J., Ozdemir, O. and Schmidt, P.W. 1997. Paleomagnetism and paleothermometry of the Sydney Basin 2. Origin of anomalously high unblocking temperatures. *Journal of Geophysical Research* **102**, 27285-27295

Eby, G.N. 1990. The A-Type Granitoids: A review of their occurrence and chemical characteristics and speculation on their petrogenesis. *Lithos* **26**, 115-134

Eby, G.N. 1992. Chemical subdivisions of the A-type granitoids: Petrogenetic and tectonic implications. *Geology* **20**, 641-644

Eliasson, T. Mineralogy, geochemistry and petrophysics of red coloured granite adjacent to fractures. SKB TR-93-06. Svensk K□rnbr□nslehantering AB.

Elmore, R.D., Burr, R., Engel, M. and Parnell, J. 2010. Paleomagnetic dating of fracturing using breccia veins in Durness group carbonates, NW Scotland. *Journal of Structural Geology* **32**, 1933-1942

Elmore, R.D., Campbell, T., Banerjee, S. and Bixler, W.G. 1998. Paleomagnetic dating of ancient fluid-flow events in the Arbuckle Mountains, southern Oklahoma. *In*: Parnell, J. (ed) 1998. *Dating and Duration of Fluid Flow and Fluid-Rock Interaction.* Geological Society of London Special Publications **144**, 9-25

Ernst, W.G. 1960. Diabase-granophyre relations in the Endion Sill, Duluth, Minnesota. *Journal of Petrology* **1**, 286-303

Essalhi, M., Sizaret, S., Barbanson, L., Chen, Y., Branquet, Y., Panis, D., Camps, P., Rochette, P. and Canals, A. 2009. Track of fluid paleocirculation in dolomite host rock at a regional scale by the anisotropy of magnetic susceptibility (AMS): An example from Aptian carbonates of La Florida, northern Spain. *Earth and Planetary Science Letters* **277**, 501-513

Fenn, P.M. 1986. On the origin of graphic granite. *American Mineralogist* **71**, 325-330

Ferré, E.C., Wilson, J. and Gleizes, G. 1999. Magnetic susceptibility and AMS of the Bushveld alkaline granites, South Africa. *Tectonophysics* **307**, 113-133

Ferry, J.M. 1985. Hydrothermal alteration of Tertiary igneous rocks from the Iskle of Skye, northwest Scotland II. Granites. *Contributions to Mineralogy and Petrology* **91**, 283-304

Fisher, R.A. 1953. Dispersion on a sphere. *Royal Society of London Proceedings Series A* **217**, 787-821

Gilbert, M.C. 1982. Geologic setting of the eastern Wichita Mountains, with a brief discussion of unresolved problems. *In* Gilbert, M.C. and Donovan, R.N. (eds) *Geology of the Eastern Wichita Mountains, Southwestern Oklahoma*. Oklahoma Geological Survey Guidebook **21**, 1-30

Gilbert, M.C. and Hogan, J.P. 2010. Our Favorite Outcrop: The Striking but enigmatic granite-gabbro contact of the Wichita Mountains Igneous Province. *Shale Shaker* 130-134

Gilbert, M.C. and Hughes, S.S. 1986. Partial chemical characterization of Cambrian basaltic liquids of the Southern Oklahoma Aulacogen. *In* Gilbert, M.C. (ed.) *Petrology of the Cambrian Wichita Mountains Igneous Suite.* Oklahoma Geological Survey Guidebook **23**, 73-79

Gilbert, M.C. and Myers, J.D. 1986. Overview of the Wichita Granite Group. *In* Gilbert, M.C. (ed.) *Petrology of the Cambrian Wichita Mountains Igneous Suite,* Oklahoma Geological Survey Guidebook **23**, 107-116

Gilbert, M.C., 1983. Timing and chemistry of igneous events associated with the Southern Oklahoma Aulacogen. *Tectonophysics*, **94**, 439-455

Ham, W.E., Denison, R.E. and Merritt, C.A. 1964. Basement rocks and structural evolution of southern Oklahoma. *Oklahoma Gelogical Survey Bulletin* **95**

Hames, W.E., Hogan, J.P., and Gilbert, M.C. 1998. Revised granite-gabbro age relationships, Southern Oklahoma Aulacogen. *In* Hogan, J.P. and Gilbert, M.C. (eds) *Basement Tectonics: Central North America and Other Regions* **12**, 247-249

Hamilton, W. 1959. Chemistry of granophyres from Wichita lopolith, Oklahoma. *Geological Society of America Bulletin* **70**, 1119-1126

Harlov, D.E., Wirth, R. and Förster, H.-J. 2005. An experimental study of dissolution-reprecipitation in fluorapatite: Fluid infiltration and the formation of monazite. *Contributions to Mineralogy and Petrology* **150**, 268-286

Heinrich, E.W. and Moore, D.G. Jr. 1970. Metasomatic potash feldspar rocks associated with igneous alkalic complexes. *The Canadian Mineralogist* **10**(3), 571-584

Herrero-Bervera, E., Walker, G.P.L., Cañon-Tapia, E. and Garcia, M.O. 2001. Magnetic fabric and inferred flow direction of dikes, conesheets and sill swarms, Isle of Skye, Scotland. *Journal of Volcanology and Geothermal Research* **106**, 195-210

Hessa, S. 1964. The igneous geology of the Navajoe Mountains, Oklahoma. University of Oklahoma unpublished M.S. thesis, 40 pages.

Hoffman, P., Dewey, J.F. and Burke, K. 1974. Aulacogens and their genetic relationship to geosynclines, with a Proterozoic example from the Great Slave Lake, Canada. *In* Dutt, R.J. Jr. and Shaver, R.H. (eds) *Modern and Ancient Geosynclinal Sedimentation. Society of Economic Paleontologists and Economic Mineralogists Special Publication* **19**, 38-55

Hogan, J.P. 1993. Monomineralic glomerocrysts: Textural evidence for mineral resorption during crystallization of igneous rocks. *Journal of Geology* **101**, 531-540

Hogan, J.P. and Gilbert, M.C. 1995. The A-Type Mount Scott Granite sheet: Importance of crustal magma traps. *Journal of Geophysical Research* **100**, B8, 779-792

Hogan, J.P. and Gilbert, M.C. 1997. Intrusive Style of A-type sheet granites in a rift environment: The Southern Oklahoma Aulacogen. *In* Ojakanga, R.W., Dickas, A.B.,

and Green, J.C. (eds) *Middle Proterozoic to Cambrian Rifting: Central North America, Geological Society of America Special Paper* **312**, 299-311

Hogan, J.P. and Gilbert, M.C. 1998. The Southern Oklahoma Aulacogen: A Cambrian analog for Mid-Proterozoic AMCG (Anorthosite-Mangerite-Charnockite-Granite) complexes. *In* Hogan, J.P. and Gilbert, M.C. (eds) *Basement Tectonics: Central North America and Other Regions* **12**, 39-78

Hogan, J.P., Barr, D., Bixler, G. and Elmore, R.D. 1994. Paleomagnetic characteristics of the Cambrian Mount Sheridan Gabbro, Southern Oklahoma Aulacogen. *EOS: Transactions of the American Geophysical Union* **75**, 121

Hogan, J.P., Gilbert, M.C. and Price, J.D. 2000. Crystallization of fine- and coarse-grained A-type granite sheets of the Southern Oklahoma Aulacogen, U.S.A. *Transactions of the Royal Society of Edinburgh: Earth Sciences* **91**, 139-150

Isshiki, N. 1958. Notes on Rock Forming Minerals (3). Red coloration of anorthite from Hachijo-jima. *Journal of the Geological Society of Japan* **64**, 644-647

Jelinek, V. 1978. Statistical processing of anisotropy of magnetic susceptibility measured on multiple specimens. *Studia Geophysica et Geodetica* **22**, 50-62

Keller, G.R. and Baldridge, W.S. 1995. The Southern Oklahoma Aulacogen. *In* Olson, K.H. (ed) *Continental Rits: Evolution, Structure, Tectonics. Developments in Geotectonics* **25**. 427-436

Keller, G.R. and Stephenson, R.A. 2007. The Southern Oklahoma and Dniepr-Donets aulacogens: A comparative analysis. *In* Hatcher, R.D., Jr., Carlson, M.P., McBride, J.H. and Martinez Catalan, J.R. (eds). *4-D Frameworkof Continental Crust*. Geological Society of America Memoir **200**, p. 127-143

Keller, G.R., Lidiak, E.G., Hinze, W.J. and Braile, L.W. 1983. The role of rifting in the tectonic development of the midcontinent, U.S.A. *Tectonophysics* **94**, 391-412

Kirschvink, J.L. 1980. The least-square line and plane and the analysis of paleomangetic data. *Geophysical Journal of the Royal Astronomical Society* **62**, 699-781

Kirschvink, J.L., Elston, D.P., Petterson, R., Hagadorn, J.W., Raub, T.D., Evans, D.A., Rose, E.C., Weiss, B.P. and Barr, T.D. 2006. Rapid polar wander in North America during the early Cambrian: Paleomagnetic and magnetostratigraphic constraints from the Puerto Blanco volcanics from Caborca, and the Tapeats Sandstone of the Grand Canyon. *EOS Transactions of the American Geophysical Union* **92**, abstract #GP34A-06

Kirschvink,J.L., Ripperdan, R.L. and Evans, D.A. 1997. Evidence for a large-scale reorganization of Early Cambrian continental masses by inertial interchange true polar wander. *Science* **277**, 541-545

Ku, C.C., Sun, S., Soffel, H. and Scharon, L. 1967. Paleomagnetism of the Basement Rocks, Wichita Mountains, Oklahoma. *Journal of Geophysical Research* **72**, 731-737

Lambert, D.D., Unruh, D.M., and Gilbert, M.C. 1988. Rb-Sr and Sm-Nd isotopic study of the Glen Mountains Layered Complex: Initiation of rifting within the Southern Oklahoma Aulacogen. *Geology* **16**, 13-17

Larson, E.E., Patterson, P.E., Curtis, G., Drake, R. and Mutschler, F.E. 1985. Petrologic, paleomagnetic, and structural evidence of a Paleozoic rift system in Oklahoma, New Mexico, Colorado, and Utah. *Geological Society of America Bulletin* **96**, 1364-1372

Lindqvist, B. 1966. Hydrothermal synthesis studies of potash-bearing sesquioxide-silica systems. *Geologiska Förenigens I Stockholm Förhandlingar* **88**, 133-178

London, D. 2008. *Pegmatites*. The Canadian Mineralogist Special Publication 10. 347 pp.

London, D., Morgan, G.B. VI, and Hervig, R.L. 1989. Vapor-undersaturated experiments with Macusani glass + H_2O at 200 MPa, and the internal differentiation of pegmatites. *Contributions to Mineralogy and Petrology* **102**, 1-17

Lowenstern, J.B., Clynne, M.A. and Bullen, T.D. 1997. Comagmatic A-type granophyre and rhyolite from the Alid volcanic center, Eritrea, Northeast Africa. *Journal of Petrology* **38**, 1707-1721

Lynnes, C.S. and Van der Voo, R. 1984. Paleomagnetism of the Cambro-Ordovician McClure Mountain alkalic complex, Colorado. *Earth and Planetary Science Letters* **71**, 163-172

Mattsson, H. and Thunehed, H. 2004. Interpretation of geophysical borehole data and compilation of petrophysical data from KSH02 (80-1000 m) and KAV01. Oskarshamn site investigation. SKB P-04-77. Svensk K□rnbr□nslehantering AB

McCausland, P.J.A., Van der Voo, R. and Hall, C.M. 2007. Circum-Iapetus paleogeography of the Precambrian-Cambrian transition with a new paleomagnetic constraint from Laurentia. *Precambrian Research* **156**, 125-152

McConnell, D.A. and Gilbert, M.C. 1986. Calculations for Cambrian extension of the Southern Oklahoma Aulacogen. *In* Gilbert, M.C. (ed.) *Petrology of the Cambrian Wichita Mountains Igneous Suite.* Oklahoma Geological Survey Guidebook **23**, 11-20

McConnell, D.A. and Gilbert, M.C. 1990. Cambrian extensional tectonics and magmatism within the Southern Oklahoma Aulacogen. *Tectonophysics* **174**, 147-157

McMenamin, M.A.S. 1987. Lower Cambrian Trilobites, Zonation, and Correlation of the Puerto Blanco Formation, Sonora, Mexico. *Journal of Paleontology* **61**, 738-749

Merritt, C.A. 1967. Names and relative ages of granites and rhyolites in the Wichita Mountains. *Oklahoma Geology Notes* **26**, 45-53

Morgan, G.B. VI and London, D. 1996. Optimizing the electron microanalysis of hydrous alkali aluminosilicate glasses. *American Mineralogist*, **81**, 1176-1185

Myers, J.D., Gilbert, M.C. and Loiselle, M.C. 1981. Geochemistry of the Cambrian Wichita Granite Group and revisions of its lithostratigraphy. *Oklahoma Geology Notes* **41**, 172-195

Nakano, S., Akai, J. and Shimobayashu, N. 2005. Contrasting Fe-Ca distributions and related microtextures in syenite alkali feldspar from the Patagonian Andes, Chile. *Mineralogical Magazine* **69**, 521-535

Neumann, H. and Christie, O.H. 1962. Observations on plagioclase aventurines from sourthern Norway. *Norsk Geologisk Tidsskrift* **42**(2), 389-393

Parsons, I. 1978. Feldspars and fluids in cooling plutons. *Mineralogical Magazine* **42**, 1-17

Parsons, I. and Becker, S.M. 1986. High-temperature fluid-rock interactions in a layered syenite pluton. *Nature* **321**, 764-766

Parsons, I. and Lee, M.R. 2009. Mutual replacement reactions in alkali feldspars I: Microtextures and mechanisms. *Contributions to Mineralogy and Petrology* **157**, 641-661

Petersen, J.S. and Lofgren, G.E. 1986. Lamellar and patchy intergrowths in feldspars: Experimental crystallization of eutectic silicates. *American Mineralogist* **71**, 343-355

Plümper, O. and Putnis, A. 2009. The complex hydrothermal history of granitic rocks: Multiple feldspar replacement reactions under subsolidus conditions. *Journal of Petrology* **50**, 967-987

Pouchou, J.L. and Pichoir, F. 1985. "PAP" φ(ρz) correction procedure for improved microanalysis. In: Armstrong, J.T. (ed.) *Microbeam Analysis*, p. 104-106. San Francisco Press, California.

Powell, B.N. 1982. Roosevelt Gabbros (Raggedy Mountain Granite Group) Wichita Mountains. *In* Gilbert, M.C. and Donovan, R.N. (eds) *Geology of the eastern Wichita*

Mountains, southwestern Oklahoma. Oklahoma Geological Survey Guidebook **21**, 51-53

Powell, B.N. and Phelps, D.W. 1977. Igneous cumulates of the Wichita province and their tectonic implication. *Geology* **5**, 52-56

Powell, B.N., Gilbert, M.C. and Fischer J.F. 1980. Lithostratigraphic classification of basement rocks of the Wichita Province, Oklahoma: Summary. *Geological Society of America Bulletin* **91**, 509-514

Price, J.D. 1998. Petrology of the Mount Scott Granite. Ph.D. Thesis, University of Oklahoma, Norman. 240pp.

Price, J.D., Hogan, J.P. and Gilbert, M.C. 1996. Rapakivi texture in the Mount Scott Granite, Wichita Mountains, Oklahoma. *European Journal of Mineralogy* **8**, 435-451

Price, J.D., Hogan, J.P., Gilbert, M.C. and Payne, J.D. 1998. Surface and near-surface investigation of the alteration of the Mount Scott Granite and geometry of the Sandy Creek Gabbro pluton, Hale Spring area, Wichita Mountains, Oklahoma. *In* Hogan, J.P. and Gilbert, M.C. (eds). *Basement Tectonics: Central North America and Other Regions* **12**, 79-122

Price, J.D., Hogan, J.P., Gilbert, M.C., London, D.L. and Morgan, G.B. VI. 1999. Experimental study of titanite-fluorite equilibria in the A-type Mount Scott Granite: Implications for assessing F contents of felsic magma. *Geology* **27**, 951-954

Pulliah, G., Irving, E., Buchan, K.L. and Dunlop, D.J. 1975. Magnetization changes caused by burial and uplift. *Earth and Planetary Science Letters* **28** 133-143

Putnis, A., Hinrichs, R., Putnis, C.V., Golla-Schindler, U. and Collins, L.G. 2007. Hematite in porous red-clouded feldspars: Evidence of large-scale crustal fluid-rock interaction. *Lithos* **95**, 10-18

Robbins, S.L. and Keller, G.R. 1992. Complete Bouguer and isostatic residual gravity maps of the Anadarko Basin, Wichita Mountains, and surrounding areas, Oklahoma, Kansas, Texas, and Colorado. *U.S. Geological Survey Bulletin* **1866G**

Rochette, P., Jackson, M. and Auborg, C. 1992. Rock magnetism and the interpretation of anisotropy of magnetic susceptibility. *Reviews of Geophysics* **30**, 209-226

Rochette, P., Jenatton, L., Boudier, F. and Reuber, I. 1991. Diabase dikes emplacement in the Oman Ophiolite: A magnetic fabric study with reference to geochemistry. *In* Peters, T., Nicolas, A. and Coleman, R.G. (eds.) *Ophiolite Genesis and Evolution of the Ocieanic Lithosphere*, p. 55-82

Roggenthen, W.M., Fischer, J.F., Napoleone, G. and Fischer, A.G. 1981. Paleomagnetism and age of mafic plutons, Wichita Mountains, Oklahoma. *Geophysical Research Letters* **8**, 133-136

Rosenqvist, I.T.1951. Investigations in the crystal chemistry of silicates III. The relation haematite-microcline. *Norsk Geologisk Tidsskrift* **29**, 65-76

Sandström, B.,Annersten, H. and Tullborg, E.-L. 2010. Fracture-related hydrothermal alteration of metagranitic rock and associated changes in mineralogy, geochemistry, and degree of oxidation: a case study at Forsmark, central Sweden. *International Journal of Earth Sciences* **99**, 1-25

Shatski, N.S. 1946. The Great Donets Basin and the Wichita system: comparative tectonics of ancient platforms. *Akademiya Nauk SSSR Izvestiya, Seriya Geologicheskaya* **6**, 57-90

Spall, H. 1968. Paleomagnetism of basement granites of Southern Oklahoma and its implications: Progress report. *Oklahoma Geology Notes* **28**, 65-80

Stevenson, C.T.E., Owens, W.H., Hutton, D.H.W., Hood, D.N. and Meighan, I.G. 2007. Laccolithic, as opposed to cauldron subsidence, emplacement of the Eastern Mourne pluton, N. Ireland: Evidence from anisotropy of magnetic susceptibility. *Journal of the Geological Society, London* **164**, 99-110

Tarling, D.H. and Hrouda, F. 1993. *The Magnetic Anisotropy of Rocks*. Chapman & Hall, 217 pp.

Taylor, C.H. 1915. Granites of Oklahoma. *Oklahoma Geological Survey Bulletin* **20**.

Taylor, H.P. Jr. 1977. Water/rock interactions and the origin of H_2O in granitic batholiths. *Journal of the Geological Society, London* **133**, 509-558

Tilton, G.R., Wetherill, G.W. and Davis, G.L. 1962. Mineral Ages from the Wichita and Arbuckle Mountains, Oklahoma, and the St. Francois Mountains, Missouri. *Journal of Geophysical Research* **67**, 4011-4019

Van der voo, R. 1993. *Paleomagnetism of the Atlantic, Tethys, and Iapetus Oceans.* Cambridge University Press, 411pp.

Vance, J.A. 1969. On synneusis. *Contributions to Mineralogy and Petrology* **24**, 7-29

Vogt, J.H.L. 1921. The physical chemistry of the crystallization and magmatic differentiation of igneous rocks. *Journal of Geology* **28**, 318-350

Waldron, K.A. and Parsons, I. 1992. Feldspar microtextures and multistage thermal history of syenites from the Coldwell Complex, Ontario. *Contributions to Mineralogy and Petrology* **111**, 222-234

Watts, D.R., Van der Voo, R. and Reeve, S.C. 1980. Cambrian paleomagnetism of the Llano Uplift, Texas. *Journal of Geophysical Research* **85**, 5316-5330

Weaver, B.L. and Gilbert, M.C. Reconnaisance geochemistry of silicic igneous rocks of the Wichita Mountains: The Wichita Granite Group and the Carlton Rhyolite Group. *In* Gilbert, M.C. (ed.) *Petrology of the Cambrian Wichta Mountains Igneous Suite.* Oklahoma Geological Survey Guidebook **23**, 117-125

Wenner, D.B. and Taylor, H.P. Jr. 1976. Oxygen and hydrogen isotope studies of a Precambrian granite-rhyolite terrane, St. Francois Mountains, southeastern Missour. *Geological Society of America Bulletin* **87**, 1587-1598

Whalen, J.B., Currie, K.L. and Chappell, B.W. 1987. A-type granites: geochemical characteristics, discrimination and petrogenesis. *Contributions to Mineralogy and Petrology* **95**, 407-419

Wohletz, K. 2008. KWare Heat3D: A multithreaded, 3-D, heterogeneous, heat flow simulator, useful for modeling magma chamber evolution. Available at http://internet.cybermesa.com/~wohletz/KWare/KWare.htm

Wolf, M.B. and London, D. 1995. Incongruent dissolution of REE- and Sr-rich apatite in peraluminous granitic liquids: Differential apatite, monazite, and xenotime solubilities during anatexis. *American Mineralogist* **80**, 765-775

Wones, D.R. and Appleman, D.E. 1961. X-ray crystallography and optical properties of synthetic monoclinic $KFeSi_3O_8$, iron-sanidine. U.S. Geological Survey Professional Paper 424-C, p. C309-C310

Worden, R.H., Walker, F.D.L., Parsons, I. and Brown, W.L. 1990. Development of microporosity, diffusion channels and deuteric coarsening in perthitic alkali feldspars. *Contributions to Mineralogy and Petrology* **104**, 507-515

Wright, J.E., Hogan, J.P. and Gilbert, M.C. 1996. The Southern Oklahoma Aulacogen: Not just another B.L.I.P. *EOS: Transactions of the American Geophysical Union* **77**, 46, F845.

Zhang, B. and Halls, H.C. 1995. The origin and age of feldspar clouding in the Matachewan dyke swarm, Canada. *In* Baer, G. and Heimann, A. (eds.) *Physics and Chemistry of Dykes* 171-176

Zijderveld, J.D.A. 1967. A.C. demagnetization of rocks: analysis of results. *In* Collinson, D.W., Creer, K.M. and Runcorn, S.K. (eds). *Methods in Paleomagnetism*. Elsevier, p. 254-286

Appendix – Quantitative Electron Microprobe Analyses

Table A-1. Quantitative analyses of feldspars

	Weight Percent Oxides					
Label	**SiO_2**	**Al_2O_3**	**Fe_2O_3**	**CaO**	**Na_2O**	**K_2O**
SG-2						
Anorthoclase-1, line-1						
SG2-1 AC-L1_1	66.19	19.14	0.53	0.56	7.68	5.23
SG2-1 AC-L1_2	65.82	18.97	0.21	0.39	6.41	7.17
SG2-1 AC-L1_3	66.12	19.03	0.27	0.42	7.12	6.05
SG2-1 AC-L1_4	66.01	19.08	0.32	0.44	6.97	6.33
SG2-1 AC-L1_5	65.82	19.06	0.39	0.45	6.46	6.93
SG2-1 AC-L1_6	65.90	18.83	0.47	0.45	6.71	6.54
SG2-1 AC-L1_7	65.75	18.94	0.42	0.40	6.46	6.92
SG2-1 AC-L1_8	65.66	19.02	0.70	0.48	6.92	5.83
SG2-1 AC-L1_9	65.82	18.88	0.58	0.57	6.69	6.10
SG2-1 AC-L1_10	65.78	18.88	0.33	0.26	5.35	8.46
SG2-1 AC-L1_11	66.04	18.77	0.35	0.39	6.38	6.93
SG2-1 AC-L1_12	65.77	18.88	0.72	0.43	6.17	7.66
SG2-1 AC-L1_13	65.33	18.55	0.87	0.27	5.74	7.70
SG2-1 AC-L1_14	65.75	18.75	0.73	0.34	6.09	7.68
SG2-1 AC-L1_15	65.94	18.83	0.32	0.27	5.59	8.56
SG2-1 AC-L1_16	66.17	19.10	0.38	0.28	6.85	6.93
SG2-1 AC-L1_17	65.47	18.63	0.37	0.18	4.77	9.31
Anorthoclase, line-2						
SG2-1 AC-L2_1	66.29	19.45	0.12	0.57	7.39	5.37
SG2-1 AC-L2_2	65.67	19.22	0.15	1.32	7.50	5.24
SG2-1 AC-L2_3	66.04	19.26	0.46	0.54	7.59	5.36
SG2-1 AC-L2_4	65.73	19.13	0.44	0.55	7.13	5.92
SG2-1 AC-L2_5	65.96	19.02	0.29	0.47	6.70	6.30
SG2-1 AC-L2_6	66.29	19.25	0.15	0.40	7.10	6.14
SG2-1 AC-L2_7	66.02	19.26	0.38	0.43	6.76	6.61
SG2-1 AC-L2_8	66.28	19.32	0.25	0.40	7.28	5.93
SG2-1 AC-L2_9	65.63	19.17	0.50	0.62	7.14	6.21
SG2-1 AC-L2_10	65.78	19.18	0.95	0.79	7.49	5.30
SG2-1 AC-L2_11	66.17	19.31	0.33	0.50	7.10	5.76
SG2-1 AC-L2_12	65.89	18.87	0.16	0.33	6.16	7.53
SG2-1 AC-L2_13	65.56	18.79	0.32	0.25	5.52	8.14
SG2-1 AC-L2_14	65.40	18.83	0.28	0.20	4.53	9.30
SG2-1 AC-L2_15	64.98	18.65	0.30	0.68	5.37	8.43

SG2-1 AC-L2_16	66.25	18.88	0.19	0.24	6.17	7.30
SG2-1 AC-L2_17	65.79	18.77	0.12	0.21	5.98	8.02
SG2-1 AC-L2_18	66.23	18.90	0.42	0.37	7.10	6.16
SG2-1 AC-L2_19	65.71	18.95	0.37	0.52	6.02	7.40
SG2-1 AC-L2_20	66.17	18.97	0.48	0.25	6.29	7.47
SG2-1 AC-L2_21	64.92	18.29	0.84	0.50	4.19	9.64
Anorthoclase, line-3						
SG2-1 AC-L3_1	66.38	19.43	0.11	0.56	7.67	5.04
SG2-1 AC-L3_2	66.11	19.30	0.24	0.56	7.47	5.26
SG2-1 AC-L3_3	66.44	19.40	0.14	0.59	8.14	4.59
SG2-1 AC-L3_4	66.14	19.33	0.54	0.66	7.68	4.83
SG2-1 AC-L3_5	65.90	19.56	0.27	0.95	7.73	4.94
SG2-1 AC-L3_6	66.18	19.52	0.16	0.65	7.62	5.12
SG2-1 AC-L3_7	66.68	19.62	0.12	0.72	8.68	3.64
SG2-1 AC-L3_8	65.26	19.25	0.35	1.58	7.37	5.19
SG2-1 AC-L3_9	66.46	19.65	0.22	1.04	8.62	3.71
SG2-1 AC-L3_10	65.67	19.20	0.27	0.58	6.91	6.27
SG2-1 AC-L3_11	65.17	19.07	0.98	0.55	6.32	6.93
SG2-1 AC-L3_12	66.14	19.23	0.36	0.54	6.97	6.13
SG2-1 AC-L3_13	65.99	18.98	0.23	0.43	6.42	6.85
SG2-1 AC-L3_14	65.83	19.07	0.13	0.42	7.33	5.87
SG2-1 AC-L3_15	65.93	18.94	0.69	0.48	7.10	6.29
SG2-1 AC-L3_16	65.98	18.91	0.09	0.40	6.75	6.33
SG2-1 AC-L3_17	66.41	19.31	0.21	0.41	7.21	5.83
SG2-1 AC-L3_18	65.87	19.00	0.12	0.38	6.76	6.78
SG2-1 AC-L3_19	65.89	19.03	0.12	0.34	6.12	7.70
SG2-1 AC-L3_20	65.05	18.93	0.99	1.11	6.44	6.78
SG2-1 AC-L3_21	65.82	18.99	0.51	0.44	6.04	7.45
SG2-1 AC-L3_22	65.93	19.18	0.12	0.39	6.44	7.00
SG2-1 AC-L3_23	66.20	19.16	0.15	0.85	7.57	5.19
SG2-1 AC-L3_24	66.00	19.05	0.35	0.41	6.85	6.78
SG2-1 AC-L3_25	66.28	19.05	0.23	0.37	6.79	6.71
SG2-1 AC-L3_26	65.92	19.03	0.42	0.46	6.98	6.41
AC-1 Avg	**65.90**	**19.06**	**0.37**	**0.51**	**6.73**	**6.52**
Std Dev	0.36	0.26	0.23	0.25	0.86	1.25
Granophyre-1, line-1						
SG2-1 GP1-2_1	65.78	18.30	0.33	0.04	3.06	12.16
SG2-1 GP1-2_2	66.26	18.44	0.95	0.24	5.02	9.05
SG2-1 GP1-2_3	66.16	18.38	0.51	0.07	3.75	10.98
SG2-1 GP1-2_4	65.49	18.28	0.21	0.03	2.96	12.27

SG2-1 GP1-2_5	65.62	18.22	0.43	0.03	3.02	12.12
SG2-1 GP1-2_6	66.15	18.27	0.49	0.04	4.33	10.40
SG2-1 GP1-2_7	65.82	18.39	0.49	0.07	3.42	11.54
SG2-1 GP1-2_8	65.61	18.09	0.22	0.02	2.25	13.22
SG2-1 GP1-2_11	66.25	18.56	0.84	0.14	5.99	7.84
SG2-1 GP1-2_16	65.52	18.26	0.39	0.07	2.32	13.09
SG2-1 GP1-2_17	70.29	17.83	1.00	0.50	9.86	1.27
SG2-1 GP1-2_18	68.36	18.55	0.49	0.11	8.80	3.78
SG2-1 GP1-2_34	68.44	16.81	0.22	0.41	3.63	9.86
SG2-1 GP1-2_44	66.82	18.65	0.49	0.18	6.55	6.86
SG2-1 GP1-2_45	66.06	18.55	0.32	0.16	4.80	9.63
GP-1 Avg	**66.58**	**18.24**	**0.49**	**0.14**	**4.65**	**9.61**
Std Dev	1.38	0.45	0.25	0.14	2.28	3.44
Anorthoclase-2, line-1						
SG2-1 AC2-L1_1	66.00	19.10	0.12	0.36	6.50	6.81
SG2-1 AC2-L1_2	66.06	19.34	0.08	0.46	6.64	6.39
SG2-1 AC2-L1_3	66.17	19.23	0.12	0.53	7.10	6.06
SG2-1 AC2-L1_4	66.04	19.38	0.12	0.48	6.92	6.21
SG2-1 AC2-L1_5	66.64	19.79	0.13	0.58	8.73	3.83
SG2-1 AC2-L1_6	66.22	19.34	0.10	0.49	7.29	5.47
SG2-1 AC2-L1_7	66.53	19.56	0.13	0.54	7.84	4.80
SG2-1 AC2-L1_8	65.91	19.16	0.08	0.62	6.50	6.43
SG2-1 AC2-L1_9	66.37	19.35	0.13	0.60	7.37	5.35
SG2-1 AC2-L1_10	65.92	19.24	0.10	0.72	6.54	6.71
SG2-1 AC2-L1_11	65.92	19.18	0.19	0.62	6.90	5.95
SG2-1 AC2-L1_12	65.85	19.27	0.26	0.52	6.76	6.23
SG2-1 AC2-L1_13	66.50	19.53	0.09	0.61	7.99	4.68
SG2-1 AC2-L1_14	65.67	18.87	0.28	0.82	6.14	7.39
SG2-1 AC2-L1_16	66.31	19.41	0.14	0.51	7.46	5.48
SG2-1 AC2-L1_17	66.21	19.18	0.16	0.54	7.36	5.52
SG2-1 AC2-L1_18	66.14	19.29	0.16	0.58	7.36	5.66
SG2-1 AC2-L1_19	66.13	19.35	0.14	0.50	6.68	6.03
SG2-1 AC2-L1_20	66.49	19.42	0.17	0.55	7.70	5.09
SG2-1 AC2-L1_21	66.35	19.57	0.12	0.46	7.59	5.15

SG2-1 AC2-L1_22	66.07	19.29	0.11	0.45	6.99	5.90
SG2-1 AC2-L1_23	66.41	19.25	0.18	0.48	7.59	5.26
SG2-1 AC2-L1_24	66.08	19.40	0.16	0.45	6.80	6.20
SG2-1 AC2-L1_25	66.18	19.19	0.13	0.42	6.64	6.29
SG2-1 AC2-L1_26	66.29	19.22	0.16	0.44	6.65	6.40
SG2-1 AC2-L1_27	66.27	19.23	0.39	0.59	7.52	4.92
SG2-1 AC2-L1_28	66.19	19.43	0.25	0.55	7.56	5.16
SG2-1 AC2-L1_29	66.49	19.54	0.18	0.57	8.05	4.38
SG2-1 AC2-L1_30	66.80	19.79	0.10	0.67	8.96	3.50
Anorthoclase-2, line-2						
SG2-1 AC2-L2_1	65.34	18.79	0.20	0.18	4.41	9.96
SG2-1 AC2-L2_2	65.64	18.89	0.17	0.30	5.46	8.57
SG2-1 AC2-L2_3	65.00	18.88	0.30	1.14	5.99	7.49
SG2-1 AC2-L2_4	65.76	18.85	0.14	0.40	6.05	7.53
SG2-1 AC2-L2_5	65.40	18.93	0.31	0.74	6.57	6.65
SG2-1 AC2-L2_6	65.53	19.16	0.31	0.61	6.28	7.12
SG2-1 AC2-L2_7	66.00	19.22	0.24	0.44	6.80	6.55
SG2-1 AC2-L2_8	65.54	19.03	0.18	0.38	6.12	7.43
SG2-1 AC2-L2_9	65.99	19.23	0.42	0.46	6.89	6.29
SG2-1 AC2-L2_10	65.69	19.12	0.18	0.37	6.18	7.52
SG2-1 AC2-L2_11	66.28	19.08	0.17	0.50	7.39	5.73
SG2-1 AC2-L2_12	64.77	18.54	0.24	1.17	4.72	9.05
SG2-1 AC2-L2_13	66.12	19.18	0.20	0.48	6.75	6.29
SG2-1 AC2-L2_14	65.89	19.14	0.19	0.47	6.16	7.11
SG2-1 AC2-L2_15	66.31	19.41	0.17	0.52	7.52	5.21
SG2-1 AC2-L2_16	65.87	19.03	0.09	0.38	6.29	6.94
SG2-1 AC2-L2_17	65.69	19.26	0.08	0.46	6.15	7.22
SG2-1 AC2-L2_18	66.46	19.85	0.23	0.85	8.59	3.66
SG2-1 AC2-L2_21	66.15	20.60	0.12	1.52	10.33	1.04
SG2-1 AC2-L2_22	66.31	20.60	0.11	1.50	9.79	1.50

SG2-1 AC2-L2_23	66.59	20.82	0.14	1.61	10.32	0.62
SG2-1 AC2-L2_24	66.59	20.66	0.18	1.59	10.30	0.67
SG2-1 AC2-L2_26	65.78	19.59	0.31	1.12	8.45	3.57
SG2-1 AC2-L2_27	67.26	20.36	0.11	1.27	10.72	0.41
SG2-1 AC2-L2_28	62.98	18.78	0.43	4.30	7.41	4.89
SG2-1 AC2-L2_29	65.69	19.52	0.53	0.74	7.58	5.17
AC-1 Avg	**66.01**	**19.37**	**0.19**	**0.71**	**7.26**	**5.59**
Std Dev	0.60	0.47	0.10	0.59	1.30	1.97
Granophyre-2, line-1						
SG2-1 GP2-1_1	65.54	18.39	0.39	0.04	2.04	13.39
SG2-1 GP2-1_4	65.36	18.16	0.17	0.01	1.50	14.21
SG2-1 GP2-1_5	65.79	18.57	0.55	0.16	3.39	11.23
SG2-1 GP2-1_6	66.66	18.50	0.57	0.18	5.96	7.39
SG2-1 GP2-1_11	66.34	18.34	1.20	0.10	4.84	9.10
SG2-1 GP2-1_13	64.13	18.19	1.04	0.15	1.39	14.06
SG2-1 GP2-1_14	63.60	17.66	0.24	0.01	1.13	14.25
SG2-1 GP2-1_17	64.93	18.09	0.82	0.11	2.10	12.78
SG2-1 GP2-1_21	65.51	18.33	0.47	0.22	3.06	11.84
SG2-1 GP2-1_27	65.88	18.08	0.41	0.09	5.06	9.01
SG2-1 GP2-1_30	65.78	18.28	0.66	0.07	3.95	10.60
GP-2 Avg	**65.41**	**18.24**	**0.59**	**0.10**	**3.13**	**11.62**
Std Dev	0.90	0.25	0.32	0.07	1.65	2.37
SR-1						
Anorthoclase-1, line-1						
SR1-3 AC 1-1_1	65.44	19.06	0.45	0.37	5.95	7.94
SR1-3 AC 1-1_2	66.20	19.21	0.28	0.30	6.09	7.38
SR1-3 AC 1-1_3	65.83	19.02	0.29	0.22	5.49	8.32
SR1-3 AC 1-1_4	66.21	19.14	0.20	0.27	6.53	7.00
SR1-3 AC 1-1_5	65.47	18.79	0.79	0.22	5.74	7.61
SR1-3 AC 1-1_6	66.12	19.20	0.23	0.37	7.05	6.45
SR1-3 AC 1-1_7	65.89	18.92	0.94	0.37	7.27	6.00
SR1-3 AC 1-1_8	65.21	18.49	0.64	0.16	4.70	9.28
SR1-3 AC 1-1_9	65.61	18.71	0.51	0.27	6.00	7.58
SR1-3 AC 1-1_10	65.91	18.76	0.55	0.21	5.90	8.07
SR1-3 AC 1-1_11	65.20	18.43	0.88	0.18	5.72	8.15
SR1-3 AC 1-1_14	65.04	18.63	1.35	0.23	6.15	7.37

SR1-3 AC 1-1_15	65.36	18.78	0.79	0.18	5.51	8.54
SR1-3 AC 1-1_16	64.81	18.45	1.51	0.23	5.86	7.68
SR1-3 AC 1-1_18	64.91	18.61	1.01	0.21	5.34	8.40
SR1-3 AC 1-1_19	65.49	18.59	0.85	0.20	5.77	8.01
Anorthoclase-1, line-2						
SR1-3 AC 1-2_1	65.46	18.74	1.56	0.42	7.18	5.69
SR1-3 AC 1-2_2	64.75	18.93	2.82	0.41	7.87	4.95
SR1-3 AC 1-2_4	65.15	18.83	1.17	0.32	5.56	7.98
SR1-3 AC 1-2_5	65.66	18.76	0.55	0.34	6.28	7.39
SR1-3 AC 1-2_6	66.17	19.04	0.28	0.36	7.04	6.24
SR1-3 AC 1-2_7	64.79	18.52	1.40	0.18	5.22	8.49
SR1-3 AC 1-2_9	65.59	18.87	0.47	0.33	5.70	8.16
SR1-3 AC 1-2_10	65.59	18.89	1.13	0.28	6.48	6.69
SR1-3 AC 1-2_11	65.55	18.74	0.53	0.31	5.87	7.81
SR1-3 AC 1-2_12	65.32	18.77	0.32	0.16	4.29	10.07
SR1-3 AC 1-2_14	64.86	18.67	0.64	0.15	3.98	10.43
SR1-3 AC 1-2_15	64.87	18.60	0.83	0.46	4.99	8.96
SR1-3 AC 1-2_16	65.23	18.69	1.28	0.28	6.63	6.75
SR1-3 AC 1-2_17	65.34	18.88	0.61	0.23	5.56	8.17
SR1-3 AC 1-2_18	65.79	19.01	0.52	0.36	6.55	6.89
SR1-3 AC 1-2_19	65.18	18.71	0.76	0.22	5.30	8.73
AC-1 Avg	**65.44**	**18.79**	**0.82**	**0.27**	**5.92**	**7.72**
Std Dev	0.43	0.21	0.53	0.09	0.85	1.18
Granophyre-1, line-1						
SR1-3 GP 1-1_2	64.51	18.17	1.07	0.01	1.32	14.31
SR1-3 GP 1-1_3	65.01	18.28	0.43	0.00	1.00	14.85
SR1-3 GP 1-1_4	65.20	18.29	0.17	0.00	0.95	14.98
SR1-3 GP 1-1_5	65.72	18.05	0.50	0.02	1.64	13.56
SR1-3 GP 1-1_10	66.88	18.54	0.65	0.05	6.57	7.47
SR1-3 GP 1-1_11	65.22	18.36	0.39	0.02	1.91	13.85
SR1-3 GP 1-1_12	65.07	18.20	0.27	0.00	1.11	14.80
SR1-3 GP 1-1_13	66.71	17.61	0.50	0.01	1.87	12.95
SR1-3 GP 1-1_14	65.60	18.45	0.63	0.01	3.05	12.14
SR1-3 GP 1-1_15	65.42	18.35	0.31	0.01	2.41	12.75
SR1-3 GP 1-1_16	66.72	18.72	0.70	0.04	6.19	7.47
SR1-3 GP 1-1_17	69.00	18.25	0.89	0.14	8.34	3.88
SR1-3 GP 1-1_32	66.28	17.69	0.81	0.03	2.59	12.22
SR1-3 GP 1-1_33	65.24	18.25	0.29	0.13	1.03	14.89
SR1-3 GP 1-1_34	64.31	18.07	2.19	0.00	1.09	14.45
Granophyre-1, line-2						

SR1-3 GP 1-2_1	65.91	18.65	0.63	0.02	3.63	11.35
SR1-3 GP 1-2_2	65.73	18.48	0.67	0.03	3.24	11.86
SR1-3 GP 1-2_3	65.04	18.31	0.56	0.36	2.09	13.52
SR1-3 GP 1-2_7	64.68	18.11	2.08	0.04	3.00	11.73
SR1-3 GP 1-2_15	65.45	18.71	2.61	0.17	7.45	5.92
SR1-3 GP 1-2_16	64.80	18.13	1.13	0.05	3.01	12.00
SR1-3 GP 1-2_20	66.84	18.88	1.26	0.08	8.83	4.32
SR1-3 GP 1-2_21	65.69	18.64	2.92	0.10	9.12	3.80
SR1-3 GP 1-2_22	65.58	18.47	1.98	0.09	5.60	8.88
SR1-3 GP 1-2_23	66.79	18.88	1.65	0.10	8.68	4.18
SR1-3 GP 1-2_24	67.64	19.19	1.12	0.09	10.37	1.96
SR1-3 GP 1-2_25	63.74	18.06	3.90	0.10	3.55	11.00
SR1-3 GP 1-2_26	64.54	18.26	3.98	0.08	5.16	8.79
SR1-3 GP 1-2_27	64.90	18.54	3.28	0.12	8.16	4.33
SR1-3 GP 1-2_28	67.32	19.20	2.02	0.16	11.36	0.52
SR1-3 GP 1-2_30	63.99	18.07	3.23	0.12	3.98	10.85
SR1-3 GP 1-2_31	66.23	18.77	2.13	0.09	7.57	5.85
SR1-3 GP 1-2_32	66.28	17.86	3.15	0.15	8.15	4.03
SR1-3 GP 1-2_34	67.03	19.47	1.64	0.43	11.37	0.18
SR1-3 GP 1-2_35	66.78	19.35	1.96	0.35	11.13	0.53
SR1-3 GP 1-2_36	66.28	18.28	2.84	0.13	7.05	5.94
GP-1 Avg	**65.78**	**18.43**	**1.51**	**0.09**	**5.10**	**9.06**
Std Dev	1.11	0.43	1.12	0.10	3.41	4.77
Anorthoclase-2, line-1						
SR1-3 AC 2-1_1	63.18	18.28	3.05	0.12	4.34	9.68
SR1-3 AC 2-1_2	65.11	18.92	0.82	1.09	7.54	5.16
SR1-3 AC 2-1_3	66.00	19.32	1.13	0.63	8.18	4.48
SR1-3 AC 2-1_4	65.26	19.56	1.68	0.60	8.72	3.77
SR1-3 AC 2-1_5	65.81	19.20	0.57	0.37	6.72	6.46
SR1-3 AC 2-1_6	66.13	19.36	0.19	0.34	7.01	6.41
SR1-3 AC 2-1_7	65.10	19.09	0.94	0.35	6.21	7.18
SR1-3 AC 2-1_8	65.03	19.00	1.10	0.41	6.01	7.62
SR1-3 AC 2-1_9	65.65	19.25	0.22	0.38	6.34	7.13
SR1-3 AC 2-1_10	65.93	19.54	0.10	0.47	7.20	5.92
SR1-3 AC 2-1_11	65.93	19.19	0.12	0.39	6.67	6.84
SR1-3 AC 2-1_12	65.71	19.36	0.58	0.36	6.76	6.57
SR1-3 AC 2-1_13	66.02	19.37	0.17	0.41	7.32	5.83
SR1-3 AC 2-1_14	66.18	19.41	0.17	0.36	6.97	6.29
SR1-3 AC 2-1_15	65.98	19.17	0.27	0.30	7.01	6.24
SR1-3 AC 2-1_16	65.36	18.96	0.49	0.51	6.25	7.37
SR1-3 AC 2-1_17	65.64	19.04	0.31	0.35	6.22	7.22

SR1-3 AC 2-1_18	65.95	19.07	0.24	0.33	6.48	6.85
SR1-3 AC 2-1_19	66.09	19.48	0.14	0.48	6.92	6.35
SR1-3 AC 2-1_20	65.57	19.31	0.30	0.41	6.27	7.38
SR1-3 AC 2-1_21	66.03	19.32	0.37	0.41	7.25	5.96
SR1-3 AC 2-1_22	66.18	19.53	0.12	0.38	7.57	5.76
SR1-3 AC 2-1_23	66.34	19.38	0.18	0.35	7.16	6.10
SR1-3 AC 2-1_24	66.03	19.27	0.18	0.31	6.99	6.41
SR1-3 AC 2-1_25	65.93	19.35	0.16	0.27	6.28	7.39
SR1-3 AC 2-1_26	65.70	19.19	0.24	0.22	5.57	8.21
SR1-3 AC 2-1_27	65.44	18.99	0.60	0.32	6.11	7.40
SR1-3 AC 2-1_28	65.38	19.01	0.21	0.30	5.23	8.74
SR1-3 AC 2-1_29	66.01	19.26	0.54	0.41	7.78	5.21
SR1-3 AC 2-1_30	65.45	19.11	0.59	1.04	7.71	5.60
SR1-3 AC 2-1_31	66.25	19.27	0.18	0.33	7.51	5.84
SR1-3 AC 2-1_32	65.89	18.94	0.20	0.26	6.38	7.39
SR1-3 AC 2-1_33	65.87	18.88	0.20	0.34	6.57	7.21
SR1-3 AC 2-1_34	64.63	19.46	0.33	1.89	7.08	5.86
SR1-3 AC 2-1_35	65.68	19.14	0.14	0.26	6.21	7.71
SR1-3 AC 2-1_36	65.51	19.18	0.85	0.29	6.48	6.95
SR1-3 AC 2-1_37	66.05	19.29	0.34	0.29	6.85	6.74
SR1-3 AC 2-1_38	65.90	19.37	0.55	0.31	7.22	6.19
SR1-3 AC 2-1_39	66.09	19.33	0.31	0.28	6.87	6.53
SR1-3 AC 2-1_40	65.86	19.08	0.44	0.25	6.59	7.06
SR1-3 AC 2-1_41	65.28	19.26	0.44	0.42	6.78	6.78
SR1-3 AC 2-1_42	66.08	19.39	0.22	0.27	6.60	6.86
SR1-3 AC 2-1_43	65.92	19.37	0.31	0.30	6.87	6.67
SR1-3 AC 2-1_44	65.82	19.25	0.63	0.31	6.91	6.25
SR1-3 AC 2-1_45	65.80	19.16	0.66	0.24	6.03	7.75
AC-2 Avg	**65.70**	**19.21**	**0.48**	**0.42**	**6.75**	**6.65**
Std Dev	0.53	0.22	0.51	0.28	0.75	1.03
Granophyre-2, line-1						
SR1-3 GP 2-1_6	64.15	16.14	2.26	0.24	9.49	0.38
SR1-3 GP 2-1_27	64.88	18.46	0.19	0.00	1.04	14.91
SR1-3 GP 2-1_45	64.65	18.32	0.54	0.08	1.23	14.43
Granophyre-2, line-2						
GP-2 Avg	**64.56**	**17.64**	**1.00**	**0.10**	**3.92**	**9.91**
Std Dev	0.37	1.30	1.11	0.12	4.83	8.25

Table A-2. Quantitative Analyses of Oxides

	Weight Percents of the elements (O calculated by stoichiometry)							
Label	**O***	**Si**	**Ti**	**Al**	**Cr**	**Fe^{2+}**	**Mn**	**Mg**
SG2-1: Fe-Ti Oxides								
SG2-1: Fe-Oxide	22.15	0.05	2.70	0.55	0.01	67.81	0.15	0.00
SG2-1: Fe: Oxide-2	21.02	0.06	1.05	0.05	0.00	69.92	0.04	0.00
SG2-1: Fe: Oxide-3	21.18	0.05	0.81	0.10	0.00	71.12	0.07	0.00
SG2-1: Fe: Oxide-4	21.14	0.04	0.77	0.05	0.01	71.18	0.06	0.00
SG2-1: Fe: Oxide-5	21.09	0.05	0.58	0.08	0.00	71.66	0.05	0.00
SG2-1: Fe: Oxide-6	21.35	0.04	1.27	0.15	0.00	70.53	0.10	0.00
SG2-1: Fe: Oxide-7	21.02	0.03	0.70	0.10	0.00	70.81	0.04	0.00
SG2-1: Fe: Oxide-8	21.10	0.02	0.68	0.09	0.00	71.58	0.05	0.00
SG2-1: Fe: Oxide-9	21.11	0.04	0.76	0.07	0.00	71.29	0.08	0.00
SG2-1: Fe: Oxide-10	21.08	0.06	0.98	0.03	0.01	70.82	0.06	0.00
Average	**21.22**	**0.04**	**1.03**	**0.13**	**0.00**	**70.67**	**0.07**	**0.00**
Std Dev	0.34	0.01	0.62	0.15	0.00	1.13	0.03	0.00
SR1-3								
Fe-Ti Oxides								
SR1-3: Fe-Oxide-1	20.70	0.20	1.54	0.08	0.00	67.43	0.08	0.00
SR 1-3: Fe: Oxide-2	20.28	0.18	0.91	0.07	0.00	67.51	0.05	0.00
SR 1-3: Fe: Oxide-3	20.33	0.17	0.79	0.08	0.00	67.99	0.04	0.00
SR 1-3: Fe: Oxide-4	20.46	0.11	1.87	0.03	0.00	66.35	0.04	0.00
SR 1-3: Fe: Oxide-5	20.67	0.14	1.39	0.06	0.00	67.99	0.03	0.00
SR 1-3: Fe: Oxide-6	20.35	0.13	0.81	0.04	0.00	68.44	0.05	0.00
SR 1-3: Fe: Oxide-7	20.28	0.23	0.95	0.08	0.00	67.24	0.07	0.00
SR 1-3: Fe: Oxide-8	20.35	0.13	0.71	0.05	0.00	68.49	0.03	0.00
SR 1-3: Fe: Oxide-9	20.82	0.39	2.17	0.13	0.01	65.25	0.15	0.04
SR 1-3: Fe: Oxide-10	20.35	0.18	1.00	0.11	0.00	67.30	0.06	0.01
SR 1-3: Fe: Oxide-11	20.22	0.10	0.61	0.05	0.01	68.41	0.05	0.00
SR 1-3: Fe: Oxide-12	20.32	0.12	0.69	0.04	0.00	68.55	0.05	0.00
SR 1-3: Fe: Oxide-13	20.60	0.08	0.98	0.05	0.00	68.95	0.06	0.00
SR 1-3: Fe: Oxide-14	20.62	0.13	1.39	0.05	0.00	67.70	0.13	0.00
Average	**20.45**	**0.16**	**1.13**	**0.07**	**0.00**	**67.69**	**0.06**	**0.00**
Std Dev	0.19	0.08	0.47	0.03	0.00	0.98	0.04	0.01
Ti Oxides								
SR 1-3: Ti: Oxide-1	31.14	0.32	37.39	0.07	0.01	19.01	0.71	0.04

Table A-3. Quantitative Analyses of Other Selected Phases

Weight Percent Components												
Label	**SiO_2**	**TiO_2**	**Al_2O_3**	**FeO***	**MnO**	**MgO**	**CaO**	**Na2O**	**K2O**	**F**	**O=F**	**Total**
Plagioclase in anothoclase												
Plag-1												
SG2-1 Pl1-1	64.51	0.00	22.11	0.12	0.01	0.00	3.36	9.62	0.27	0.00	0.00	100.01
SG2-1 Pl1-2	64.43	0.00	22.27	0.09	0.01	0.00	3.39	9.61	0.32	0.13	-0.06	100.20
SG2-1 Pl1-3	64.18	0.00	22.30	0.08	0.01	0.01	3.52	9.54	0.21	0.25	-0.10	99.99
SG2-1 Pl1-4	64.81	0.01	21.81	0.04	0.00	0.01	3.33	9.72	0.19	0.08	-0.03	99.96
SG2-1 Pl1-5	64.70	0.01	22.34	0.08	0.00	0.01	3.37	9.73	0.18	0.11	-0.05	100.50
SG2-1 Pl1-6	64.39	0.00	21.80	0.05	0.00	0.02	3.26	9.76	0.20	0.00	0.00	99.47
Plag-1 Avg	**64.50**	**0.00**	**22.11**	**0.08**	**0.00**	**0.01**	**3.37**	**9.66**	**0.23**	**0.10**	**-0.04**	**100.02**
Std Dev	0.23	0.00	0.25	0.03	0.01	0.01	0.09	0.09	0.06	0.09	0.04	0.34
Plag-2												
SG2-1 Pl2-1	62.94	0.01	22.63	0.27	0.02	0.02	4.31	9.17	0.18	0.34	-0.14	99.75
SG2-1 Pl2-2	63.19	0.00	22.80	0.04	0.00	0.00	4.38	9.21	0.22	0.24	-0.10	99.99
SG2-1 Pl2-3	63.74	0.02	22.57	0.11	0.00	0.03	4.06	9.35	0.26	0.14	-0.06	100.22
SG2-1 Pl2-4	63.34	0.02	22.64	0.07	0.02	0.01	4.24	9.27	0.22	0.00	0.00	99.83
SG2-1 Pl2-5	63.57	0.00	22.90	0.05	0.00	0.02	4.24	9.18	0.18	0.16	-0.07	100.23
Plag-2 Avg	**63.36**	**0.01**	**22.71**	**0.11**	**0.01**	**0.02**	**4.24**	**9.23**	**0.21**	**0.18**	**-0.07**	**100.00**
Std Dev	0.31	0.01	0.14	0.09	0.01	0.01	0.12	0.08	0.03	0.12	0.05	0.22
Brown Phase (unknown)												
SG2-1 Brn1	45.31	0.02	3.69	34.47	1.46	2.85	1.25	0.13	0.10	0.04	-0.02	89.30
SG2-1 Brn1-1	45.32	0.04	3.65	34.33	1.38	2.77	1.25	0.12	0.13	0.14	-0.06	89.06
SG2-1 Brn1-2	45.17	0.05	3.66	34.53	1.43	2.76	1.25	0.16	0.12	0.05	-0.02	89.16
SG2-1 Brn1-3	44.60	0.02	3.88	34.46	1.39	2.77	1.28	0.13	0.12	0.00	0.00	88.66
SG2-1 Brn1-4	45.05	0.06	3.83	34.67	1.42	2.81	1.21	0.16	0.13	0.00	0.00	89.34
SG2-1 Brn1-5	45.62	0.00	3.79	34.19	1.40	3.01	1.31	0.07	0.12	0.15	-0.06	89.61
SG2-1 Brn2-1	46.16	0.05	4.25	33.79	1.18	3.19	1.20	0.08	0.09	0.47	-0.20	90.26
SG2-1 Brn2-2	45.83	0.02	3.83	34.79	1.33	2.58	1.16	0.12	0.07	0.00	0.00	89.74
SG2-1 Brn2-3	45.31	0.03	4.02	34.13	1.26	2.91	1.22	0.13	0.08	0.24	-0.10	89.23
SG2-1 Brn2-4	45.41	0.04	3.86	34.36	1.35	2.81	1.22	0.11	0.08	0.03	-0.01	89.26
Brown Avg	**45.38**	**0.03**	**3.84**	**34.37**	**1.36**	**2.85**	**1.23**	**0.12**	**0.10**	**0.11**	**-0.05**	**89.36**
Std Dev	0.43	0.02	0.18	0.29	0.08	0.16	0.04	0.03	0.02	0.15	0.06	0.43
Clinopyroxene												
SG2-1 Cpx1-1	47.00	0.45	0.43	30.53	1.00	0.54	18.91	0.53	0.01	0.00	0.00	99.40
SG2-1 Cpx1-2	46.21	0.64	0.46	31.65	0.99	0.52	18.40	0.53	0.01	0.00	0.00	99.41
SG2-1 Cpx1-3	47.91	0.26	0.37	30.02	0.95	0.46	19.14	0.53	0.00	0.00	0.00	99.65
SG2-1 Cpx1-4	48.08	0.23	0.40	29.83	0.99	0.44	19.21	0.50	0.01	0.00	0.00	99.67
SG2-1 Cpx2-1	48.00	0.33	0.46	30.12	1.11	0.30	19.01	0.50	0.00	0.17	-0.07	99.92
SG2-1 Cpx2-2	47.79	0.29	0.45	30.12	1.03	0.30	19.22	0.44	0.00	0.00	0.00	99.65

SG2-1 Cpx2-3	48.33	0.15	0.28	29.56	1.04	0.36	19.49	0.56	0.01	0.11	-0.05	99.83
SG2-1 Cpx2-4	48.24	0.33	0.44	29.91	1.04	0.35	19.10	0.46	0.01	0.19	-0.08	100.00
SG2-1 Cpx2-5	47.97	0.33	0.43	30.08	1.04	0.31	19.20	0.45	0.01	0.22	-0.09	99.94
Cpx Avg	**47.73**	**0.33**	**0.41**	**30.20**	**1.02**	**0.40**	**19.07**	**0.50**	**0.01**	**0.08**	**-0.03**	**99.72**
Std Dev	0.68	0.14	0.06	0.60	0.04	0.10	0.30	0.04	0.00	0.10	0.04	0.22
Amphibole												
SG2-1 Hbl1-1	41.57	1.23	5.94	34.49	0.66	0.36	9.53	1.73	1.15	0.21	-0.09	96.77
SG2-1 Hbl1-2	42.19	0.75	5.53	35.29	0.75	0.22	9.42	1.53	1.05	0.57	-0.24	97.06
SG2-1 Hbl1-3	42.35	0.72	5.40	35.51	0.73	0.23	9.56	1.65	1.06	0.43	-0.18	97.46
SG2-1 Hbl1-4	42.45	0.70	5.31	35.74	0.76	0.22	9.41	1.65	0.94	0.27	-0.11	97.33
SG2-1 Hbl1-5	42.35	1.03	5.35	35.03	0.76	0.29	9.57	1.51	1.02	0.12	-0.05	96.99
SG2-1 Hbl-CPX1-	42.20	1.02	5.41	34.96	0.81	0.25	9.59	1.53	1.07	0.32	-0.14	97.04
SG2-1 Hbl-CPX1-1	42.26	1.06	5.46	35.01	0.77	0.28	9.48	1.61	1.06	0.59	-0.25	97.31
SG2-1 Hbl-CPX1-2	42.05	1.02	5.41	35.12	0.76	0.22	9.50	1.58	1.00	0.26	-0.11	96.81
SG2-1 Hbl-CPX1-3	42.28	1.06	5.44	35.10	0.77	0.26	9.46	1.53	1.03	0.42	-0.18	97.15
SG2-1 Hbl-CPX1-4	42.20	1.08	5.36	34.99	0.82	0.25	9.56	1.58	1.04	0.54	-0.23	97.20
SG2-1 Hbl-CPX1-5	42.08	1.07	5.41	35.39	0.77	0.29	9.44	1.57	1.02	0.16	-0.07	97.14
SG2-1 Hbl-CPX1-6	42.29	1.11	5.45	35.18	0.78	0.28	9.49	1.51	1.02	0.65	-0.27	97.49
SG2-1 Hbl-CPX1-7	42.15	1.12	5.45	35.34	0.76	0.26	9.55	1.56	1.06	0.50	-0.21	97.54
SG2-1 Hbl-CPX1-8	42.12	1.03	5.43	35.32	0.74	0.26	9.54	1.51	1.06	0.09	-0.04	97.05
Amph Avg	**42.18**	**1.00**	**5.45**	**35.18**	**0.76**	**0.26**	**9.51**	**1.57**	**1.04**	**0.37**	**-0.15**	**97.17**
Std Dev	0.21	0.16	0.15	0.30	0.04	0.04	0.06	0.07	0.05	0.19	0.08	0.24
Misc Phases												
SG2-1 Incl in brn-1	41.13	0.07	2.27	42.03	1.50	1.40	0.71	0.06	0.05	0.06	-0.02	89.25
SG2-1 Bt in Brn1	35.33	2.91	9.77	36.93	0.33	1.09	0.07	0.15	7.71	0.69	-0.29	94.69